TÉCNICO LISBOA

Structural Design of a MAME UAV Wing using High-Fidelity Numerical Tools

Vítor Manuel Tavares Silva

Thesis to obtain the Master of Science Degree in

Aerospace Engineering

Supervisor: Prof. André Calado Marta

Examination Committee

Chairperson: Prof. Jorge Manuel dos Santos Ribeiro Fernandes
Supervisor: Prof. André Calado Marta
Member of the Committee: Prof. Virginia Isabel Monteiro Nabais Infante

December 2023

Dedicated to my mother

Declaration

I declare that this document is an original work of my own authorship and that it fulfills all the requirements of the Code of Conduct and Good Practices of the Universidade de Lisboa.

Acknowledgments

I want to thank my supervisor, Professor André Calado Marta, for the endless and continuous support throughout this work. The professor's availability, guidance and positive posture were vital to the completion of this work.

I am also thankful for Dr. Joaquim Martins and Dr. Eirikur Jonsson, which provided the necessary Python libraries for this work, as well as the necessary support when required.

I also want to thank Tekever for their support and funding for this work, with a special mention to Eng. Nuno Matos, who also continuously supported my work and gave numerous valuable feedback.

Special thanks to my colleague Rúben Gameiro, who was part of the Tekever project work group, for the many laughs and support throughout this journey.

I am extremely grateful to my mother, who transmitted the love, strength, and support I needed to conclude this work. Without her numerous sacrifices, I would not have had the opportunity to undertake this degree. I am equally grateful to my father for the love, support and knowledge transmitted.

I am deeply indebted to my cousins, Manuel Nunes and Fátima Nunes, who provided me with a home to be able to come to Instituto Superior Técnico and pursue this Aerospace Engineering degree.

Finally, I would also want to generally thank other members of my family and friends, with special mention to my best friend, Ricardo Fontão, for the positivity and strength provided, as well as my girlfriend, Cláudia Fernandes, for the love and support.

Resumo

Com o rápido crescimento do mercado dos UAVs, soluções mais eficientes obtidas através de análises de elevada fidelidade e técnicas de otimização na metodologia de projeto, promovem uma enorme vantagem competitiva para os fabricantes. Este trabalho aborda o desejo de um fabricante líder de UAVs se manter competitivo no mercado dos UAVs de vigilância. Para tal, uma ferramenta de análise estrutural utilizando do método de elementos finitos foi demonstrada, sendo depois usada como parte de uma *framework* de análise e otimização estrutural. Para esta demonstração foram efetuadas análises estáticas a uma asa de um modelo existente de UAV, constituídas por compósitos em fibra de carbono com diferentes empilhamentos para duas condições de voo. Os resultados de deformação e falha desta ajudaram a avaliar o comportamento estrutural da asa. A validação da *framework* utilizando dados experimentais disponíveis apresentaram ligeiras diferenças devido às simplificações do modelo e à falta de propriedades exatas dos materiais. Diversas novas soluções ótimas da asa foram encontradas com espessuras de camadas e orientações de fibra variáveis. A primeira com constrangimentos de falha; às duas seguintes, um deslocamento máximo foi adicionado, tendo pontos de partida diferentes; às três seguintes, foram adicionadas constrangimentos de fabrico, tais como a continuidade do ângulo das camadas de fibra, a ortogonalidade entre as camadas e a espessura monotónicamente decrescente, respetivamente; por último, uma torção máxima permitida na ponta da asa foi adicionada. Foi possível obter uma redução de massa entre cerca de 44% e 56%, respeitando um fator de segurança de 1.5.

Palavras-chave: otimização, ambiente de projeto, método de variáveis adjuntas, método de elementos finitos, materiais compósitos, orientação de fibras.

Abstract

With the rapid growth of the UAV market, more efficient solutions obtained from high-fidelity analyses and optimisation techniques during aircraft design, promotes a huge competitive advantage. This work addresses the desire of a leading UAV manufacturer to improve its fleet to remain competitive in the surveillance UAV market. For this, a structural analysis tool using the finite element method was demonstrated, which was then used as part of a structural optimisation framework. For this demonstration, static analyses of the wingbox of an existing UAV model, with a CFRP material with different lay-ups were carried out for two flight conditions. Results of deformation and failure helped to evaluate the wingbox structural behaviour. Validation of the numerical design framework using available experimental data presented slight differences due to model simplifications and lack of accurate material properties. Several new optimal wingbox solutions were found with variable ply thicknesses and fibre orientations. The first was optimised only with failure constraints; a maximum allowed displacement was added to the following two but had different starting points; manufacturing constraints such as ply angle continuity, orthogonality of plies and monotonically decreasing thickness were added to the next three, respectively; and finally, for the fully constrained solution, a maximum allowed wing tip torsion was added. Mass reduction between about 44% and 56%, while respecting a safety factor of 1.5, was found possible.

Keywords: optimisation, design framework, adjoint method, finite element method, composite materials, fibre orientation.

Contents

List of Tables

List of Figures

Nomenclature

Greek symbols

γ	Tip Torsion
Δ	Interval
δ	Kronecker's delta
ε	Strain
θ	Ply angle
ν	Poisson ratio
ρ	Density
σ	Stress
ψ	Interpolation function

Roman symbols

E	Young's modulus
f	Function
G	Shear modulus
g	Constraint
R	FEM residuals
t	Thickness
$\mathbf{u}$	Displacement vector
v	Design variable
X	Nodal locations
x, y, z	Cartesian components

Subscripts

G	Geometric
h	Approximated
M	Material
max	Maximum
VM	Von Mises
x, y, z	Cartesian components
Y	Yield

Superscripts

e	Elemental

Glossary

BEM	Boundary Element Method
CAD	Computer Aided Design
CFD	Computational Fluid Dynamics
CPU	Central Processing Unit
CSM	Computational Structural Mechanics
DV	Design variable
DoF	Degrees of Freedom
FDM	Finite Differences Method
FEA	Finite Element Analysis
FEM	Finite Element Method
FVM	Finite Volume Method
GDP	Gross Domestic Product
HALE	High Altitude Low Endurance
KS	Kreisselmeier-Steinhauser
LE	Leading Edge
MAME	Medium Altitude Medium Endurance
MITC	Mixed-Interpolation of Tensorial Components
MTOW	Maximum Take-Off Weight
NASA	National Aeronautics and Space Administration
RAM	Random Access Memory
REF	Reference
RVE	Representative Volume Element
SATCOM	Satellite Communication
TACS	Toolkit for the Analysis of Composite Structures
TE	Trailing Edge
UAS	Unmanned Aerial System
UAV	Unmanned Aerial Vehicle
VTOL	Vertical Take-Off and Landing

Chapter 1

Introduction

In this chapter, a brief introduction to this work is provided, including an overview on the topic, the motivation of this thesis and the objectives and deliverables expected.

1.1 Topic Overview

Beginning of aviation

In a divided and militaristic Europe, in the 16th century, the idea of flying machines that could possibly make surprise attacks and destroy facilities by dropping explosives was thought by an Italian Jesuit, Father Francesco de Lana. Although he purposed some infeasible designs, the main idea was to make a ”lighter than air” machine, leading the way to the first successful human flight. Only in November of 1783, however, this first flight happened with Pilâtre de Rozier and Marquis d'Arlandes hovering over Paris for about 25 minutes in a hot-air balloon. Although ballooning was the first major demonstration of the flying capacity, in 1799, Sir George Cayley started testing the lift created by different shapes at different angles and speeds and designed the first configuration that resembles a modern airplane. Backed by Cayley's research on lift, the idea of steam powered ”heavier than air” machines was becoming a reality. In 1903, the world's first powered flight with an aircraft was performed by Wilbur Wright with the Flyer. In the following years, the first european flight happened, as well as the increase in the time and height of flights, all possible due to engineering progresses. Also, passenger test flights started to happen proving that flying was both practical and safe [1].

However, when World War I striked in Europe, Unmanned Aerial Vehicles (UAVs) started being developed for dropping bombs. Instead of having balloon configurations like Francesco de Lana thought, they had more advanced features and shapes.

UAV

One of the first recognized UAV was the Kettering Bug in 1917, developed for the US Army which had a biplane configuration with detachable wings. Upon hovering the target, they were released and the

fuselage with explosives would hit the ground. Although, the World War I years were filled with suffering and sadness and the UAVs were used purely for lethal purposes, they started having better uses for the upcoming years. During the Vietnam War, for instance, these machines were massively used for reconnaissance. After it, Israelis also found uses for UAVs, taking down the Syrian air defences by using them not only for reconnaissance but also jamming and as decoys. With such uses, they showed that UAVs were valuable and worth to invest in [2].

Moving further in time to the modern era, technological improvements and size reduction of these vehicles lead to a wider range of possible uses. Equipped electronics, cameras and sensors, UAVs are not only used as a vehicle, but as a whole system.

(a) Drone carrying out aerial thermography in photovoltaic plant in Spain

(b) Tekever's AR4 for surveillance and reconnaissance missions

(c) Spylite from BlueBird AeroSystems that can be used to monitor and detect oil spills

(d) RQ-11B Raven from AeroVironment that can be used to monitor and detect red tides

Figure 1.1: Example of UAS with different uses

Some use cases of these Unmanned Aerial Systems (UAS) include:

- Inspection of photovoltaic plants - a more specific application of thermography using UASs can be found in photovoltaic plants, seen in Fig. 1.1 a), since their large size requires higher maintenance capacity as well as innovative techniques. The main advantage is that aerial thermography greatly reduces the time of manual inspections [3];
- Precision agriculture - in this type of agriculture, UASs are used for weed mapping and management, vegetation health and growth monitoring, irrigation management and crops spraying [4];
- Urban environment and management - applying this aerial vehicles in urban areas gives real-time monitoring of traffic, road conditions as well as building observation [5];

- Disaster hazard and rescue - with the emerging global warming concerns and the increase in wildfires, fire monitoring is essencial to quickly and accuratly respond when necessary. In the eventuality of larger disasters, specially in remote places, the use of UASs for post-disaster assessment and emergency response is a quick and safe option that can be vital [5];
- Maritime monitoring - there are many specific applications on maritime monitoring, including monitoring oil spills, gas pipes, whales and marine life, tracking fishing boats as well as controlling illegal immigration [6]. Some UAS used for this purposes are presented in Fig. 1.1 b) to d).

UAVs can be classified depending on weight, endurance and range, altitude, wing loading and type. Since the major requirements of the UAS system to be developed/optimised in this work are based on altitude and endurance, only the classes for different ranges, endurances and altitudes are presented in Tab. 1.1.

Table 1.1: Classes of UAS depending on endurance, range and altitude [7]

Class	Endurance	Range	Altitude
High	>24 hours	>1500 Km	>10 Km
Medium	5 - 24 hours	100 - 400 Km	1 - 10 Km
Low	<5 hours	<100 Km	<1 Km

1.2 Motivation

With so many applications being brought up and many more to be developed, investment in the UAS industry has been a trend for the past couple of years, with many companies, mainly start-ups, directing their funds to explore new and original applications to be competitive. Since 2000, more than 300 start-ups entered the UAS market, focusing on hardware, support services and operations [8]. They have gathered more than 3 billion USD to develop the industry with new applications, as seen in Fig. 1.2.

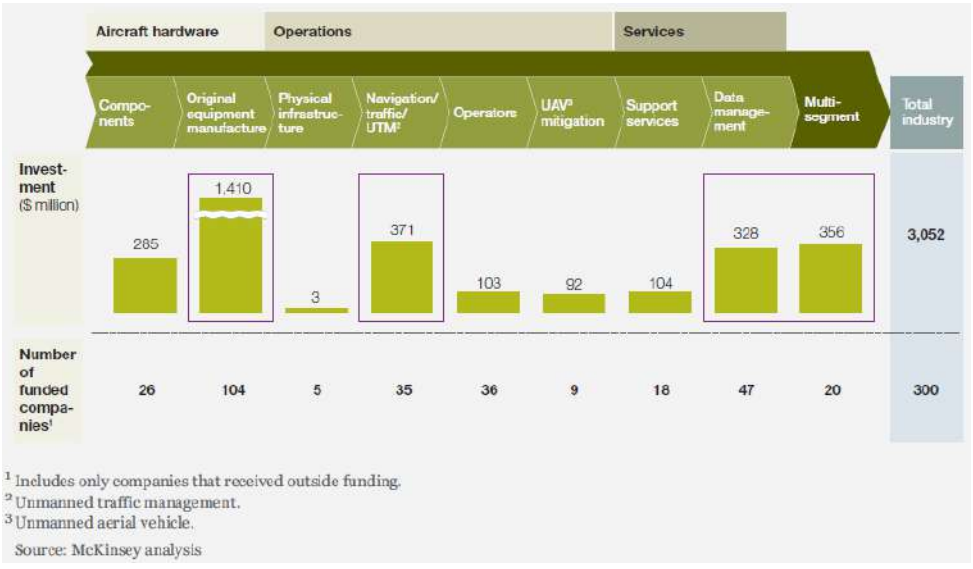

Figure 1.2: Start-ups in the USA receiving over 3 billion USD in investment [8]

This strong commercial growth has been translated into a rise in UAV activity from 40 millions USD in 2012 to 1 billion USD in 2017, solely in the United States. It is also projected that in 2026, the commercial use of UASs will have an impact of 31 billion USD, up to 46 billion USD in the USA's gross domestic product (GDP). Moreover, by this time, it is expected that the value of commercial UAV manufacturing in the USA should rise to about 8 to 20 billion USD [8]. Although such growth has been predicted for the USA, it can be a good estimate on how the investment in other markets is expected to increase.

In order to maintain this growing market trend, it is important to focus on five main factors: public acceptance, economic drivers, technology, regulation and infrastructure [8].

The scope of this work is integrated within the context of economic drivers and specially, in improved technological capabilities. In order to remain competitive in this growing market, the demand for highly efficient and optimised UASs increases since they can help lowering time and energy costs. With energy prices increasing, longer flight times of a UASs, for example, can reduce the number of times it needs to take-off and land, resulting in faster missions and less time allocated for non-mission related maneuvers.

Having established the motivation for this work, it is relevant to present the project on which this thesis is integrated and based upon.

1.3 Project Framework

This work is part of a collaboration between the company Tekever and the academia. Tekever is a company founded in 2001 that manufactures and operates their UAS mainly for surveillance missions. Besides this, they also provide training and maintenance for some customers who prefer more autonomy on their work [9].

The goal of the entire project is to achieve a multipoint optimal design of a MAME UAS using high-fidelity numerical tools. Regarding this work, the objectives and expected deliverables are described in Sec. 1.4.

Products and Missions

With Tekever's array of products, there is a wide variaty of missions they can execute. The main ones focus on maritime surveillance, ranging from whale watching to tracking fishing boats, monitoring gas pipes and even controlling illegal immigration.

Their current fleet is composed of three different UAS:

- AR3 - a versatile and customizable UAS capable of performing missons up to 16 hours. Its endurance highly depends on the configuration since it can have Vertical Take-Off and Landing (VTOL) capability, specially important for deployment from small boats. Otherwise, it needs to be launched from a catapult.

- AR4 - a lightweight UAS designed to be rapidly deployed, by hand throw, and mainly used for military or commercial apllications.

- AR5 - the most advanced Medium Altitude Medium Endurance (MAME), presented in Fig. 1.3, with increased endurance over similar concurrent UASs and reduced operating costs. It is mainly used for maritime patrolling and surveillance.

Figure 1.3: Tekever AR5

The main AR5 specifications are resumed in Tab. 1.2.

Table 1.2: Some characterístics of the Tekever AR5

Wing span	Cruise speed	MTOW	Payload	Endurance	Comms range
$7.30\,\mathrm{m}$	$100\,\mathrm{km\,h^{-1}}$	$180\,\mathrm{kg}$	$50\,\mathrm{kg}$	$12\,\mathrm{h}^{\star}$	Unlimited (SATCOM)

For take-off and landing specifications, this UAS needs a track and as a drawback, it can not take-off with crosswinds. Regarding the payload, one advantage is that, for rescue missions that may require fast action on site, the AR5 can transport an inflating raft. However, this added weight might affect the total endurance and reduce total operating time from 16h to 12h. Finally, since it uses Satellite Communication (SATCOM) for communication with the operator, there is no range limit for operating, which is really advantageous.

1.4 Objectives and Deliverables

The objective of this work is to establish a numerical high-fidelity framework for composite wing structural analysis and design. Taking advantage of the open source computational structural mechanics (CSM) software and additional commercial software for pre- and post-processing, structural analysis and optimisation will be performed.

Initially, a simple test case is analysed to check the results accuracy and test the framework. Then, the baseline Tekever AR5 configuration is studied and the CSM parameters tunned to match as best as possible, the experimental data provided by Tekever. Finally, an optimisation of the wing structure is performed.

Having the results analysed and validated, at the end of this thesis, the validation of this structural analysis tool and an enhancement of the Tekever AR5 performance due to the optimisation of the wing structure is provided.

The work tasks are presented in Fig. 1.4.

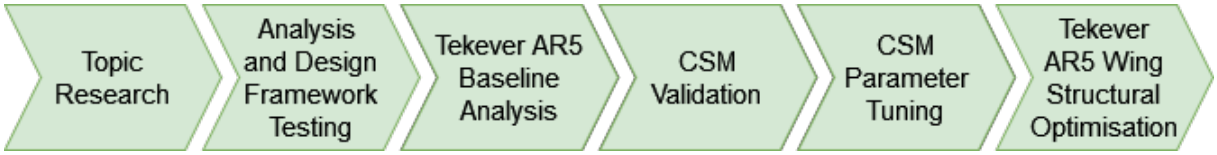

Figure 1.4: Thesis work plan

1.5 Thesis Outline

This work is divided into seven chapters. In the first one, an introduction is given with a brief overview of the topic, as well as the motivation of this work, the project into which this thesis is integrated, and finally, the objectives and deliverables that are expected in the end.

The second chapter provides a traditional aircraft design methodology overview, including a market analysis of 50 UAVs, typical wing structure details, and design phase descriptions, along with a literature review on structural optimisation.

The third chapter covers theoretical aspects of structural analysis and optimisation, including computational solid mechanics, material properties (isotropic vs. orthotropic), and the use of composite materials. It also discusses failure criteria and the finite element method, with an emphasis on potential numerical errors and error mitigation strategies. In the latter part of this chapter, optimisation techniques are introduced, including parameters for defining optimisation problems, a comparison of gradient-based and gradient-free algorithms, and a focus on gradient-based methods. It also discusses sensitivity calculations and places significant emphasis on explaining the adjoint method for optimisation.

The fourth chapter provides insights into computer-based solid mechanics and optimisation processes, covering pre-processing (geometric definition, mesh generation, and computational modelling of composites) and explaining the software architecture used for structural analysis and gradient calculations. It also discusses constraint imposition and post-processing, concluding with a test case that showcases the framework and validates custom constraints.

The fifth chapter focuses exclusively on the structural analysis of the Tekever AR5 wing. It covers UAV baseline descriptions, a material definition, a mesh refinement study, load conditions and constraints, concluding with a discussion and comparison of results for various load conditions. The sixth chapter highlights the structural optimisation of the Tekever AR5 wing, presenting and comparing results from six optimisation cases and concluding with a summary and discussion of the outcomes. Lastly, the conclusion and achievements of this work are given in the seventh chapter, together with some suggested future work improvements.

Chapter 2

Aircraft Design

In this chapter, the conventional aircraft design methodology is presented. Beginning with the market overview, containing a research of the currently used UAVs for surveillance and monitoring purposes, up to the detailed aircraft design. In the conceptual and preliminary design phases, examples of wing mass and sizing approaches are given.

2.1 Methodology

Aircraft design usually follows a traditional and very clear methodology, as seen in Fig. 2.1, with three distinct phases: conceptual, preliminary and detailed.

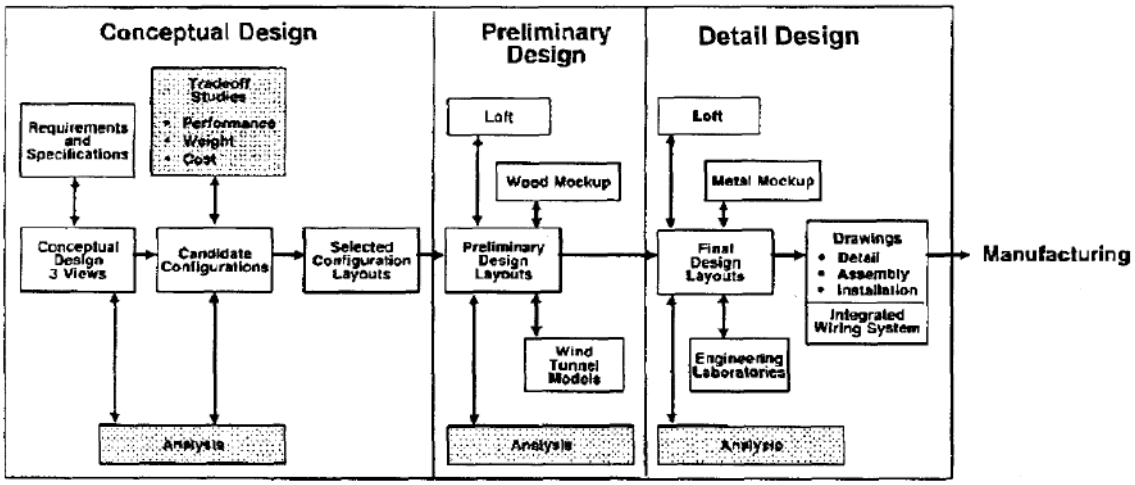

Figure 2.1: Traditional aircraft design methodology [10]

It starts by setting, as a basis, every known requirement for the misson or task, the aircraft is to be designed for. For a new vehicle, its purpose should be clearly set in the beginning to specify its categorie. Based on specific requirements (range, take-off and landing distances, cruise speed, etc), the categorie can be further refined, allowing the vehicle to be inserted in more specific subcategories [11].

2.2 UAV Market Overview

With that in mind, a market analysis is performed to meet the necessities and requirements that consumers are looking for. There are many types of requirements, namely for performance, operations, production, environmental impact, among others [12]. In the context of this work, since its major focus is the design phase, some design requirements are exemplified in Tab. 2.1 with the corresponding parameters and components affected by them.

Table 2.1: Relationship between aircraft major components and design requirements (Based on [12])

No.	Design requirements	Aircraft component/parameters affected most
1	Payload (weight) requirements	Maximum take-off weight
2	Payload (volume and geometry) requirements	Fuselage
3	Performance requirements (range and endurance)	Maximum take-off weight, fuel weight
4	Performance requirements (maximum speed, rate of climb, take-off run, stall speed, ceiling, and turn performance)	Engine, landing gear, and wing
5	Stability requirements	Horizontal tail and vertical tail, weight distribution
6	Controllability requirements	Control surfaces (elevator, aileron, rudder), weight distribution
7	Flying quality requirements	Center of gravity, weight distribution
8	Airworthiness requirements	Minimum safety requirements
9	Cost requirements	Materials, engine, weight, etc.
10	Design duration requirements	Configuration optimality
11	Detectability requirements	Materials, configuration

An example of such requirements being established for a specific mission is given by Panagiotou et al. in [13], in which, for their MALE UAV to be used for monitoring and surveillance operations in Greece, they define its flight, structural and payload requirements accordingly.

Another important aspect to consider in this preliminary phase is that, with increasing market value, as referred in Sec. 1.2, it is relevant to further enhance the characteristics of an already existing UAV, with new versions/generations of such aircraft, than having a timely and costly investment in a new complete design [12].

Regarding the topic of monitoring and surveillance, a market research of the drones used for this purposes was performed. Historically, one of the main parameters in aviation is the Maximum Take-Off Weight (MTOW). With that in mind, a graph showcasing different UAVs with their wingspan and MTOW relation is presented in Fig.2.2, in an attempt to correlate the data and identify the market trends. This is specially useful to estimate some parameters, for example the wingspan, given a required MTOW for a certain mission. For this market overview, the data of 50 UAVs, including the Tekever AR5, was used and some of them are illustrated in Fig. 2.3. The extracted data is given in Appendix A. The best fitting correlation was a power law, with equation presented in Fig. 2.2. It is considered that the correlation factor is good and visually inspecting, the data looks to have the correlation behaviour, with the exception of some outliers. To improve this correlation factor however, more UAVs should be included, specially with larger wingspans.

Looking at Fig. 2.2, it can be concluded that the Tekever AR5 has two close competitors with about

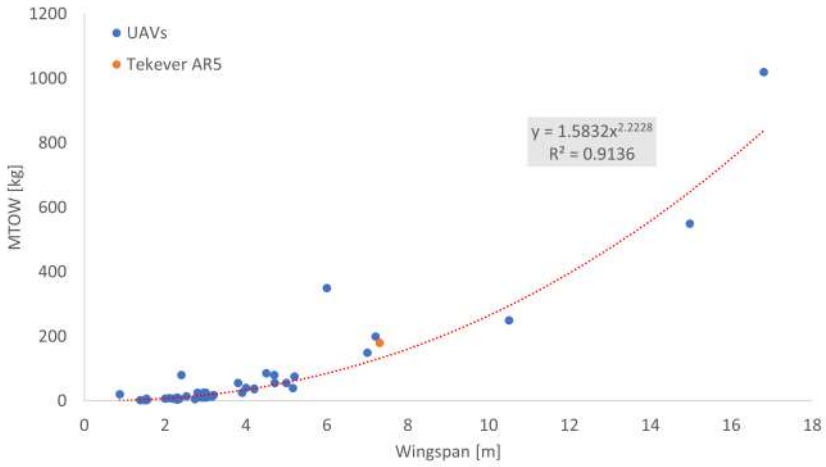

Figure 2.2: Wingspan vs MTOW of some surveillance UAVs in the market

the same wingspan and MTOW. This indicates that, with an optimal, and consequently, lighter solution for the same wingspan and MTOW, more payload could be added. This would result in a more competitive solution and possibly preferred over the others, dominating the market within this size category of UAV.

(a) Albatross 2.2 from UAVOS

(b) Raybird 3 from Skyeton

(c) PD-2 from Ukrspec Systems

(d) CGT50 from A-TechSYN

(e) P330 Pro from CHCNAV

(f) Atlantic I from SCR

Figure 2.3: Drone examples from current market analysis

After gathering this data, it is important to retain, once again, that some estimations of general parameters of the UAVs can be then obtained based solely on mission requirements and current market trends. These, help to start the design phase, that will be described thereafter. Before that however, taking in consideration that this work focuses on a wing analysis and optimisation, a brief description of its internal structure is given.

2.3 Wing Structure Layout

The typical internal components of a wing are represented in Fig. 2.4. The main and most impor-

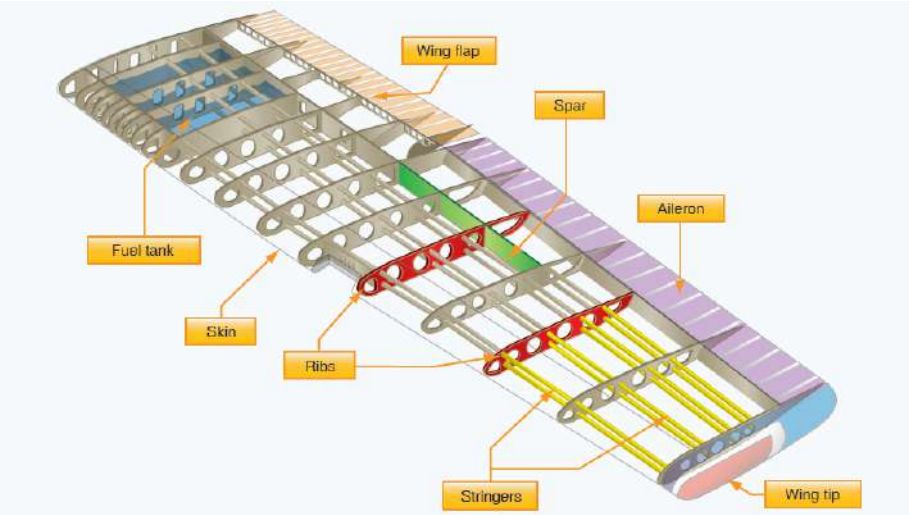

Figure 2.4: Wing structural components [14]

tant parts are the skin, spars, ribs and stringers. Each one plays a very important role to support the aerodynamic loads on the wing.

The stringers and spars are necessary, specially for bending and torsion stiffness. Combined with the skin, the structure is able to handle the normal loads more easily since the loads are distributed. For the ribs, their main purpose is to form the wing to the desired shape as well as assists with buckling since the outer skin is usually a thin shell, highly prone to buckling [15].

To evaluate the performance of the wing, analyses are performed to get data that allows the engineers, in the several design phases, to assess how efficient the wing might be. The most common parameters used to make this evaluation are:

- Wing mass - to make sure that the weight is not far from the estimation;
- Maximum displacements - to ensure small deformations and an acceptable wing stiffness;
- Von Mises stresses - to ensure that the material can safely withstand all expected loads in the elastic regime;
- Buckling - to ensure structure stability, buckling should be analysed, being usually critical on the top skin due to bending loads on the wing;
- Natural vibration frequencies - for aeroelastic phenomenon mitigation.

Having this in mind, the design stages can now be explained and the examples better understood.

2.4 Design Phases

Conceptual Design

A conceptual design is firstly developed to get the initial size, total weight and an estimation of its distribution, to satisfy static stability requirements and general aerodynamic characteristics. In this stage,

sketches are made and a general shape is obtained.

With such configuration, the first analysis are made, using very simple tools, and the estimations refined. This step is highly iterative, since some compromises might need to be done to the requirements, in order to have a working aircraft. Besides that, to find an optimal solution, more concepts can be created so that the next design phases are based on the supposedly optimal aircraft layout [10, 11]. An illustration of this design phase is given in Fig. 2.5.

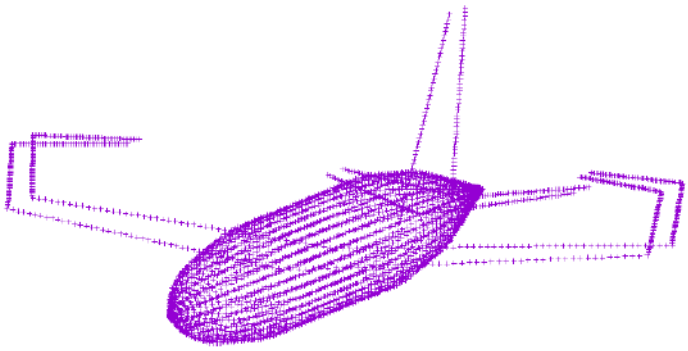

Figure 2.5: Conceptual geometry in a weight estimation tool [16]

One example of this conceptual design stage is given by Howe [17], where mass estimation strategies are given. The first method presented is empirical and only applicable to wings made from light alloy. The basis of this approach is a mathematical function in order to the wing geometry, operational parameters and a coefficient (C_1) that is a function of the type of aircraft

$$C_1 = A - BM_T \times 10^{-6}\,, \tag{2.1}$$

where A and B are tabulated for different types of aircraft and M_T is the design take-off mass in kg. This method relies heavily on data interpretation, which means that for some types of aircraft the results might be less accurate, but it is simple to apply and gives accurate results in about 86% of the test cases presented. However, it does not take in consideration, more specific and special cases which might be a disadvantage in some cases, like a new wing configuration.

Preliminary Design

The following phase consists of the preliminary design, which includes a more detailed analysis of different portions of the aircraft. In the case of structures, for example, the loads acting upon the aircraft structure, due to aerodynamic forces and weights are taken in consideration and a more detailed design and analysis is performed. More complex behaviours like the aeroelastic motion are also considered, making it possible to further refine the structural design and aircraft shape. To support this preliminary design and its analyses, some tests are also initiated. Fig. 2.6 illustrates this design phase where the authors in [18] were sizing the wingbox to resist buckling loads.

It is after this design phase that a decision of its construction is made, estimating cost and time to build the aircraft. This estimation is the main goal of this design stage and it is of high importance to

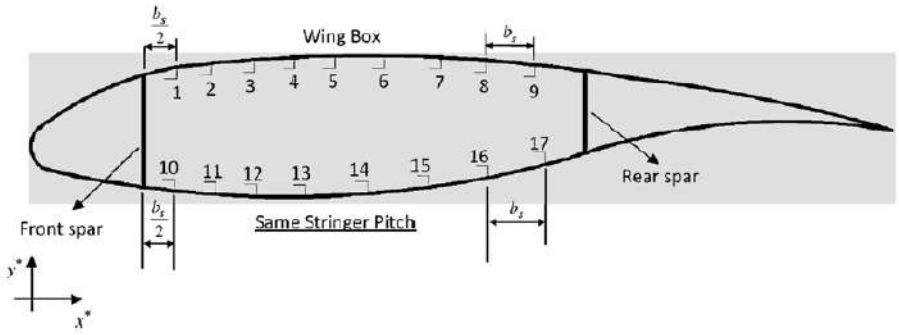

Figure 2.6: Preliminary arrangement of stringers [18]

understand if the vehicle is feasible [10, 11].

A more complex tool for wing weight estimation and structural sizing is given in [19]. This tool has two modules: one to initially size the wing internal structure and a second one to size the wingbox more accurately, taking in consideration aeroelastic behaviour. The weight estimation has a quasi-analytical approach. The thickness of equivalent panels that model the wing skin, stringers and spar webs are obtained using analytical expressions. These relate the maximum stresses allowed and the wing shape to obtain the said thicknesses. After this initial estimation, an empirical correlation is used to represent the secondary components weight, and finally a total weight is obtained [19, 20]. The aeroelastic behaviour was not considered in this case, so the second module is precisely used for that purpose. Coupling both the structural and aerodynamic models, a structural analysis is performed using 3D finite beam elements and a vortex lattice method to obtain the aerodynamic loads (mesh used presented in Fig. 2.7). To them, a 1.5 safety factor is applied.

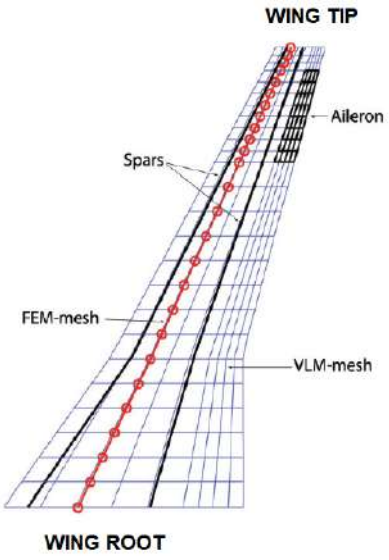

Figure 2.7: Structural and aerodynamic mesh [19]

Having as inputs the thicknesses previously calculated in the first module, the tensile and shear stress distributions are obtained. With this coupled system, an optimisation problem can be formulated and the weight of the wing minimized for the expected loads. This way, a more accurate estimation of

the wing weight is expected [19].

Detailed Design

Finally, a detailed design is made to incorporate and visualize every detail for the aircraft construction. Each major component like wings or the fuselage, for example, is divided in the individual pieces (ribs, skin, spars, etc) that make the part altogether and they are individually designed and analysed. After that, the fabrication processes and the respective components assembly are defined. In this phase, some changes to parts can also be made to facilitate the manufacturing and diminuish their cost. Finally, the initial requirements are confirmed to be met or need to be adjusted [10, 11]. An illustrative example of this design phase is given in Fig. 2.8 were the authors validate a detailed FEM model with a wing attachment with experimental data [21].

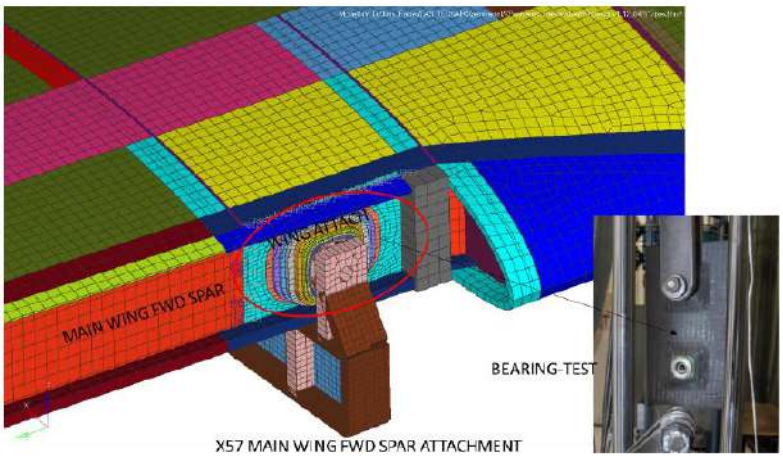

Figure 2.8: Detailed FEM with a ply-based model arrangement of stringers with test setup for wing attachment [21]

One important aspect to note is that, in the different stages of the design process, different types of analysis are performed. Accordingly, earlier in the process, the level of complexity of these are lower and grow throughout the stages [10]. It is in the preliminary and detailed design stage that Computer Aided Design (CAD) and Computer Structural Mechanics (CSM) play an important role.

With the development of technology and computational capabilities, this higher fidelity analysis and design tools brought more accurate measurements of weight, dimensions, center of gravity position. Not only that but also the overall geometry and internal layout of the aircraft can be better studied and some parts precisely dimensioned. These tools help the traditional aircraft design methodology, not only to have a reduction in costs and time but also to improve the design quality [22].

2.5 Optimal Design

After describing briefly each phase of a traditional aircraft design methodology, it can be understood that these are not smooth phases in terms of development, since they require many iterations until the specific objectives and requirements of each phase are met. This iterative characteristic of the traditional

methodology has some disadvantages namely in increasing time and costs, which creates a potential for numerical optimisation to enhance the design process.

In [23], Grose explains that the competitiveness of a company is high if: it can provide fast responses to consumer needs by reducing development or manufacturing times; the aircraft is produced with the least possible costs; and if it requires low maintenance, indicating a good final product quality. Using optimisation as a tool to improve all these aspects, the traditional process can change by having an optimiser directly and automatically changing some pre-established design variables. To ensure the final version given by the optimiser might be the best for a certain objective, a set of constraints is also pre-established. With this tool, an aircraft development time can be reduced, thus reducing costs. By combining this with a judgment of an experienced engineer, the final product is expected to surpass legacy solutions.

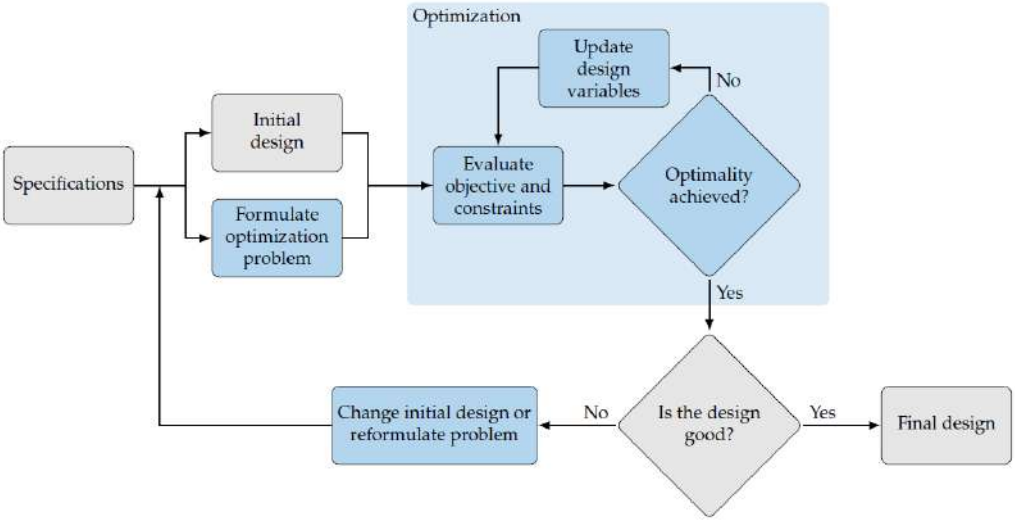

Figure 2.9: Design phase with optimisation process [24]

Although this is mainly an automated process, there is still some degree of iteration since the solution given by the optimiser might need some refinement, as Fig. 2.9 shows. That is why there is still a lot of time spent by engineers to ensure the problem is properly formulated with the right objective in mind, the design and manufacturing constraints properly translated into mathematical formulations and the design variables adequately chosen [24]. As such, optimisation is not a foolproof solution to the design process that reduces time and costs, since it still depends on the engineering inputs and final solution evaluation. Nevertheless, it is definitely an useful tool to expedite the design process. An illustrative example of an optimisation is provided in Fig. 2.10.

2.6 Literature Review

Having established the steps on the traditional aircraft design with the inclusion of optimisation processes, it is now relevant to give a broader but brief overview of some work developed in structural optimisation.

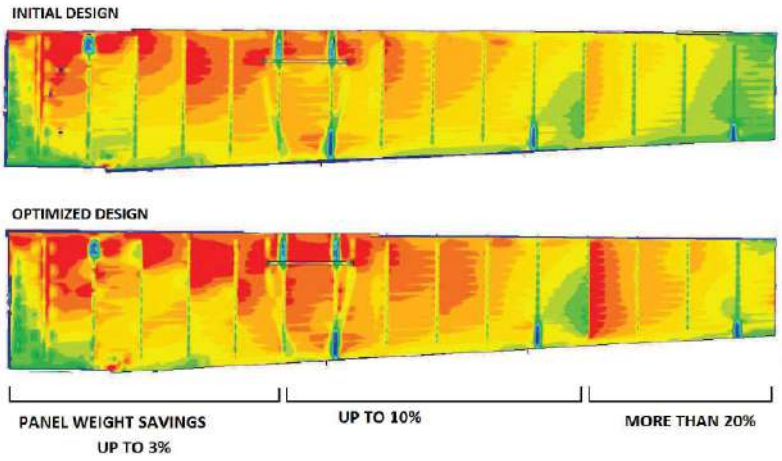

Figure 2.10: Stress distribution in initial and optimal wing panel's solution [25]

The optimisation applications can vary from wind turbine blades to hydrofoils and airplane wings. One example of this was an hydrostructural optimisation applied to an hydrofoil [26]. The objective was to minimize the drag coefficient under failure, cavitation and manufacturing constraints, using as design variables the hydrofoil shape and ply orientations. The optimisation was successful, showing significant delay in the cavitation while also achieving a maximum drag reduction of 5% for the composite case, relative to the baseline.

Focusing on the aeronautical field, a structural optimisation of a high aspect ratio composite wing model was performed for different load conditions while comparing an aluminium and composite wing [27]. After a load selection process to determine the most relevant sizing loads (2.5g manoeuvre), the optimisation process is setup up. As design variables, the authors only used the thickness distribution of each component, with fixed layups for each component in the composite wing: ($60\%0°$, $20\%\pm45°$, $20\%0°$) for the skin panels and ($10\%0°$, $80\% \pm 45°$, $10\%0°$) for the ribs and spars. As constraint, a maximum strain criterion was used. This optimisation has the structural model coupled with the aerodynamic to update the loads in each iteration, due to the structural deflections. One of the results showed a 14.5% reduction in mass using composites. Using a load alleviation procedure, to shift the lift distribution more towards the root, the authors were also able to reduce the wing structural mass a maximum of 8.6% with a 5.1% reduction of the wing root bending moment. The final solution presented a maximum deflection of 17.5% of the half wing span.

Another way to have composites as design variables is presented in [28], where the authors used lamination parameters as design variables to tackle the challenge of a large amount and discrete nature of these variables, when using plies thickness and any possible ply angle as a design variable. In this work, the authors were minimizing the mass of a wingbox while trying to obtain the optimal orientation of stringers, as well as the optimal lamination parameters, under buckling and failure constraints. For minimum mass, it was found optimal to have a near $0°$ angle on the stringers.

Other type of approaches to structural optimisation is changing the actual shape of the internal structure of the wing. An internal structure optimisation with curvilinear spars and ribs (SpaRibs) is presented in [29] where the design variables are parameters that define their profile and also their number. Due to

their nature being mixed with both continuous and discrete desgin variables, the authors used a particle swarm optimisation algorithm. For the panels formed between the intersections of the skin, ribs and spars, their thickness is updated using a local panel optimisation under buckling constraints. As conclusion, a structural mass reduction of 4.98% relative to the baseline using straight spars and ribs and the same number of stiffeners was obtained, proving that curvilinear SpaRibs have reduce the structural weight.

Using an heuristic method, it was successfully demonstrated the efficient use of a framework based on the equivalent-plate methodology which exhibited an excellent accordance between this numerical model and the equivalent 3D Finite Element Method [30]. Using stiffness, strength and dynamic aeroelastic as constraints and the number of plies with $-45°$, $0°$, $45°$ and $90°$ as design variables, the authors obtained the optimal thickness distribution for each component, shown in Fig. 2.11, under a 2.5g manoeuvre. An Ant Colony optimisation algorithm was used together with a penalty method due to the discrete nature of this optimisation.

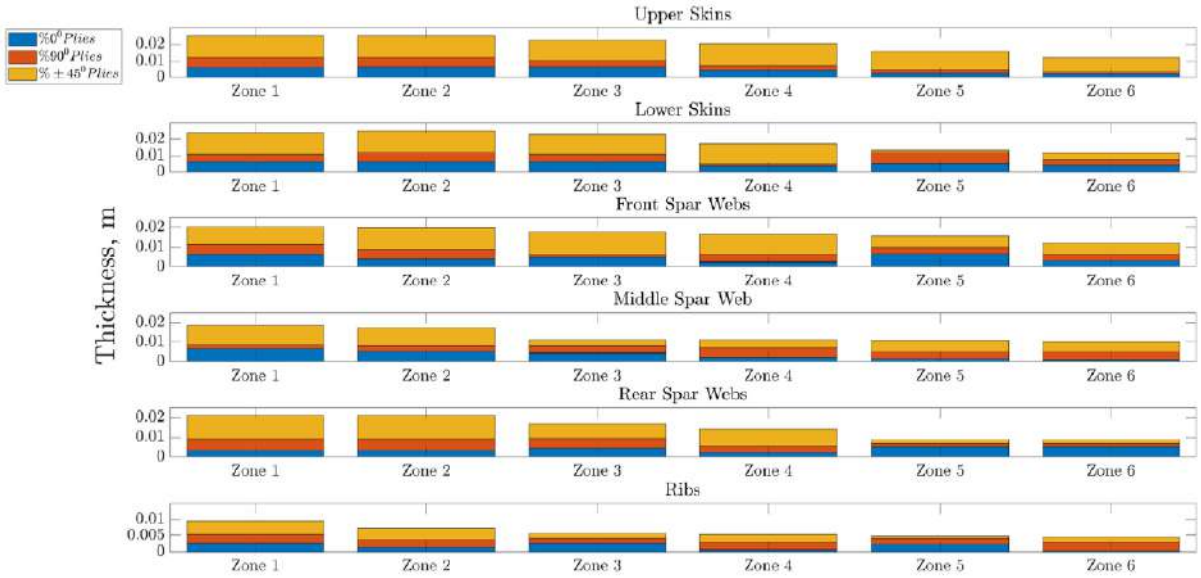

Figure 2.11: Component wise spanwise ply thickness distribution [30]

To assess the importance of the starting point during the optimisation process, a CRM wingbox model both with isotropic and composite materials was used [31]. Several mass minimization problems with two different algorithms were created using strength and stiffness constraints. As design variables, for the isotropic case, the thickness and the cross-sectional area of the wingbox spar caps and stiffeners is used. For the composite, the number of plies corresponding to each angle of the layup $[-45°_{n_1}/0°_{n_2}/45°_{n_3}/90°_{n_4}]$ are used as well as the previously mentioned cross-sectional area. The isotropic wingbox revealed to have similar results and to be independent on the starting point and algorithm. In contrast, the composite case had several mass penalties for certain starting points and method. With it, it was possible to conclude that the composite wingbox was more sensible to changes in the starting point and, considering that using composites increased the design space largely.

Finally, a mass minimization on a high-aspect ratio wingbox using a high-fidelity gradient-based struc-

tural optimisation was performed in [32]. A 2.5g load condition was used and, besides adjacency and stress constraints, it also included a geometrically nonlinear flutter constraint. As design variables, the total thickness of each component was used. The FEM model was assembled and solved considering an isotropic material. Afterwards, it was translated into a low-order beam representation to evaluate the nonlinear flutter constraint. The final optimal solution was an actual increase in mass ranging from $+11.1\%$ with a root angle of attack of $0°$ (Fig. 2.12) up to $+52.7\%$ with a root angle of attack of $6°$, with significantly different thickness distributions.

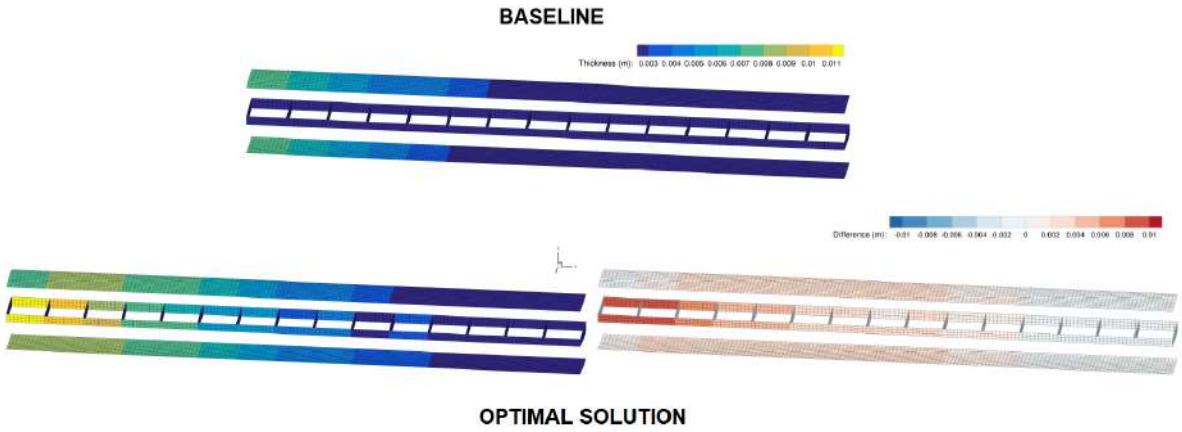

Figure 2.12: Comparison of the baseline and optimised structural sizing [32]

Across this work, this same research and more is presented to support the decisions taken and steps made, specially for the type of optimisation algorithm best suited in this work's case and the sensitivities calculation method (only required for gradient-based methods). These conclusions can be found in Sec. 3.8.

Chapter 3

Structural Analysis and Optimisation

In this chapter, numerical methods for solving structural mechanics problems are presented, such as the Finite Differences Method, Finite Element Method and Boudary Element Method. Focusing on the Finite Element Method, a more detailed explanation is given, as well as some typical errors present by the use of such method.

3.1 Computational Solid Mechanics

Computational Structural Mechanics (CSM) models, with numerical methods, the behaviour of solid structures. Since exact solutions to the governing equations are often impossible to attain, either by the geometric or material behaviour complexity, many numerical methods are developed to solve them. This complexity is represented by the linearity or non-linearity in problems. When linearity is present in structural mechanics, the displacements are proportional to the applied forces and the material behaviour is in the elastic domain (linear elasticity), where stresses vary linearly with strains and strains vary linearly with displacements. Non-linearity arrives when larger deformations are present and the plasticity of materials needs to be considered [33].

The most commonly used numerical methods are the Finite Differences Method (FDM), Finite Elements Method (FEM), Finite Volume Method (FVM) and Boundary Element Method (BEM). Although there are many methods, there is not a right one for every situation. According to the type of problem, regarding the problem formulation or the geometry, different methods are more adequate to be used.

The FDM is easily formulated and extended for two and three dimensional problems and it is a good option for simple geometries. In this process, derivatives in the governing equations are discretized using a Taylor series expansion which then give approximate solutions [34]. One example of its use can be found in [35] where the dynamic interaction between a tunnel structure and the soil was evaluated to simulate seismic behaviour for underground facilities.

The FEM, also mentioned in [35], consists in the discretization of the domain in several subdomains (elements) in which, the governing equation of the problem is approximated. This discretization helps complex systems and geometries to be approximated by several polynomials in each element, giving

the complete problem solution when all these elements are coupled [36]. This method is the one which is going to be used in the current work and will be further detailed in Sec. 3.6.

Regarding the BEM, this method has been specially used, in the structural field, for analysis of plates and shells. Contrary to the FEM, instead of discretizing the whole domain, the BEM uses line elements in the boundary of the domain. One example of its application is given in [37] where a numerical formulation for the modal analysis of anisotropic plates is presented. In this, the integrals over the plate domain are transformed in boundary integrals and for that, the plate discretized with boundary elements. One of the main advantages of the BEM over the FEM is that, in some cases, it is not easy to distinguish between thin shell, thick shell or a 3-D model to choose the finite element accordingly. Not only this but, in FEM models with 3D elements, the corresponding BEM model only requires a surface (boundary) mesh, making the modelling of the problem easier [38].

Finally, the FVM is mainly used for simulations with conservation laws, namely mass flow, heat and fluid mechanics problems [39], so it does not have a great importance in the field of structural mechanics.

3.2 Material Constitutive Laws

In order to model the material behaviour under certain loads, material constitutive equations are formulated. Depending if this behaviour is a function of the current state of deformation or only on the initial state of deformation, these materials are characterized as elastic or hyperelastic, respectively.

Even though the material might have another behaviour regimes, like the plastic or even non linear elastic behaviour, the constitutive equations that are presented, model a linear elastic behaviour for infinitesimal deformations [40]. This is known as the generalized Hooke's law and is given by

$$\sigma_{ij} = C_{ijkl}\varepsilon_{kl} + \sigma^0_{ij} \ , \tag{3.1}$$

where σ is the stress tensor, C is a stiffness tensor, containing material parameters, ε is the strain tensor and σ^0_{ij} is the residual stress tensor. Since C is a fourth-order tensor, there are 81 components to characterize the material. However, due to symmetry conditions in all three tensors and assuming the material as hyperelastic, the number is reduced to 21 components.

To visualize this, the Voigt-Kelvin notation is used, where the two subscripts in the stress and strain tensors are substituted by a single one, using the relations

$$\begin{aligned} &\sigma_1 = \sigma_{11},\ \sigma_2 = \sigma_{22},\ \sigma_3 = \sigma_{33},\ \sigma_4 = \sigma_{23},\ \sigma_5 = \sigma_{13},\ \sigma_6 = \sigma_{12} \ , \\ &\varepsilon_1 = \varepsilon_{11},\ \varepsilon_2 = \varepsilon_{22},\ \varepsilon_3 = \varepsilon_{33},\ \varepsilon_4 = 2\varepsilon_{23},\ \varepsilon_5 = 2\varepsilon_{13},\ \varepsilon_6 = 2\varepsilon_{12} \ . \end{aligned} \tag{3.2}$$

Having that and assuming that the reference configuration is stress and strain free ($\sigma^0_i = \varepsilon^0_i = 0$) [40], Eq. (3.1) can be written in matrix form as

$$\begin{Bmatrix}\sigma_1\\ \sigma_2\\ \sigma_3\\ \sigma_4\\ \sigma_5\\ \sigma_6\end{Bmatrix} = \begin{bmatrix}C_{11} & C_{12} & C_{13} & C_{14} & C_{15} & C_{16}\\ C_{21} & C_{22} & C_{23} & C_{24} & C_{25} & C_{26}\\ C_{31} & C_{32} & C_{33} & C_{34} & C_{35} & C_{36}\\ C_{41} & C_{42} & C_{43} & C_{44} & C_{45} & C_{46}\\ C_{51} & C_{52} & C_{53} & C_{54} & C_{55} & C_{56}\\ C_{61} & C_{62} & C_{63} & C_{64} & C_{65} & C_{66}\end{bmatrix} \begin{Bmatrix}\varepsilon_1\\ \varepsilon_2\\ \varepsilon_3\\ \varepsilon_4\\ \varepsilon_5\\ \varepsilon_6\end{Bmatrix} \Leftrightarrow \left\{\varepsilon\right\} = \left[S\right]\left\{\sigma\right\} \ , \tag{3.3}$$

with $C^{-1} = S$, both symmetric and S being named as the compliance tensor.

When the material properties vary for different directions, a material is called anisotropic. Two commonly used types of materials are isotropic (for example, aluminium or steel alloys) and orthotropic (for example, fibre-reinforced polymers).

Orthotropic Material

In this type of material, there are three orthogonal planes of symmetry characterizing the behaviour. With that, Eq. (3.3) reduces to

$$\begin{Bmatrix}\varepsilon_1\\ \varepsilon_2\\ \varepsilon_3\\ \varepsilon_4\\ \varepsilon_5\\ \varepsilon_6\end{Bmatrix} = \begin{bmatrix}\frac{1}{E_1} & -\frac{\nu_{21}}{E_2} & -\frac{\nu_{31}}{E_3} & 0 & 0 & 0\\ -\frac{\nu_{12}}{E_1} & \frac{1}{E_2} & -\frac{\nu_{32}}{E_3} & 0 & 0 & 0\\ -\frac{\nu_{13}}{E_1} & -\frac{\nu_{23}}{E_2} & \frac{1}{E_3} & 0 & 0 & 0\\ 0 & 0 & 0 & \frac{1}{G_{23}} & 0 & 0\\ 0 & 0 & 0 & 0 & \frac{1}{G_{13}} & 0\\ 0 & 0 & 0 & 0 & 0 & \frac{1}{G_{12}}\end{bmatrix} \begin{Bmatrix}\sigma_1\\ \sigma_2\\ \sigma_3\\ \sigma_4\\ \sigma_5\\ \sigma_6\end{Bmatrix} \ , \tag{3.4}$$

where E_i is the Young's Modulus for the ith direction, ν_{ij} is the ratio between transverse shear in the jth direction to the axial strain in the ith direction with an applied stress in the ith direction (Poisson ratio) and G_{ij} is the shear modulus for the ijth plane [40]. There are, then, only 9 independent material properties due to symmetry of the S tensor, namely

$$E_1,\, E_2,\, E_3,\, G_{23},\, G_{13},\, G_{12},\, \nu_{12},\, \nu_{13},\, \nu_{23} \ .$$

Isotropic Material

This type of material is characterized for not having any preferred direction, which means the material behaviour is the same in any of those directions.

Due to that fact, the Young's modulus, the Poisson ratios and the Shear modulus do not depend on the orientation and a relation between these three variables can be obtained,

$$E_1 = E_2 = E_3 \equiv E \,/\, G_{23} = G_{13} = G_{12} \equiv 2G = \frac{E}{1+\nu} \,/\, \nu_{12} = \nu_{13} = \nu_{23} \equiv \nu \tag{3.5}$$

3.3 Composite Materials

In this work, the structures expected to be analysed are mainly composed of composite materials. This type of material is characterized as a mixture of chemically and/or geometrically different materials, called matrix and reinforcement, which are generally not soluble in each other.

There are many types of composites, depending on the origin of either the matrix or the reinforcement. Two of the most commonly used composite materials are GFRP (Glass Fibre Reinforced Polymer) and CFRP (Carbon Fibre Reinforced Polymer), generally with continuous fibres in a certain direction with a polymeric resin matrix. By stacking layers of these impregnated fibres (called plies or laminae) in different angles, a layup is created, as illustrated in Fig. 3.1.

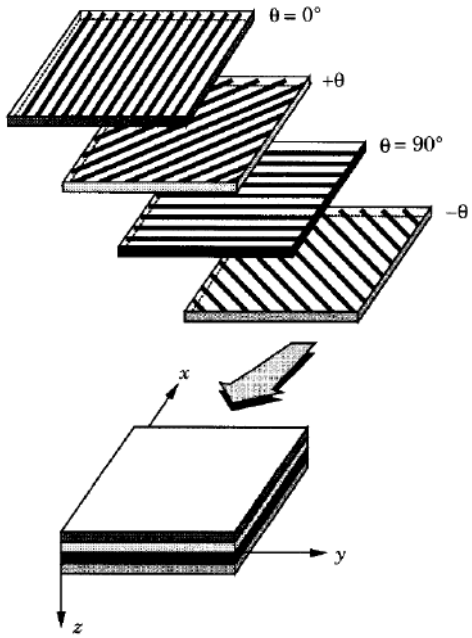

Figure 3.1: Composite layup with different angles [40]

Depending on the angles and the number of plies in each direction, the material properties of the composite can be tuned to meet the desired characteristics. Assuming that all fibres are oriented in the same direction and all parallel within a ply, each laminae can be assumed to have orthotropic behaviour.

The main difficulty is to obtain the properties of one ply, so there are many different approaches to the problem, from theories to laboratorial determination of properties. One of the theories is the rule of mixtures (or a micromechanics approach). Assuming that there is a perfect bound between fibres and matrix, fibres are parallel and uniformly distributed, the matrix has no voids or cracks and is in an initial stress-free state, both the fibres and the matrix are isotropic and have a linear elastic behaviour and finally and that the loads are either perpendicular or parallel to the fibre direction, the relations

$$\begin{aligned} E_1 = E_f v_f + E_m v_m \quad &; \quad E_2 = \frac{E_f E_m}{E_f v_m + E_m v_f} \\ G_{12} = G_{21} = \frac{G_f G_m}{G_f v_m + G_m v_f} \quad &; \quad \nu_{12} = \nu_{21} = \nu_f v_f + \nu_m v_m \end{aligned} \tag{3.6}$$

can be obtained [40]. In these relations, E_f and E_m represent the Young's Modulus of the fibre and

matrix, respectively, ν_f and ν_m the Poisson's ratio of the fibre and matrix, respectively and v_f and v_m the volume fractions of fibre and matrix, respectively.

Another way of obtaining the material properties of a ply is using a representative volume element (RVE) which is a small portion of the laminate that has some details of the microstructure of the composite. The volume is then analysed using the FEM and equivalent properties obtained. However, it is important to note that these properties are either lower bounds or upper bounds of the actual properties of the orthotropic ply, depending on the set of loads and/or boundary conditions imposed to the RVE. More about this method can be found in [41].

Having each ply property, the layup stiffness matrix $\overline{Q}$ can be assembled. Afterwards, the matrices A, B, and D are obtained which represent the membrane stiffness, the membrane-bending coupling stiffness, and the bending stiffness, respectively [40].

3.4 Failure Criteria

To predict failure of composite materials, it is necessary to characterize the composite strength for different load conditions (axial, transverse and shear tensile stresses as represented in Fig. 3.2), which are reflected in their longitudinal, transverse and shear tensile strength parameters. These are then used in the failure criteria to predict failure when a part of the structure with a composite material is under a combination of these type of loads.

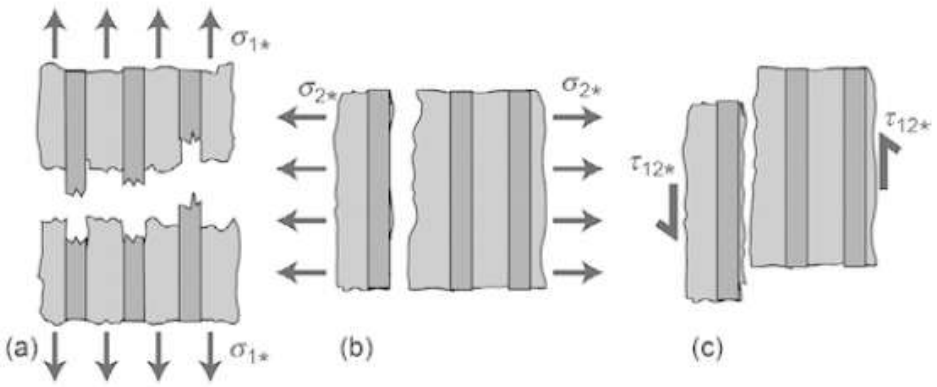

Figure 3.2: Schematic of the fracture of a unidirectional long fibre composite with (a) axial, (b) transverse and (c) shear applied tensile stresses [42]

Although composites are mainly used in components under tensile loads due to their usually high tensile strength in the fibre direction, compressive stresses can occur, specially due to bending moments. This means that the compressive strength of composites also needs to be taken into consideration, since compressive failure of these is possible. Since this type of failure generally occurs due to the constraint imposed by the composite matrix and depends on its shear strength and also the matrix-fibre strength, it should not be confused with buckling, that is dependent on the elastic properties and dimensions of the composite. These compressive strength parameters are also used in failure criteria such as the Tsai-Wu, to calculate some of the F_{ij} coefficients in Eq. (3.8).

Finally, to check if structures fail under certain loads, failure criteria are needed to ensure safety and predict material failure.

Von Mises criterion

The most commonly used criterion for isotropic materials is the Von Mises stress which can be normalized with the material yield stress, creating a failure index that when equal or above 1, material failure is expected. In the 2D domain, $\sigma_z = 0$, so, this index is defined as

$$F_{VM} = \frac{\sigma_{VM}}{\sigma_Y} = \frac{\sqrt{\sigma_x^2 + \sigma_y^2 - \sigma_x\sigma_y + 3\sigma_{xy}^2}}{\sigma_Y} \,, \tag{3.7}$$

where σ_{VM} is the Von Mises stress, σ_Y is the materiel yield stress and σ_x, σ_y and σ_{xy} are the normal and shear stress state under load [43].

Tsai-Hill criterion

A similar criterion, that derives from the Von Mises stress but is adapted for unidirectional composite material, is the *Tsai-Hill* criterion. This depends on the stresses of each orthogonal direction and, instead of using yield stresses, the measured strength parameters mentioned above are used [42].

Tsai-Wu criterion

For composite materials, however, the failure criterion needs to be different since deformation depends on the direction of the applied forces due to the orthotropic characteristic of the plies. The failure criterion that can be used in this case is the Tsai-Wu criterion, defined as

$$F_{TW} = F_1\sigma_1 + F_2\sigma_2 + F_{11}\sigma_1^2 + 2F_{12}\sigma_1\sigma_2 + F_{22}\sigma_2^2 + F_{66}\sigma_{12}^2 \,, \tag{3.8}$$

where σ_i is the stress component in the ith direction in the principal material coordinates of each ply (1 to 3 are normal stresses and 4 to 6 are shear stresses) and F_{ij} are coefficients that depend on the material normal and shear strengths [40].

Maximum Strain criterion

Finally, another criterion that can be used is the maximum strain. As the name suggests, failure of the material is considered to have happened when the strains reach a certain peak. This is traduced mathematically to when, at least one of the following inequalities, is not satisfied:

$$\varepsilon_1 < \mathsf{X}_{\varepsilon_t} \quad \varepsilon_2 < \mathsf{Y}_{\varepsilon_t} \quad \varepsilon_1 > \mathsf{X}_{\varepsilon_c} \quad \varepsilon_2 > \mathsf{Y}_{\varepsilon_c} \quad |\gamma_{12}| < \mathsf{S}_{\varepsilon} \,, \tag{3.9}$$

where $\mathsf{X}_{\varepsilon_t}$ and $\mathsf{X}_{\varepsilon_c}$ are the maximum tensile and compressive normal strains in the 1-direction, respectively, $\mathsf{Y}_{\varepsilon_t}$ and $\mathsf{Y}_{\varepsilon_c}$ are the maximum tensile and compressive normal strains in the 2-direction,

respectively, and S_ε is the maximum shear strain in the 1-2 coordinates.

This maximum strains are obtained by the ratio of the tensile and compressive strength parameters of the composite, over its elastic properties, and their formulation can be found in [44].

3.5 Buckling

Buckling is a type of failure mode that occurs in structures due to compressive loads. These cause a sudden change in the stability of the structure, going from stable to unstable, making its shape change, as shown in Fig. 3.3. This failure happens since the energy necessary to compress a certain structural element in a given point (critical buckling load) becomes to high and a warped configuration is more energetically efficient [45].

Figure 3.3: Airplane with fuselage skin that suffered buckling (Credit: Tony Webster, 2016)

Typically in aviation, the main components that are more prone to suffer from this problem are the fuselage and the wing skin panels, since they are the thinnest and longest parts in an aircraft. To tackle this, various solutions can be implemented. Some include the installation of longerons, stringers and bulkheads adequately sized across the fuselage length [11], such as the ones in Fig. 3.4, to help resist the compressive forces, as well as the addition of stringers in the wing inner structure (Fig. 2.4), to help the spars support bending moments that create compressive stresses in some sections of the wing.

3.6 Finite Element Method

Depending on the type of problem, different governing equations can be used to model the structure. As previously stated, a domain is discretized by several elements in which the solution of the governing equations is obtained. The advantages of dividing the domain into several finite elements are the possibility of modelling continuously the interface of different, materially and geometrically, parts of that domain, as well as the higher simplicity of approximating a solution in smaller domains instead of its entirety.

With this method, the possible solutions found are the nodal displacements and rotations. These are called the degrees of freedom (DoF). There are a maximum of 6 DoF per node (translation in x, y and

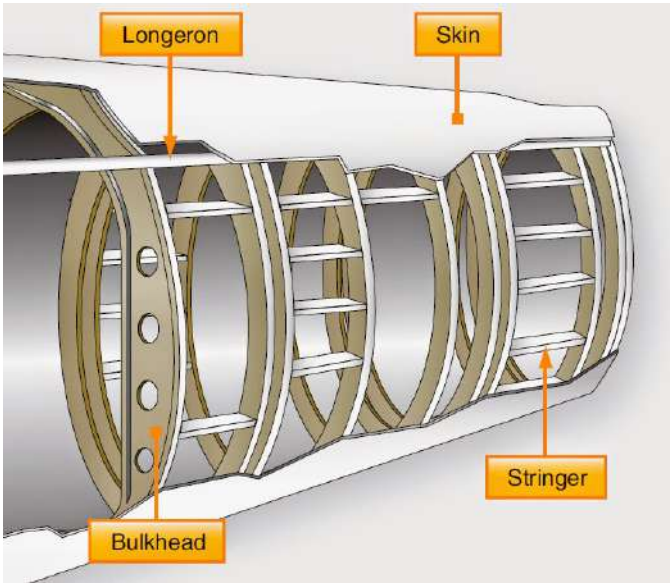

Figure 3.4: Fuselage with longarons, bulkheads and stringers [46]

z directions and rotation about x, y and z axes), but this number depends on the element formulation. Some commonly used elements will be presented in Sec. 3.6.2. By interpolating within the elements, the solution for points inside them is obtained. With the displacement field, the strain is computed as well as the stresses, following material constitutive laws.

For the shell elements, mentioned in Sec. 3.6.2, the basis theory is the classical first order deformation theory [40]. In this, the transverse plane does not remain perpendicular to the mid plane after deformation including shear strains in model. With it, the variables to be determined in this formulation are the mid-plane displacements and the rotations about the x and y axis. To add the rotation about z (also called "drilling degree of freedom"), a penalty approach is used [47, 48]. Although it is not necessary to add this DoF, its inclusion reduces difficulties with model construction, programming, numerical sensitivity and others [47]. Then, with laminate constitutive equations the stresses are obtained from the strains.

3.6.1 General Lagrange 2D Element Formulation

To briefly explain how the interpolation within each element works, a general example of a Lagrange element formulation is given. In this method, only the desired function is interpolated and not its derivative.

Since the governing equations are solved to obtain nodal displacements, the displacement field $u(x, y)$, for example, needs to be interpolated within the element. The approximation is given by a linear combination of polynomial functions as

$$u(x, y) \approx u_h^e = \sum_{i=1}^{n} u_i^e \psi_i^e \,, \tag{3.10}$$

where u_h^e is the approximated elemental displacement field, ψ_i^e are the element interpolation functions

and u_i^e the nodal values [36].

One way of defining the u_h^e functions is using the Pascal's triangle. Depending on the shape of the element and the number of the nodes, the polynomial function uses different terms of the Pascal's triangle. An example of this triangle is presented in Fig. 3.5.

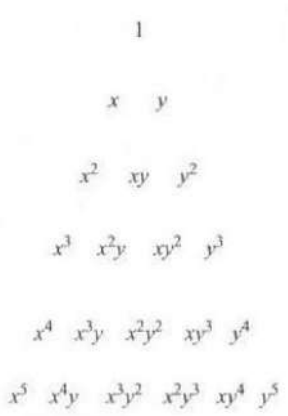

Figure 3.5: Pascal's triangle [36]

For a triangle, for example, the number of nodes represents the number of terms from the Pascal's triangle, counting from the top and going line by line. In this case, for a triangle with 6 nodes (3 nodes in the vertices and 3 nodes in the middle of each side), u_h^e would be defined as

$$u_h^e(x,y) = a_1 + a_2 x + a_3 y + a_4 x^2 + a_5 xy + a_6 y^2 \,. \tag{3.11}$$

For rectangular elements, the terms are obtained from the same Pascal triangle but they do not follow the same line by line rule.

Finally, to define the ψ_i^e functions, a local element reference frame needs to be set. Then, after enumerating the nodes, the interpolation functions are obtained using the following properties:

$$\begin{cases} \psi_i^e(x_j^e, y_j^e) = \delta_{ij} \\ \sum_{i=1}^{n} \psi_i^e = 1 \end{cases} , \tag{3.12}$$

where (x_j^e, y_j^e) are the nodal coordinates of the jth node and δ_{ij} is the Kronecker's delta.

Having this defined for every element, the approximated displacement field u_h^e can then be obtained for every element with Eq. (3.10).

3.6.2 Element Types

For the FEM, numerous elements formulations were created in order to better discretize the model to be analysed, according to the governing equations. From the elements presented in [36, 40], a division can be made, depending on the problem dimension:

- 1D line elements:
  - Bars (with 1 DoF in each node - 1 translation)

  - Beams (with 2 DoF in each node - 1 translation and 1 rotation)
  - Frame elements (with 3 DoF in each node - 2 translations and 1 rotation as represented in Fig. 3.6 a))
  - Timoshenko Beam (2 nodes on the edges, with 2 DoF and 1 central node with 1 DoF)
- 2D triangular or quadrangular elements:
  - Plate (with 3 DoF in each node - 1 translation and 2 rotations)
  - Membrane (with 2 DoF in each node - 2 translations as represented in Fig. 3.6 b))
  - Shell (with 5 DoF in each node - 3 translations and 2 rotations)
- 3D solid elements:
  - Tetrahedrals (4 nodes)
  - Triangular prisms (6 nodes)
  - Hexahedral (8 nodes - Fig. 3.6 c))
  - Higher order triangular and hexahedral - each element with 3 DoF per node

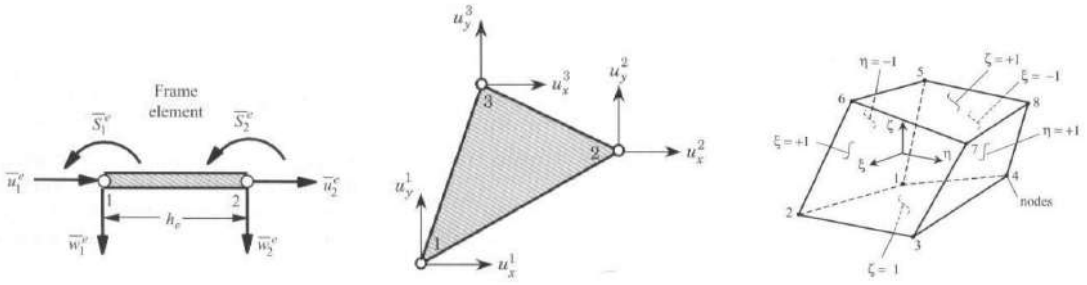

(a) (b) (c)

Figure 3.6: FEM Elements (a) 1D frame (b) Membrane (c) Hexahedral (8 nodes) [36]

As described, different elements have a different numbers of DoF which implies that, to obtain certain solutions, not all elements are suitable. For example, in 1D, if an element is under a bending load, bar elements can not be used to model this problem since they can only deform axially. Also, if a load is applied only axially, there is no need to add complexity with other 1D elements and the most efficient ones would be bars. A similar thought can be made for 2D elements.

Also, regarding the element order, since the displacement fields are interpolated within the element, better approximations can be achieved using higher order polynomials. This implies that more nodes need to be used, for the same element. An example can be a triangle with 6 nodes (3 in each vertex and 3 in the middle of each side segment).

Since real structures are 3D, it would be assumed that 3D elements are the only used elements. However, they have increased dimensions and complexity in comparison to 2D elements. In cases where thin structures, like the wing skin, are analysed, a simplification can be done where 2D shell

elements are used to model the middle plane of the skin. One example of this can be found in [49] where the authors analysed a composite wing for a HALE UAV using quadrangular 2D shell elements only.

The CSM solver software used throughout this work has three implemented types of elements that are good candidates to be used in the analysis in further chapters: Higher-order shell elements for linear analysis in the integrated framework, 2D quadrilateral higher-order plane stress elements and 3D hexahedral elements for both geometrically linear and non-linear analysis [50]. The main difference between the 2D plane stress elements and the 2D shell elements is that, their formulation is different and the latter take into account bending effects of the shell since they incorporate the rotation DoF in their nodes. Since the wingbox is composed of shell structures like the skin and the ribs, the expected elements to be used in the analysis are the higher-order shell elements which, since they are based on a MITC (mixed-interpolation of tensorial components) approach, shear and membrane locking is avoided [40, 50]. It is important to note that, according to the formulation used for these elements, a modelling error is introduced which makes these not suitable for shell structures with high thickness and curvature radius. With that in mind, in possible areas of the wing were the thickness is significant and variations of stress is relevant within the thickness, 3D elements should be used.

3.7 Numerical Errors

Since an approximation of the solution of the governing equations is obtained, it is important to address the errors deriving from this approximation and define their sources, to improve upon them for better results. There are 3 types of errors [36]:

- Domain approximation errors;
- Quadrature and finite arithmetic errors;
- Approximation errors.

Regarding the first type, these are connected to the discretization. When in presence of curvature in the domain, the finite elements induce an error since in any of the dimensions, they only possess straight lines and planar faces. As an example, consider the circumference (1D model) presented in Fig. 3.7. Line segments are used to model the shape but the final shape can never have curvature. This means that the analysed domain is not exactly the real one and errors always exist in this case. It is also important to notice that, when the number of segments increase, combined shapes of them get closer to being a circumference, which indicates that, the higher the discretization, the more accurate the domain representation is, as well as the errors inherent from this approximation tend to decrease.

The second type of error comes from numerical computation. In this case, numbers might be rounded-off and not be exact in their computation and the integrals necessary for the system matrices are not accurately evaluated due to the method used for such integration. This type of error can be reduced by increasing the computational representation of floating-point numbers, for instance using 64 bits (double precision) instead of 32 bits (single precision).

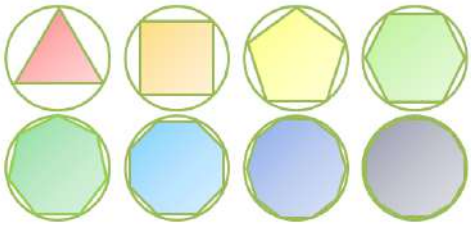

Figure 3.7: Circumference discretization

Finally, the last type of error is inherent from the fact that, in each element, the solution of the displacements is given as an approximation. As presented in Eq. (3.10), the element wise displacement field (u_h^e) is approximated as a sum of the nodal displacements times the shape functions that come from the element formulation. This type of errors can be reduced by using higher-order shape functions instead of linear ones.

3.8 Optimisation Techniques

As explained in Sec. 2.5, the optimisation process requires the definition of pre-established parameters to formulate the problem for the optimiser to solve. These are the following:

- **Objective function:** the objective function represents the metric that distinguishes the designs between the optimisation process iterations. The usual is to try to minimize this function and the problem formulation is written this way. However, if a maximum of a function wants to be achieved, it can be also written in terms of a minimization. One example of this function can be the range of a UAV, that is desired to be maximized in the optimal solution.

- **Design variables:** these variables define the system and the optimiser has the freedom to change them within defined bounds (or without any bounds), independently from each other, between each iteration, so that they can define the final optimum design. The choice of the design variables is, in general, free and not unique, although it must be taken into consideration that the design variables should be independent to avoid creating an ill-defined problem since there would be an infinite number of solutions that would lead to the same design [24]. Taking as example a simple symmetric wing with constant chord, the design variables of this system can be the span and chord, since these can define the wing shape. However, using the aspect ratio would lead to a an ill-defined problem since for a specific aspect ratio, there are infinite combinations of span and chord.

- **Constraints:** the constraints are functions of the design variables which constraint the domain to obtain an optimal solution. The region of the domain that satisfies all constraints is called the *feasible region*. The constraints can be either equalities or inequalities, although some care must be taken in order to avoid the domain to be overconstrained and no solutions to be possible. So, the number of equality constraints must be less than or equal to the number of design variables

[24]. An example of a constraint can be a maximum allowed Von Mises stress over a wing structure domain.

Given this, the general structural optimisation problem can be stated as

$$\begin{aligned} \text{minimize} \quad & f(v, u_1, ..., u_{n_l}) \\ \text{w.r.t.} \quad & v, u_1, ..., u_{n_l}\,, \\ \text{governed by} \quad & R_i(X^N(v_G), v_M, u_i) = 0\,, \\ \text{subject to} \quad & g_i(v, u_i) \leq 1 \end{aligned} \tag{3.13}$$

where $f(v, u_1, ..., u_{n_l})$ is the objective function, $g_i(v, u_i)$ is a constraint vector for the ith load case, up to a total of n_l, $x = (v_G, v_M)$ are the design variables, divided as geometric and material design variables, respectively, $X^N(v_G)$ are the nodal locations, u_i are the state variables for the ith load case and R_i are the finite-element residuals.

Types of algorithms

Having set the optimisation problem with the previously described requirements, there are two types of approaches for the optimisation process: gradient-based or gradient-free algorithms. As the name suggests for the first approach, there is the need to compute gradients, either of the objective function or the constraint functions with respect to the design variables. These are very computationally expensive to calculate and many methods have been developed to make them more efficient to calculate. Kennedy & Martins [51] and Kenway et al. [52], for example, used a gradient-based algorithm for an aerostructural optimisation of a wing and a wide-body transport aircraft (Fig. 3.8), respectively, due to the large number of design variables (thousands). The most important aspect in these cases was that the derivatives were obtained by the adjoint method. Another use for this type of gradient-based methods is given by Werter & De Breuker [53] by using a globally convergent method of moving asymptotes (GCMMA) to minimize a wing weight with respect to some lamination parameters and the laminate thickness. One of the key aspects in this case was that the derivatives were obtained using the direct method and with the use of analytically obtained sensitivities of the objective and constraints' functions with respect to the design variables.

Gradient-free in contrast, needs no information about the function gradient, which is an advantage when functions are not smooth or continuous. These type of methods can have both a deterministic or stochastic base. Some examples of this approach in composite structures optimisation can be seen in [30], where Kilimtzidis et al. used an Ant Colony Optimisation stochastic algorithm due to the objective and constraints' functions being of the black-box type and the design variables discrete. This is one of the main advantages of this type of methods since no information of the function behaviour is required. Similarly, Bramsiepe et al. [54] also used a stochastic method, a genetic algorithm, to optimise the stacking sequence of a composite structure. Due to the nature of this mentioned methods being based on evolutionary strategies, they are heuristic. The main disadvantage however, of this type of algorithms

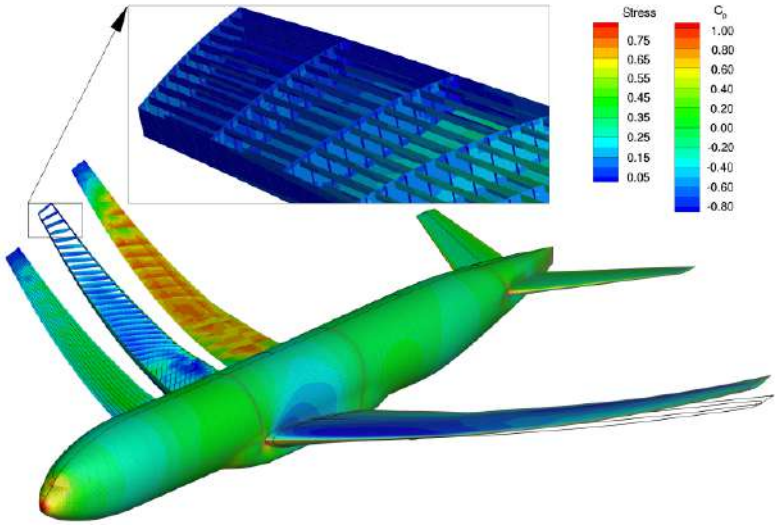

Figure 3.8: Common research model aerostructural solution at Mach 0.85; CFD solution at 1g shown on the right, and structural model and solution at 2.5g shown on the left. [52]

is that they require a very high number of function evaluation [53], which scales with the dimension of the problem (number of design variables).

Gradient-Based Methods

In the context of this work, the gradient-based optimisation seems the most favourable approach since the number of design variables is equally as high as the ones in the above examples, which used the same method. One of the most commonly used approaches to solve the optimisation problem is recurring to a sequential quadratic programming method. One great example is the Sequential Least Squares Quadratic Programming method (SLSQP) which uses the Han–Powell quasi-Newton method with a BFGS update of the B-matrix and an L1-test function in the step-length algorithm [55]. This method approximates the Lagrangian to a quadratic function and linearizes both equality and inequality constraints [24, 55].

A study performed by Zhoujie et al. [56] showed that, for a multi-dimensional Rosenbrock function, the SLSQP algorithm performed the best among several other gradient-based and -free methods, converging the fastest, with the lowest number of function evaluations. Not only that, but both this algorithm and the Sparse Nonlinear Optimiser (SNOPT) performed the greatest when obtaining the minimum C_D when changing the wing twist or shape. This result was especially good using the adjoint method for the derivatives. This SLSQP method is commonly used in aerodynamic shape optimisation [57], airfoil shape optimisation problems [58] as well as aerostructural problems [59].

Having the optimisation algorithm, the following step is choosing and adequate algorithm to compute the derivatives efficiently, according to the problem dimension.

Adjoint Method

To compute the derivatives, the chosen method and the one used by the optimisation framework, is the adjoint method. This method is also used by Kennedy & Martins [51] and Kenway et al. [52] due to the number of objective and constraints' functions being smaller than the number of design variables. On the other hand, if the situation was the opposite, the direct method used by Werter & De Breuker [53] would be the most efficient.

Representing any function of the optimisation problem as f, that depends both on the design variables and the state variables of the problem,

$$f = f(x_n, y_i) \tag{3.14}$$

and representing the residual of the governing equation from the structural analysis as,

$$R(x_n, y_i(x_n)) = 0 \ , \tag{3.15}$$

where x_n are the design variables and y_i the state variables, the derivative of each can be given by the chain rule as

$$\frac{df}{dx_n} = \frac{\partial f}{\partial x_n} + \frac{\partial f}{\partial y_i}\frac{dy_i}{dx_n} \ , \tag{3.16}$$

and

$$\frac{dR}{dx_n} = \frac{\partial R}{\partial x_n} + \frac{\partial R}{\partial y_i}\frac{dy_i}{dx_n} = 0 \ . \tag{3.17}$$

Using a reduced-space (or nested) approach [60] to the problem, the structural analysis of the model is solved repeatedly in each optimisation iteration. This means that the derivatives in Eq. (3.16) are necessary in each iteration. With variational calculus, the partial derivatives from the first expression can be easily obtained. However, from the schematic in Fig. 3.9, it is possible to conclude that the total derivative $\frac{dy_i}{dx_n}$ is computationally expensive since it requires solving the structural model, after imposing a small perturbation in x_n, to obtain y_i.

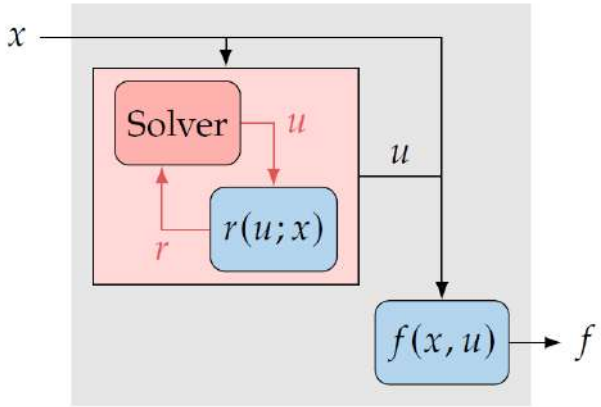

Figure 3.9: Relationship between functions and design variables for a system involving a solver [24]

To tackle this problem of solving the total derivatives, the derivative of the residuals in Eq. (3.17) can be re-written as

$$\frac{\partial R}{\partial y_i}\frac{dy_i}{dx_n} = -\frac{\partial R}{\partial x_n} \Leftrightarrow \frac{dy_i}{dx_n} = -\left[\frac{\partial R}{\partial y_i}\right]^{-1}\frac{\partial R}{\partial x_n}\ . \tag{3.18}$$

Replacing this in Eq. (3.16),

$$\frac{df}{dx_n} = \frac{\partial f}{\partial x_n} + \frac{\partial f}{\partial y_i}\left[\frac{\partial R}{\partial y_i}\right]^{-1}\frac{\partial R}{\partial x_n}\ . \tag{3.19}$$

Defining the adjoint vector as

$$\psi^T \equiv \frac{\partial f}{\partial y_i}\left[\frac{\partial R}{\partial y_i}\right]^{-1}\ , \tag{3.20}$$

yields the adjoint equation

$$\left[\frac{\partial R}{\partial y_i}\right]^T \psi = \frac{\partial f}{\partial y_i}^T \tag{3.21}$$

Solving the adjoint equation to obtain ψ, it can then be replaced in Eq. (3.18) and the derivative of the function f found. This procedure to compute derivatives is called the adjoint method.

From Eq. (3.21) it is possible to conclude that in order to obtain the adjoint vector, this equation needs to be solved as many times as the number of functions f that there are in the optimisation problem. So, this problem complexity scales with the number of constraints. In contrast, the direct method, previously mentioned, takes an alternative approach to Eq. (3.19) since instead of solving for ψ, it solves directly Eq. (3.18) to obtain $\frac{dy_i}{dx_n}$. In this case, this equation is solved as many times as the number of design variables that there are on the system.

It can than be concluded that when there is a distinct difference between the number of constraints and design variables in a problem, the choice of these methods is important. In the particular case of this work, since the problem involves a lot more design variables than constraints, the adjoint method proves to be the best option.

Chapter 4

High-Fidelity Computational Structural Mechanics

In this chapter, the steps for the CSM analyses and optimisation are firstly presented for a better understanding of the workflow. Then, a brief description of the CSM solver is given to know the main performed tasks. Finally, a wing structure test case is performed with a Common Research Model as a proof of concept.

4.1 CSM Analyses' Steps

From the CAD file containing the geometry information of the wingbox to be evaluated up to the output results of the finite element analysis, and the posterior optimisation, a sequence of steps need to be followed and different software used, as presented in Fig. 4.1.

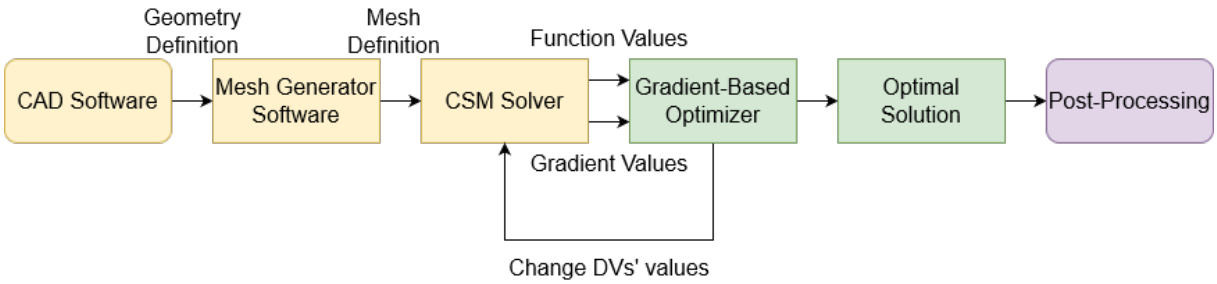

Figure 4.1: Flowchart of the structural optimisation framework with highlight in yellow of the structural analysis components

Firstly, the geometry defined in the CAD needs to be exported as a file with a specific compatible format to be read by a mesh generator software. This geometry definition file contains information about the nodes location, elements identification and nodes which define them and the type of elements used. This is fed into the CSM software so that the finite element model can be used with that discretization.

The CSM software used in this work is TACS (Toolkit for the Analysis of Composite Structures) [50],

an open-source FEM solver. In TACS, load cases are set to condition the problem before it is solved and boundary conditions imported from the mesh definition file. In gradient-based optimisation iteration, the TACS software provides the required function values and gradients, which are then used by the optimiser to iterate until the optimum solution for the intended problem is found.

4.2 Pre-Processing of Lifting Surfaces

The geometry definition and mesh generation of lifting surfaces, require a few software to be used, which are briefly described next.

4.2.1 Geometry Definition Software

To generate the geometry files, containing the necessary information to afterwards create a mesh, different software can be used, depending on the required level of detail. For simple wings, where no control surfaces are taken into account, and the geometry is simply an extrusion of an airfoil with a certain incidence, dihedral and sweep angles, as well as a certain chord distribution, a great tool to use is pyGeo [61]. This python package allows for CAD-free geometry creation and manipulation where a simple script with some wing and airfoil parameters can generate the IGES files necessary for the mesh generation. An excerpt of the pyGeo script is shown in listing F.1 in Appendix F.1.

In contrast, where higher definition and many detail is indeed required in the geometry, the use of CAD software like SolidWorks® [62] is mandatory. Some of these cases include the addition of certain holes on the wing interior for cables to run through and complex shapes that are necessary to incorporate certain components in the wingbox.

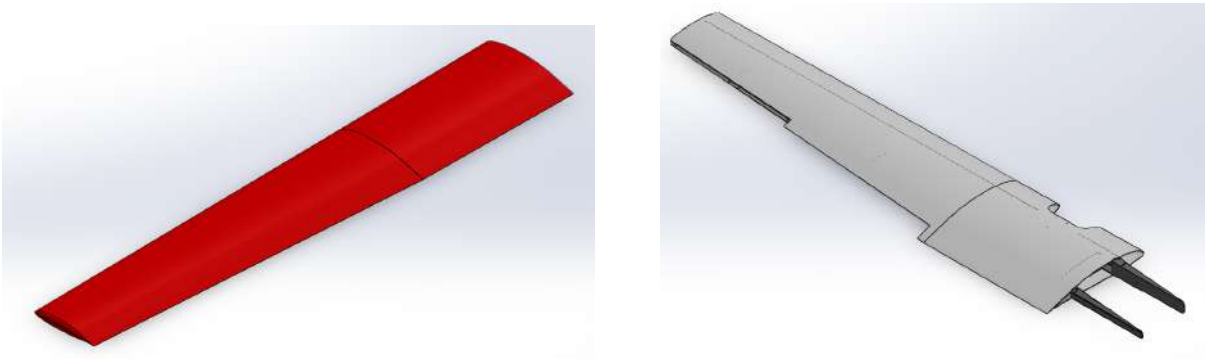

(a) Example of geometry generated with pyGeo

(b) Example of geometry generated with SolidWorks

Figure 4.2: Examples of geometries defined using different software

4.2.2 Mesh Generation

The next step in the pre-processing stage is to generate the desired mesh, given the geometry. Similarly to the geometry definition software, for meshing, according to the level of detail, different options are available.

The best combination for pyGeo is pyLayout. It is a python package that contains several classes that enable parametric generation of finite element models of wingboxes. pyLayout creates the mesh, given the number and position of spars, ribs and stringers in a python script. In the areas formed by the boundaries of each element of the wingbox (represented with the different colours in Fig. 4.3 a)), designations are set that help the structural solver identifying the design variables. Also, there is a good control over the mesh refinement since the number of elements in each spanwise, chordwise and upwards direction is given. An excerpt of the pyLayout script is shown in listing F.2 in Appendix F.2.

For more complex geometries, local refinements and overall better control of the mesh properties, softwares such as Simcenter™FEMap™[63] and Altair® Hypermesh® [64] are used (Fig. 4.3 b).

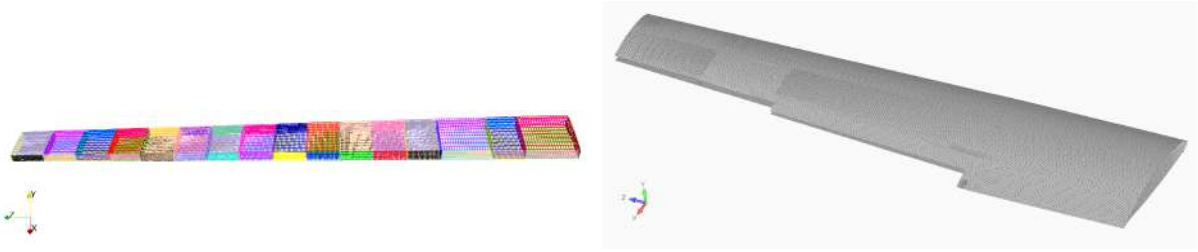

(a) Example of mesh generated with pyLayout

(b) Example of mesh generated with FEMap

Figure 4.3: Examples of meshes created using different software

4.2.3 Smeared FSDT Approach

To model the composite material that composes the wingbox, a smeared approach is used [65]. This method describes the composite using fractions of plies (f_{θ_i}) and their respective angles (θ_i), instead of the complete description on the layup. It is necessary to provide the elastic and strength properties of each ply as well as the total thickness of the laminate. With these, the global stiffness matrix $\overline{Q}$ is weighted with each ply fractions of a certain orientation, instead of each ply thickness. A visual diagram of the geometric parameters necessary for this model is presented in Fig. 4.4.

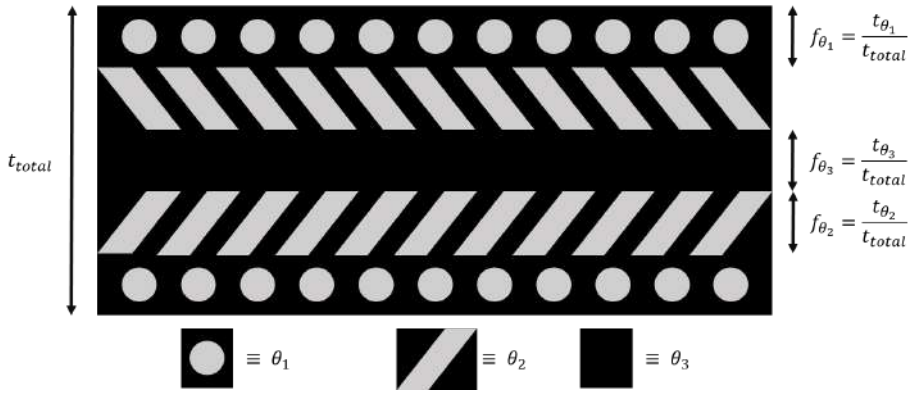

Figure 4.4: Composite representation with the necessary parameters to define the smeared model (matrix in black and fibres in grey)

Using this approach, the problem complexity reduces since the optimisation process does not have to take the angle of each ply and the laminate thickness (taking into account each ply thickness), as

design variables. It fixes the proportions of each angle and only controls these angles θ_i and the total laminate thickness t_{total}.

4.3 TACS Architecture

The TACS is used for analysis and design optimisation of thin-shell structures manufactured with laminated composites or metallic alloys. To give an overview and an understanding of how is the problem resolution workflow, a flow chart is presented in Fig. 4.5.

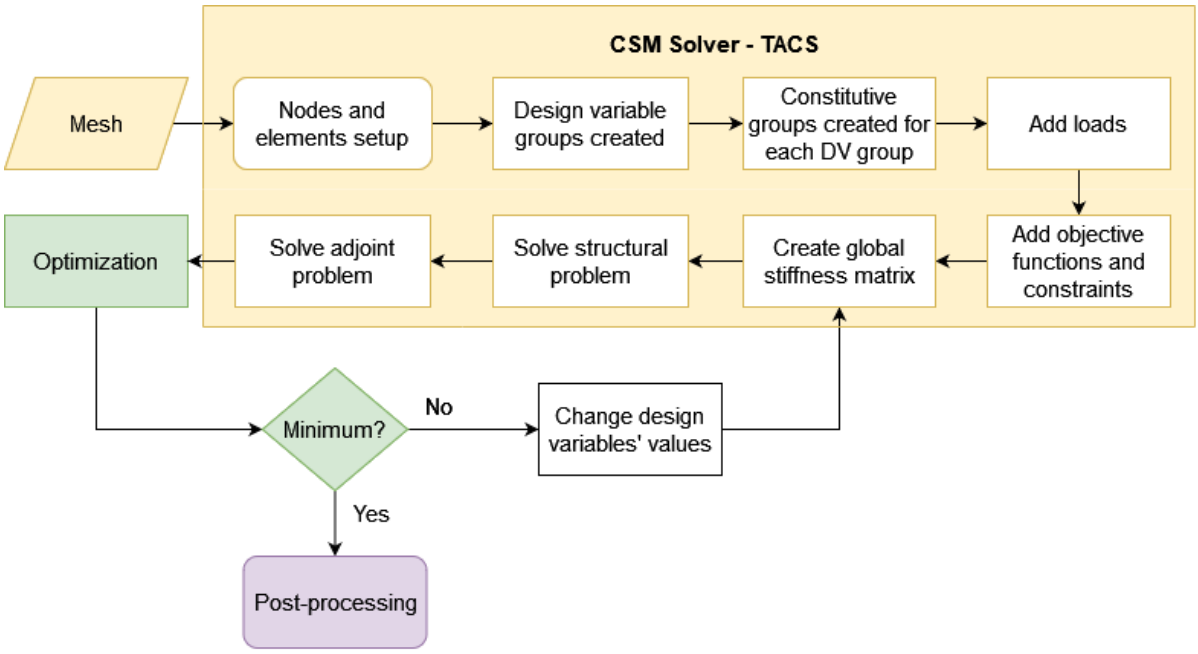

Figure 4.5: Flow chart of the steps to solve an optimisation problem

It starts by importing a file with the wingbox mesh information, as well as the problem constraints. In this file, certain sections of the wing are assigned a property name. For example, the elements that form the front spar have a property name of FRONT_SPAR. After this, a setup is made where nodes and elements are read from this file. Then, using the properties' names, the various wingbox parts can be divided in design variable groups. Followed by this, the constitutive models are assigned to each group. The most important aspect of the property names is the fact that, using them effectively, it is easy to control constitutive models and design variable groups since they can be called by that assigned name.

After this, all loads are given to the model, either by manually inserting values to certain wingbox locations or by giving TACS a file generated by ADFlow [66] which translates the aerodynamic forces into nodal forces in the structural mesh. With this settled, remains the necessity of defining the objective and constraints' functions for the optimisation problem. Then, the global stiffness matrix is built and a solution obtained. Using the optimiser, if the solution found was the optimal, the problem ends. Otherwise, the design variables' value changes, a new stiffness matrix is built and the process repeats, as represented by the loop in Fig. 4.5.

In Appendix B, some guidelines of how the TACS software works internally are given.

4.3.1 Standard Constraints' Functions

TACS comes with standard pre-implemented functions that can be used as constraints. These include failure, displacement and adjacency constraints [67].

Since it is not possible to obtain a gradient of a function that retrieves the maximum failure indexes across all points in which it is calculated, the Kreisselmeier-Steinhauser (KS) aggregation function [68] is used to convert the discrete nature of the maximum failure index function into a continuous and smooth function, allowing for a gradient-based optimiser to use it,

$$\text{KS} = \frac{1}{\rho} \ln(\sum_{l=1}^{n_g} \exp(\rho g_l)) \tag{4.1}$$

where ρ is a tolerance/weight parameter, n_g the number of failure constraints and g_l the lth failure constraint function. This KS function can be also used to aggregate the displacements of each point in a region, to control their maximum.

Finally, regarding the adjacency constraint, this function allows adjacent design variable groups to have a relation between the selected design variables. In the context of this work, this can be used to limit the thickness and ply angle differences of certain wingbox components.

4.3.2 Custom Developed Constraint Functions Added to TACS

For the optimisation process to be successful and comply with Tekever's requirements, manufacturing constraints are necessary so that the line of production and the manufacturing techniques used remain the same, while the parts themselves are optimised.

To achieve this, some of these constraints had to be developed and incorporated into TACS. These are the orthogonal plies, the monotonic thickness and the wing tip torsion.

Orthogonal Plies Constraint

Since the majority of CFRP components that are produced by hand layup use woven fibres for an easier handling, it is necessary to take this into account. The way it was found possible was by constraining a pair of plies to have a difference of 90° between them, ensuring they are orthogonal like woven fabric.

The way it was modelled in TACS was: check for adjacent areas of the same component, in which the optimiser locally changes the design variables; then, for each area, impose an inequality constraint making each design variable, corresponding to the ply angle, have an absolute value of the difference between 89.4° and 90°. Although computationally this is modelled as an inequality, in reality, this is equivalent to an equality constraint since such small difference between the inequality bounds is equivalent to the dimensional accuracy of the hand layup, when placing the fibre cloths.

In Appendix E.1, excerpts of the implemented code in TACS are given.

It is also important to note that, the strength of a $[0°/90°]$ layup with unidirectional fibres (Fig. 4.6 b)) should be different than the use of the weaving pattern (Fig. 4.6 a)), making this approach an approximation.

(a) Plain weave pattern trying to be modelled (Credit: EasyComposites)

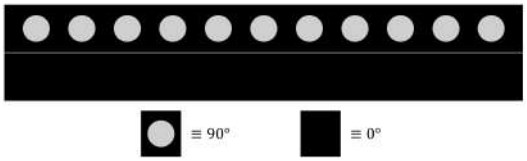

(b) Representation of the computational implementation

Figure 4.6: Real vs computational model of the woven carbon cloth

Monotonic Thickness Constraint

Another necessary constraint to add was the monotonic thickness, to ensure that the fibres are continuous in the spanwise direction. Since the fibre fabrics are extended from the wing root up to the tip, if the thickness is lowering from the root to the tip, the fibre is getting cut before reaching the tip, as represented in Fig. 4.7. If, however, the thickness does not have a monotonic behaviour, the fibres would not be continuous from the root and a patch of cloth (represented in Fig. 4.7 in red) would be needed at the wing tip. This would lead to a weak spot in the area of minimum thickness.

(a) Desired layup of fibre

(b) Non desired layup of fibre

Figure 4.7: Monotonic thickness

To have this constraint working properly, it was made sure, when defining the design variable groups, that they were enumerated from root to tip so that, when their indexes were extracted and placed in ascending order, the higher number corresponds to a group further away from the root. This is important since, the way this constraint was modelled was by checking, in the desired component to have the

decreasing thickness from the root to the tip, the difference between thicknesses ($t_i - t_{i+1}$) and constrain it to be positive.

There is a similar function in TACS that applies adjacency constraints to make sure a certain design variable in adjacent groups does not exceed a desired value (Δ_{max}). However, since that Δ defines the upper and lower bound of the inequality, it does not ensure that the thickness is monotonic. To not change this base function of TACS, and instead add more capabilities, this new constraint was added.

In Appendix E.2, an excerpt of the implemented code in TACS is given.

Otherwise, another possible solution could just be to use the Δ_{max} in the upper bound and limit the lower bound to 0, so that the same difference would always be positive.

Tip Torsion Constraint

Finally, the last and most challenging constraint to be developed and added to TACS was a tip torsion constraint. With the optimisation of the wing, it is expected that the structure becomes more flexible in bending and torsion due to the possible thinning of components. With that in consideration, and since no aeroelastic phenomena, such as divergence or flutter, are taken into account during the optimisation process, a tip torsion constraint was thought to be necessary. The optimal solution is expected to have a limited possible amount of wash in at the wing tip under the aerodynamic load, in contrast with an optimised wing without this constraint, under the same load.

The tip torsion (γ) is represented in Fig. 4.8 then calculated

$$\gamma = \arctan\left(\frac{(y_1 + v_1) - (y_2 + v_2)}{(|x_1 - x_2|)}\right), \tag{4.2}$$

where x_i and y_i are the x and y coordinate of the ith point, respectively, and v_i is the y displacement of the ith point.

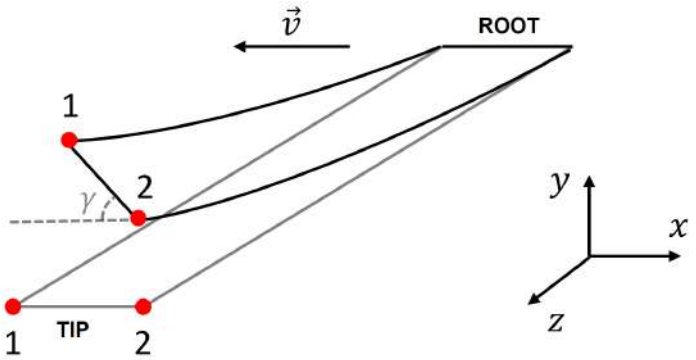

Figure 4.8: Representation of the tip torsion

In Appendix E.3, excerpts of the implemented code in TACS are given.

4.4 Post-processing

As output of the structural optimisation problem, a file is written containing information about displacements, stresses, strains, failure index, material thickness and ply orientation. To have a visual interpretation of this data, software like ParaView® [69], which is open-source and Tecplot 360™[70], which is commercial, can be used. Since more support was found regarding Tecplot, this was the one chosen for this work.

To read the information from the file, it needs to be converted into a format that this software can read, such as .plt. Some of the most interesting plots that can be drawn using Tecplot are the deformed view of the wingbox, which allows the user to understand if the wing deflection is adequate for certain loads (Fig. 5.12) and coloured representation of the failure criteria in the wingbox, showing the most problematic areas (Fig. 5.14, for example). Not only this but analysing these plots is important to check the validity of the results. Critical thinking is necessary and a plot of the one of the stress components along the wing, for example, can help understand if areas that are supposed to be under compression (like the upper skin of the wing under cruise conditions) are indeed behaving as predicted.

Finally, other important result is the wing tip deflection, since it reflects the aeroelastic behaviour of the wing. Given this value, some interpretations can be done regarding to the wing divergence.

For the optimisation results analysis, checking that the optimisation finishes with the adequate termination condition and not by reaching a limit of iterations, or even with any type of error, is required. Following that, it in necessary to observe if the objective function presents a converging behaviour to a minimum, while respecting the defined constraints. Finally, it is important to confirm that all the design variables are within the defined boundaries and if, qualitatively, present adequate results.

4.5 Test Case

To validate the constraints added and developed to the base version of TACS, as well as test the framework, a test case was necessary. In this case, a plate with thickness of $2.5\,\mathrm{mm}$ was subject to a normal distributed load of $300\,\mathrm{N}$ (in the y direction) and clamped at the edge in red, as presented in Fig. 4.9 a). This induces a torsional deformation as shown in Fig. 4.9 b).

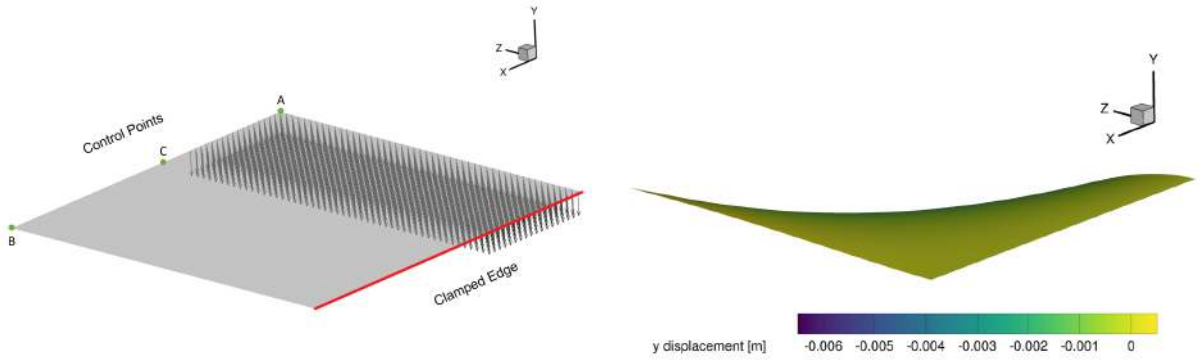

(a) Load configuration for the plate test case

(b) Displacement results for the plate test case

Figure 4.9: Plate test case

It was assumed that this was a CFRP plate, with typical properties presented in Tab. 4.1 and both a $[0°/90°]$ and $[-45°/45°]$ layup being the $0°$ reference the z axis.

Table 4.1: Density and physical properties of CFRP ply

Density	$1700\,\mathrm{kg\,m^{-3}}$
Young's modulus (fibre direction)	$175.8\,\mathrm{GPa}$
Young's modulus (transverse direction)	$11.0\,\mathrm{GPa}$
Shear modulus	$3.93\,\mathrm{MPa}$
Poisson ratio	0.023
Tensile and compressive strength (fibre direction)	$2.58\,\mathrm{GPa}$
Tensile and compressive strength (transverse direction)	$45\,\mathrm{MPa}$
Shear strength	$136\,\mathrm{MPa}$

A simple mass minimization problem similar to the described in Sec. 6.1 with both starting points was formulated using the 3 coloured areas from Fig. 4.12 as design variable groups, where the thickness and ply orientations changed. The imposed constraints were: the desired torsion was set to be about $0°$; the KS failure function (described in Sec. 4.3.1) not allowed to surpass the value 1; the thickness had to decrease from the area with the load to the opposite edge; the angle of each ply had to be the same for each design variable group; and the pair of plies had to be orthogonal to behave similarly to woven fabric. In terms of optimisation parameters, they are presented in Sec. 6.1.

The optimisation of the plate resulted in a mass reduction of 27.0% for both initial layups, which is due to the equal decrease in the thickness of the plate. Therefore, no local minima was found in this problem.

The vertical displacement results for the optimal solution, under the load previously mentioned, at the control points A, B and C (represented in Fig. 4.9 b)) can be inspected in Fig. 4.10, with the x axis raging from 0 (position of point 2) to 1 (position of point 1). Across that edge, opposing the fixed one, the displacement is about the same for both solutions being approximately $1.2\,\mathrm{mm}$. The fact that this displacement is practically constant reflects the imposed $0°$ torsion condition demonstrating that it is satisfied. The possible small differences (not noticeable in the plot) come from the fact that the torsion constraint is modelled as an inequality constraint with upper and lower bounds instead of an exact equality constraint.

Regarding the final thickness of each design variable (DV) group, it can be observed in Fig. 4.11. As expected, the area which carries the load increases its thickness to about $5\,\mathrm{mm}$ to increase its torsional stiffness until the optimisation constraints are satisfied. Also, it can be visually inspected in Fig. 4.12 that the decreasing thickness constraint also worked as desired since its value is decreasing from the load carrying area to the other edge. Finally, the obtained optimal layup was the same as the original, $[0°/90°]$ for both starting layups which also satisfies the demanded orthogonality between plies.

Having concluded this optimisation with satisfactory and expected results for this simpler problem, all added constraint were validated and the framework tested, during all stages from the CAD and pre-processing of the plate up to the post-processing of the optimised results.

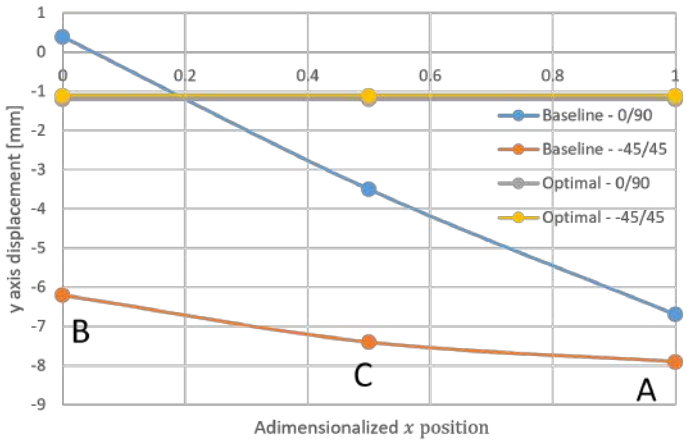

Figure 4.10: Displacement at the edge with control points 1, 2 and 3

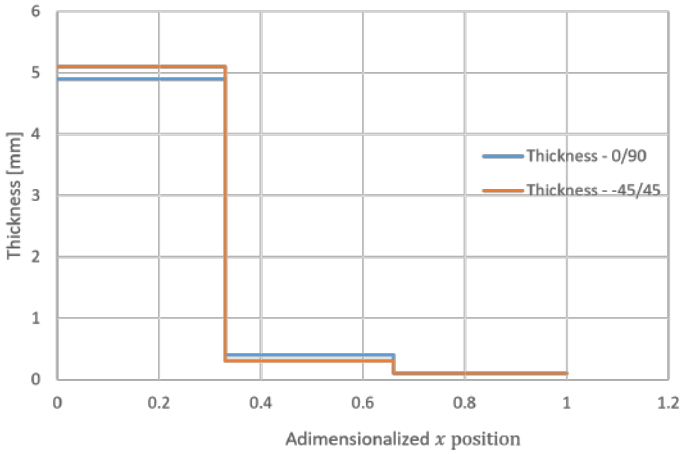

Figure 4.11: Thickness for each DV group

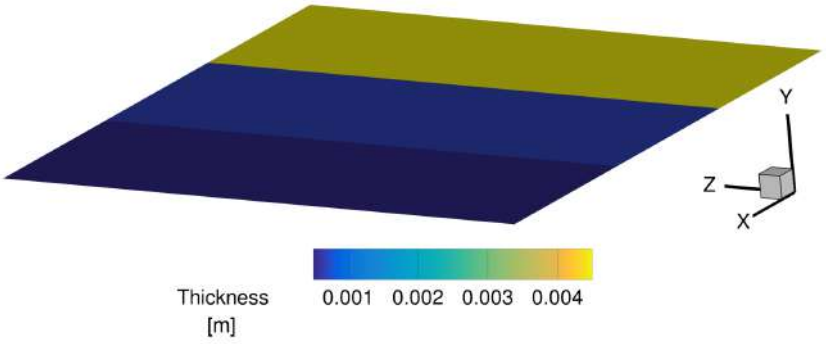

Figure 4.12: Optimal solution of the plate's thickness for $[0°/90°]$ baseline

Chapter 5

Tekever AR5 Wing Structural Analysis

In this chapter, a baseline analysis of the Tekever AR5 wing is performed. To do this, the material characterization of all its components is presented, as well as a mesh convergence study to choose the appropriate mesh for this analysis and the optimisation, performed in Chapter 6.

5.1 Baseline UAV Definition

The baseline and start of the optimisation process of the Tekever AR5 is its wing, since it is the main component of the UAV and is subject to a large range of loads. Fig. 5.1 shows AR5's top view and respective reference frame used throughout its analysis together with a simplified representation of its internal structure.

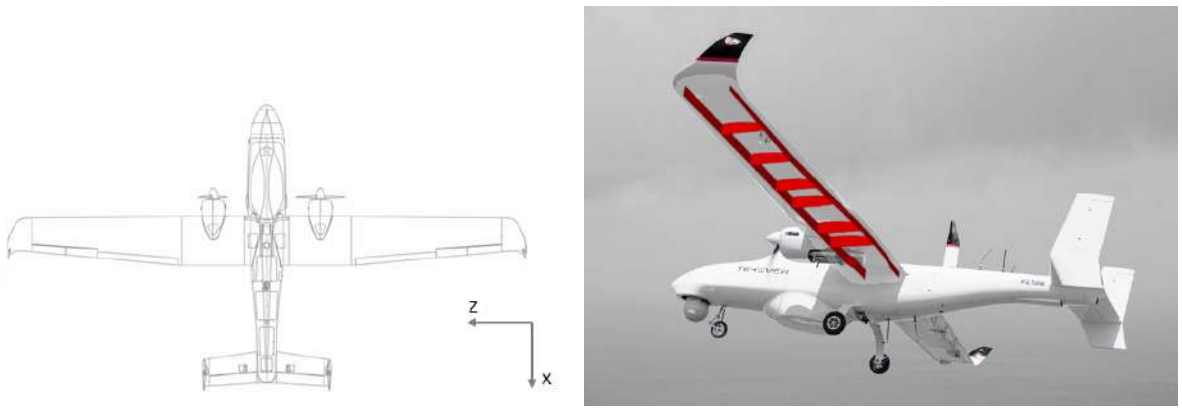

(a) AR5 top view (b) Simplified representation of its internal structure

Figure 5.1: Tekever AR5 with representation of simplified wing internal structure

The simplified and more detailed internal wingbox structure models are represented in Fig. 5.2.

The wingbox can be parametrised in several ways. To do this, some groups within the structure are created, sharing the same parameters. Afterwards, in the optimisation process, these will vary equally. In Fig. 5.3, the groups can be observed in different colours.

The parameters that define each group are thickness, type of materials, their proportions and the ply angles. Regarding the position, the wing is also parametrised using the intersection points between the

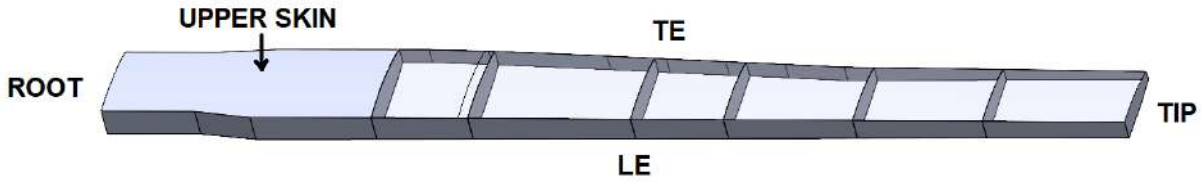

(a) Simplified baseline

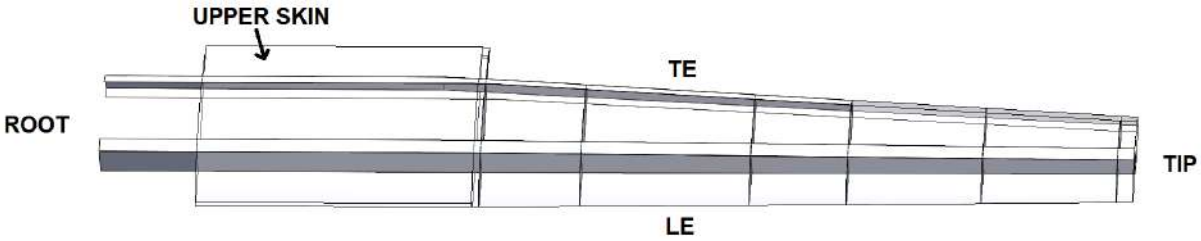

(b) Detailed model

Figure 5.2: Wingbox structure of Tekever AR5

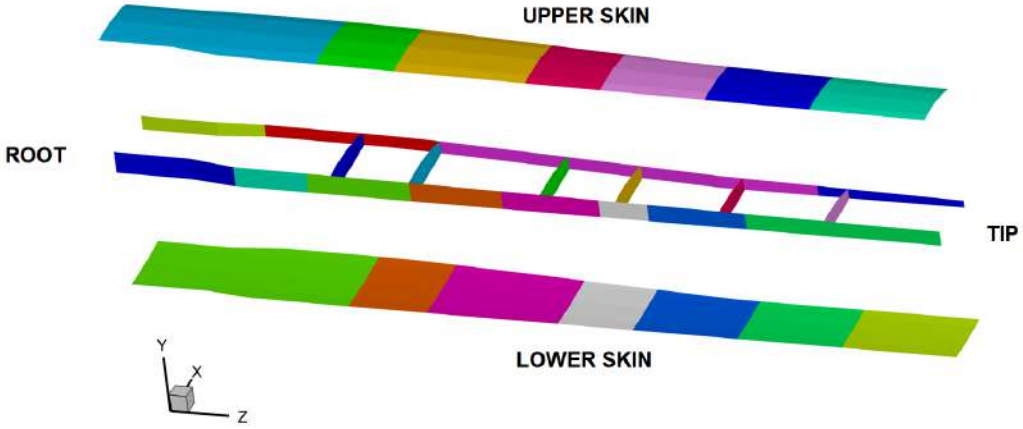

Figure 5.3: Representation of the design variable groups on the simpler wingbox

spars and ribs (which determine the number and position of ribs), as well as coordinate points that define the shape of the spar and its chordwise position. The detailed parametrisation of the AR5 wingbox can be found in Appendix C.1.

5.2 Problem Setup

To setup the structural problem to analyse the Tekever AR5's wingbox, the mesh of the model needs to be created and several parameters need to be established. These correspond to the loads, constraints and material definition.

5.2.1 Wingbox Material Definition

The AR5 wingbox is composed of sandwich composite components with different thicknesses and fractions of core and shell material. A representation of these sandwich components is shown in Fig.

5.4.

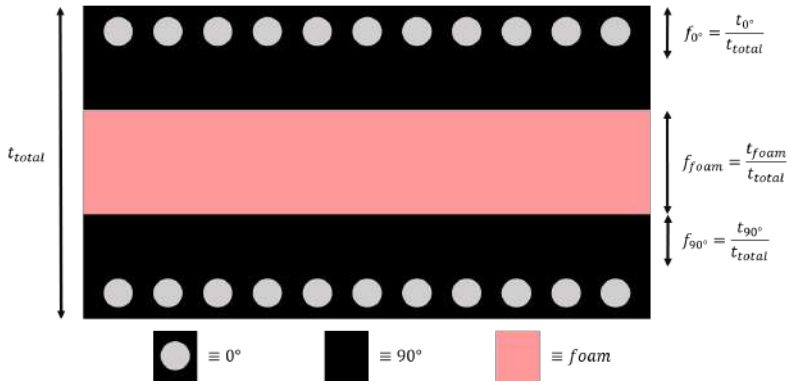

Figure 5.4: Representation of the sandwich composite (CFRP with black matrix and grey fibres and foam core in pink)

The core consists on a low weight rigid foam which gives the necessary stiffness to the wing, with a very low weight. Different versions and proportions of this core are used depending on the wingbox section. A detailed description of its composition is provided in Appendix C.2. The physical and mechanical properties used are summarized in Tab. 5.1. It is important to note that, only the in-plane properties were necessary since the transverse stress is neglected in the first-order shear deformation laminated plate theory. This means that, since the foam core properties in-plane are independent of direction, this material can be modelled as isotropic.

Table 5.1: Foam core properties

Density
Tensile modulus in the plane
Shear modulus
Tensile strength in the plane

For the shell, a Carbon Fibre Reinforced Polymer (CFRP) layup is used with plies of 0° and 90° orientation as a starting solution. Fig. 5.5 shows the direction of the 0° fibre orientation. It is defined by direction 1 of the local reference axis for each wingbox component: for both skins, spars and ribs, corresponding to the z, y and x directions, respectively.

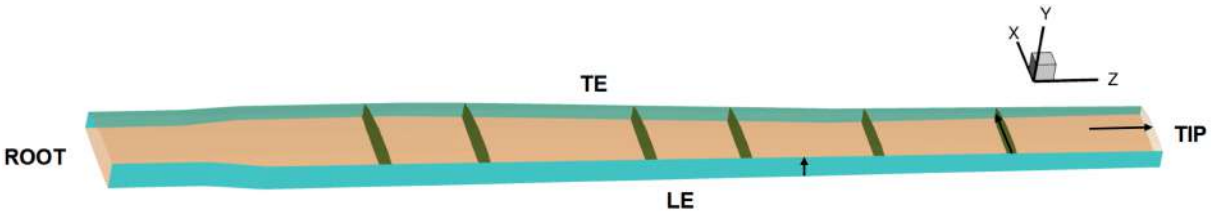

Figure 5.5: Representation of the 0° fibre direction for each wingbox component

A summary of the necessary properties obtained can be seen in Tab.3 and their values in Appendix C.2.

To define the material composed of both the foam and the CFRP in the wingbox, the constitutive

Table 5.2: Density and physical properties of CFRP ply

Density*
Young's modulus (fibre direction)*
Young's modulus (transverse direction)*
Shear modulus
Poisson ratio
Tensile strength (fibre direction)
Compressive strength (fibre direction)
Tensile and compressive strength (transverse direction)
Shear strength

* Obtained from rule of mixtures

model explained in Sec. 4.2.3 is used. The change in thickness of the different components mainly derives from a change in thickness of the foam and not necessarily of the CFRP shell, since the core has the largest fraction (over 80% for the majority of components). A compilation of the core and shell proportions across the wingbox components can be found in Appendix C. However, in TACS, a complete and detailed model of this material is not possible to conceive, mainly due to the fact that the core is fully enclosed by the CFRP, in contrast with the layup in Fig. 5.4 and some properties are not exactly representing the real material. These are the major limitations in terms of material that were encountered and a probable cause for different results between a real test and a computational analysis. Nonetheless, the analysis is performed and an optimisation can be carried out later.

Finally, to acknowledge the possible differences between the mass calculated from the structural model and the real mass of each component, measured by Tekever's quality control team, the error of the model relative to the measured values is given in Tab. 5.3.

Table 5.3: Error of model mass relative to measured mass of AR5 wingbox components

	Lower Skin	Upper Skin	Spars	Ribs	Total
Simpler model [%]	$+19.1^*$	$+26.1^*$	-30.9	-50.0	-1.7
Detailed model [%]	-33.4	-23.9	$+53.5$	-33.5	$+1.6$

* Extrapolated value

It is possible to observe that the calculated total mass is slightly underestimated in the simpler model. Firstly, for the skin mass, an extrapolation was needed to compare the real and model values since due to the simplifications needed for the wingbox meshing, the skin panels that are computed are only present between the spars. Therefore, with those panel's mass, an extrapolation was made to obtain the estimated weight of the real model skin and it is shown in Tab. 5.3. This extrapolation was simply made considering the chordwise position of the spars and would be accurate it the skin panels were straight and parallel to the chordwise direction. For the detailed mesh, this extrapolation was not necessary since all skin panels were considered. Nonetheless, there were still 33.4% and 23.9% less mass than in the measured lower and upper skin, respectively. Since there are a few geometric differences, specially in the simpler model, as well as material properties' differences in both, some discrepancies are present. For example, spar's beam profile in the simpler model is simply rectangular. However, in reality, this is not the case. This means that a good amount of material is not considered, resulting in a underestimation of the mass in the model. In the detailed model, the profile is taken into consideration, making the spar

mass prediction going from an underestimation to an overestimation. Finally, it is important to note that, overall, the difference is negligible (about 2% error for both cases) and does not affect the wing's stiffness directly.

5.2.2 Mesh Generation and Refinement Study

To generate the mesh of the internal structure of the simpler wing model, pyLayout was used. However, some model simplifications were necessary upon the limitations encountered due to the lack of tools in this python library. Nonetheless, the structure is composed by 6 ribs, 2 spars and the skin panels between these. The simplifications include the trimming of the ribs' leading edge at the front spar, the addition of a rear spar section close to the tip and the skin panels are only present between the spars (no leading or trailing edge skin panels).

As explained and exemplified in Sec. 3.6.2, since these components are thin and made with composite materials, it is beneficial to use 2D elements for this mesh. Firstly, 4-node quadrangular MITC shell elements were used. Afterwards, higher order elements, such as 9-node quadrangular elements, were employed.

Considering that the structural model is solved in each optimisation step, as explained in Sec. 3.8, it is important to choose an efficient mesh to compute the most accurate results in the least time possible and using the least amount of computational resources. To make this decision, a mesh refinement study was carried out for the simplified wingbox with 5 meshes, as summarized in Tab. 5.4.

A representation of mesh 1 can be seen in Fig. 5.6. The others are a subdivision of this one, where each element is split into 4.

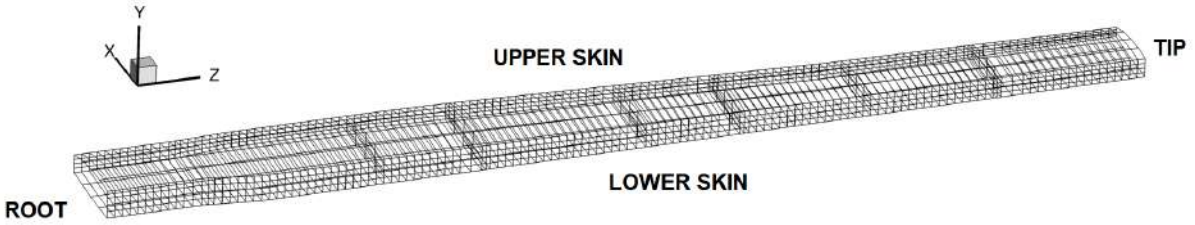

Figure 5.6: Mesh of the Tekever AR5 wingbox simplified

The study consisted in monitoring the maximum displacement in the vertical (y) direction, as well as the x component of the mid-plane stress, in a specific point. In this case, the intersection between the upper skin and rear spar at the tip and the wing root intersection of the front spar and the lower skin, respectively. These results, together with the CPU time and RAM necessary to compute them are plotted against the total number of elements to understand the relation between the mesh sparsity, the results' accuracy and their computational cost. As load condition, the higher stress gradients and displacement values are encountered in a 4g maneuvre. Therefore, the expected loads in that situation were applied to the wingbox to obtain the results presented in this section.

As described in Sec. 3.7, one of the methods to lower the approximation error is to increase the

order of the finite elements used. This meant that, not only bi-linear elements were used in this study, but also higher order ones, to have a comparative view of both types. The obtained values for each mesh are presented in Tab. 5.4 and 5.5 and are visually represented in Fig. 5.7 and 5.8. These results were obtained with a computer using a 16-core processor with 4.5 GHz base frequency and 128 GB of available RAM. Since there were some memory allocation problems, due to the increasingly higher number of nodes with each refinement, all analysis were done using parallel computation between 4 cores, except for mesh 5 with 2^{nd} order elements, which required the use of 13 cores simultaneously.

Table 5.4: Convergence study for bilinear elements

Mesh	Number of elements	Degrees of freedom	Max disp. (Tip Rear Spar - USkin) [m]	Diff.	Stress (Root Front Spar - LSkin) [Pa]	Diff.	RAM per core [GB]	CPU time [s]
#1	2,272	13,476	0.2686	-	60,490	-	0.1	80
#2	9,088	54,180	0.2668	-0.67%	62,450	+3.24%	0.1	584
#3	36,352	217,380	0.2665	-0.11%	64,280	+2.93%	0.1	964
#4	145,408	870,948	0.2665	0.00%	66,089	+2.91%	1.4	964
#5	581,632	3,486,756	0.2665	0.00%	67,936	+2.79%	8.8	1864

Table 5.5: Convergence study for 2^{nd} order elements

Mesh	Number of elements	Degrees of freedom	Max disp. (Tip Rear Spar - USkin) [m]	Diff.	Stress (Root Front Spar - LSkin) [Pa]	Diff.	RAM per core [GB]	CPU time [s]
#1	2,272	54,180	0.2662	-	64,138	-	0.1	56
#2	9,088	217,380	0.2665	+0.11%	65,913	+2.77%	0.1	444
#3	36,352	870,948	0.2664	-0.04%	67,774	+2.82%	1.5	844
#4	145,408	3,486,756	0.2665	+0.04%	69,663	+2.79%	6.8	1248
#5	581,632	13,953,060	0.2665	0.00%	71,298	+2.35%	9.9	10257

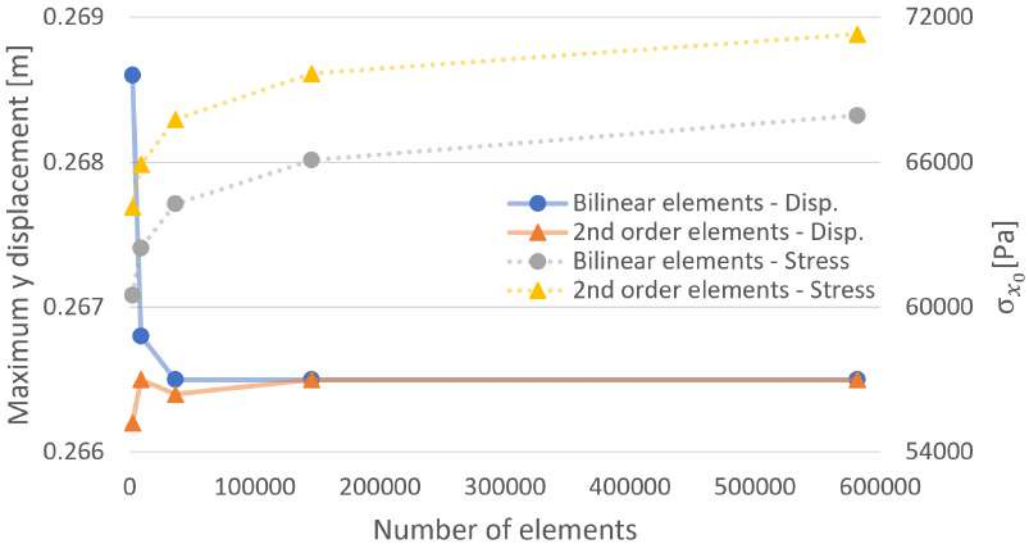

Figure 5.7: Mid-plane stress (σ_x^0) at root and maximum y displacement at the tip for each mesh and element type

Observing Fig. 5.7, it is possible to conclude that both the stress and maximum displacement converge with increasing number of elements in the mesh. This is the expected behaviour since with

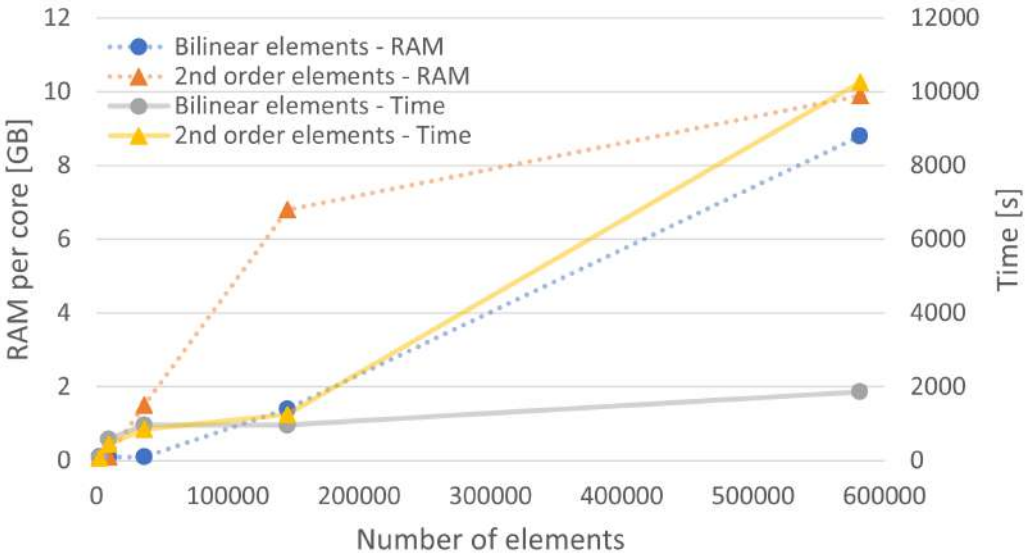

Figure 5.8: Computational time and RAM necessary for each mesh

increasing level of refinement, the results should have lower approximation errors (Sec. 3.7). Quantitatively, after the 4^{th} mesh of bilinear elements and the 3^{rd} mesh of 2^{nd} order ones, the difference of displacement and stress results between these meshes and the following are lower than 0.04% and 2.80%, respectively. Although this last value might be relatively high, it must be pointed that the chosen location to monitor the stress is a stress concentration point. This means that, to tightly converge in that spot, it would be better to refine it locally. However, since that point is not of particular interest and reinforcements are added in the real wing that cannot be modelled, the mesh is left as it is since the remaining results in other points of the mesh are already converged.

Regarding time and memory usage, their behaviours are the expected. With more elements and consequently, a larger amount of nodes and degrees of freedom, the amount of equations to be solved increases. Therefore, the cost to solve the structural problem also increases with the mesh refinement level. However, in the particular case of mesh 3 and 4 with bilinear elements, the time it takes is the same. Considering that this behaviour is inconsistent and a complete surprise, an intermediate mesh was also tested, with $71,168$ elements and $482,052$ DoF which, once again, took exactly the same time to conclude the analysis. One possible explanation for this is at the code level, where within that range of number of bilinear elements, the problem becomes non-sensitive when solving the equation $[K]\{u\} = \{F\}$.

Another detail that is observed is that, for meshes of different type of elements, with the same amount of DoF, the CPU time is actually decreased for the higher order mesh. The reason for this behaviour is that for the same number of nodes, problems with higher order elements benefit from super-node identification, which facilitate the factorization of matrices [50, 71].

To choose the most efficient mesh to obtain the structural results from and use during the optimisation process, the criteria was: it had to be converged and it should be the one that takes the least time and memory to solve. Looking at the Tab. 5.4 and 5.5, it was concluded that the mesh meeting these criteria was mesh 4 with bilinear elements or mesh 3 with 2^{nd} order ones. The computational cost between these

two meshes is similar. However, the convergence behaviour is different since the difference between stress results of the bilinear meshes behaved monotonically decreasing while the 2^{nd} order ones did not. From mesh 2 to mesh 3 the difference increased and only started to decrease again from mesh 4 onwards. It could then be said that although the deviation in the results was about 2.8% for the mesh 3 with 2^{nd} elements, which was considered acceptable, its behaviour is not totally convergent. Additionally, the stress values are higher using the 2^{nd}. Considering that the point monitored has stress concentrations as previously mentioned, this could lead to oversized final optimal solutions. The failure index in this point would have much higher values than in reality. Therefore, this mesh was rejected and the next most efficient choice was mesh 4 with bilinear elements.

Following this study, a comparison between the detailed and simpler wingbox results was made. In order not to repeat the same study for the other mesh, the element size from this study's choice was translated to the other mesh. Tab. 5.6 shows the size of the quadrangular element edges in each direction and the average. It is important to note that, in some areas, the size varies slightly due to some refinements. Nonetheless, the average from the simpler mesh was the value used for the detailed one.

Table 5.6: Element sizes for both meshes

Direction	Simplified	Detailed
x	$0.0094\,\mathrm{m}$	
y	$0.0019\,\mathrm{m}$	-
z	$0.0031\,\mathrm{m}$	
Average	$0.0048\,\mathrm{m}$	$0.0048\,\mathrm{m}$

This resulted in a mesh with $212,589$ elements and $200,312$ nodes, represented in Fig. 5.9, that was only possible to be created by using a commercial software such as the ones described in Sec. 4.2.2 for complex geometries. The increase in number of elements and nodes is due to more surface area and detail in the geometry.

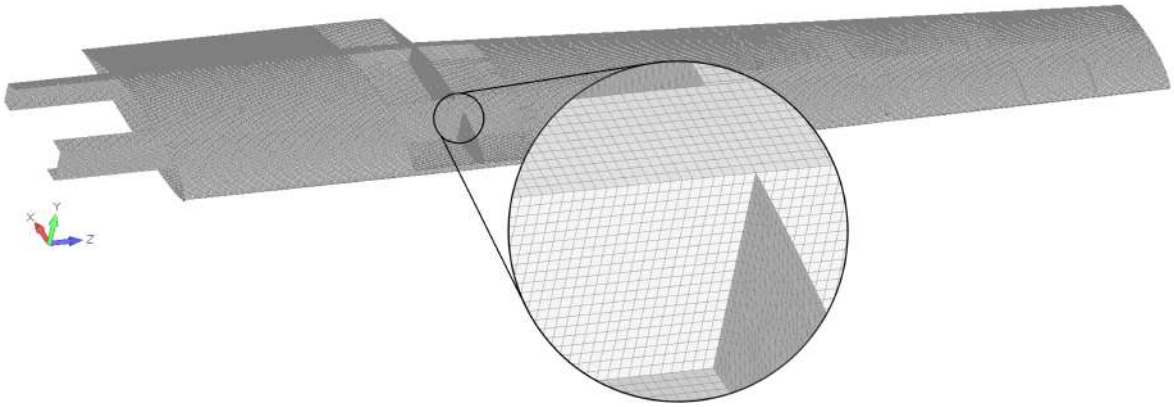

Figure 5.9: Mesh of the detailed geometry

Given that the geometry has more curvature, specially at the ribs, some triangular finite elements appeared when trying to mesh. TACS does not support analysis with mixed elements within the same design variable group, therefore most of the triangular elements were removed locally refining some

areas. By doing so, most of the remaining triangular elements moved to the ribs and if tried to further refine, the other components would have again mixed elements within them. The final decision was then to mesh the ribs using 3-noded triangles and the remaining components with 4-noded quadrangular elements.

5.2.3 Load Cases and Constraints

Having the meshes set, to test the wing and analyse its baseline behaviour, three load cases were used. These are:

1. **Specific loads across the wingspan to simulate a wing bend test + wing weight:** The bending test performed by Tekever consisted of clamping both the right and left wing roots, and, with these wings upside down, weights were placed on the lower skin. The location of the weights is shown in Fig. 5.10 and their respective values in Tab. 5.7.

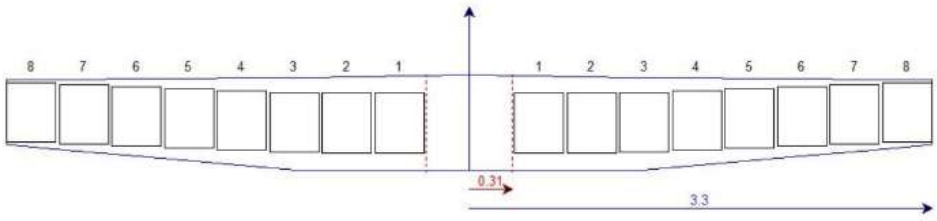

Figure 5.10: Location of the static loads

Table 5.7: Load's value

Location	1	2	3	4	5	6	7	8
Value [N]	246.2	153.0	273.7	255.1	232.5	217.8	193.3	244.3

2. **Cruise:**

   Since most of the time during its operation, the UAV is flying at cruise condition, it is important to check deflections and possible failure points in the wing during such load condition. The lift equals the weight in this case (Fig. 5.11) and its distribution is obtained directly from an aerodynamic analysis using ADFlow [66] that outputs a file force that is fed into TACS. Not only that, but a safety factor is also given when running the problem, which was set to 1.5.

3. **4.0g Maneuvre:**

   The UAV has a predefined flight envelope so failure is expected at higher loads. To make sure the wing supports the maximum allowable loads within the flight envelope of the AR5, a 4.0g manoeuvre is studied. In this case, the lift is four times larger than the weight. Note that, even though this corresponds to a manoeuvre, the influence of the control surfaces is not taken into consideration in the analysis. The input forces' file is, once again, generated by ADFlow after running an aerodynamic analysis and the same safety factor used for cruise condition was also implemented in this case.

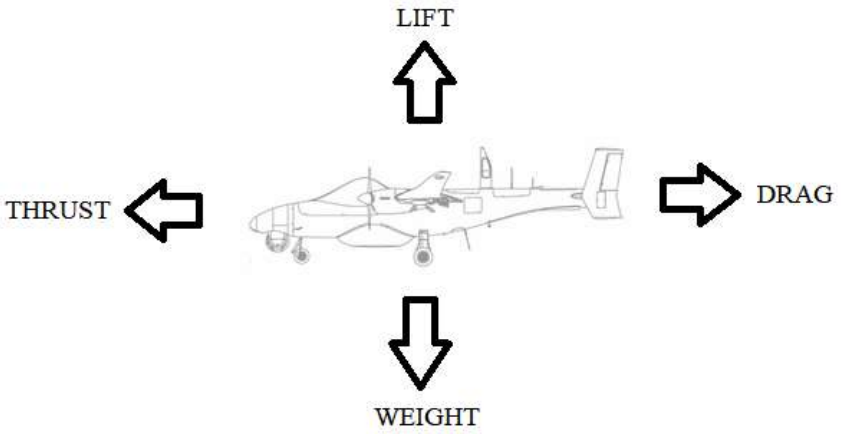

Figure 5.11: Representation of forces actuating on the AR5

To fully define the model for the following static analyses, constraints need to be set. For the simplified mesh, the wing root was assumed to be clamped so the nodes in the root plane had both translations and rotations DoFs fixed to zero. For the detailed mesh, the spar extensions and wing root are clamped as if they were connected to the fuselage.

5.3 Discussion of Results

In this section, a compilation of the results obtained for three different conditions is presented, as well as a final comparison and summary.

5.3.1 Wing Bending Test

To validate the numerical design framework, experimental data was used from a static wing bending test provided by Tekever. Weights were added in the lower skin with the wing upside down and the tip displacement measured. Analysing with TACS, the maximum deflection obtained was about $0.17\,\mathrm{m}$ across the tip. The undeformed and deformed shapes can be observed in Fig. 5.12.

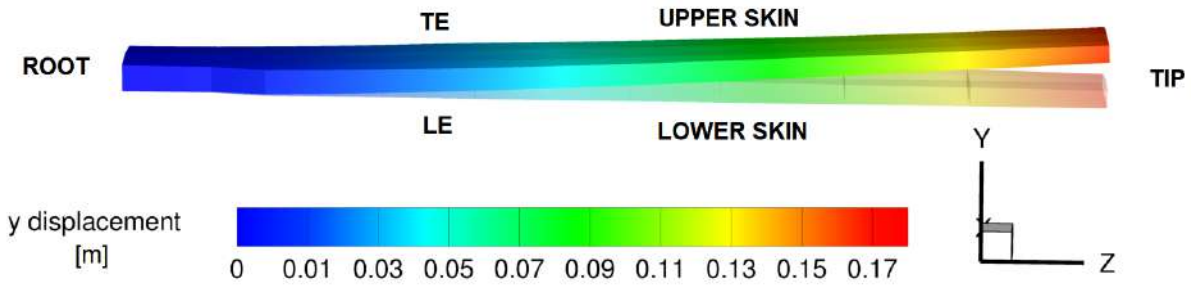

Figure 5.12: Wingbox's displacement in the vertical direction under the fixed loads condition

According to the ground test values, the measured displacements, at the tip, for the leading edge and

trailing edge were $0.12\,\mathrm{m}$ and $0.17\,\mathrm{m}$, respectively. Firstly, the order of magnitude of the computational results is similar which is a good indicator that the model is behaving as expected. Secondly, the fact that there is no significant difference between the leading and trailing edge from the computational results is due to a portion of the rear spar, close to the tip, not existing in reality, so the trailing edge has lower stiffness and a higher displacement in the bending test. Finally, the computational results reproduce overall a higher displacement and this is the expected behaviour since, with the geometry approximations explained in Sec. 5.2.2, some wing elements were not added, making the wing less stiff and exhibit a larger deformation.

After this, a more detailed geometry (Fig. 5.2) was used to test the analysis framework capabilities. Unsurprisingly, since this model has more sections, such as other skin panels, the stiffness increases in comparison to the simplified wingbox, reflecting the reduced tip maximum displacement of $0.054\,\mathrm{m}$ and $0.053\,\mathrm{m}$ at the trailing and leading edge, respectively, as represented in Fig. 5.13.

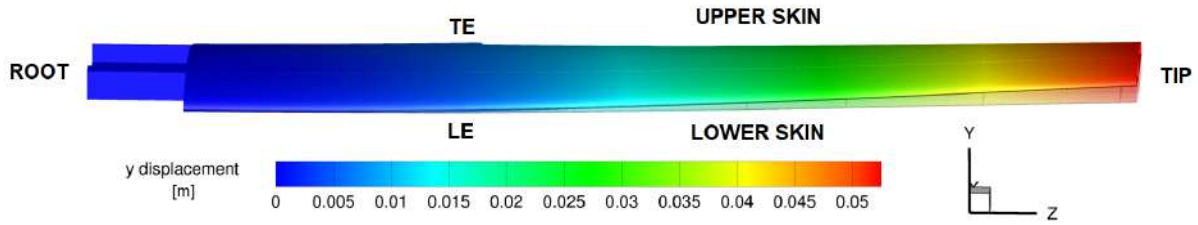

Figure 5.13: Detailed wingbox's displacement in y under the fixed loads condition

These values are about 50% of the measured ones but it is believed that this difference comes from the material properties since it was the information lacking the most. Nonetheless, the values do not seem too disproportional to the actual behaviour of the wing under loading and it can then be concluded that the framework produced acceptable results.

5.3.2 Cruise and 4.0g Manoeuvre

For these conditions, the most important results to gather are the failure index, as well as displacement, to make sure it is acceptable, given cruise is the condition in which the UAV is working at the most time and 4.0g is the maximum allowed load in the AR5 flight envelope. The failure index results are shown in Fig. 5.14 and 5.15, respectively for both conditions and the normalized displacement are plotted across the wingbox's front spar and presented in Fig. 5.16.

For failure index, the criteria used was the Tsai-Wu (Sec. 3.4). The results obtained are satisfactory and well bellow the unity for both cases, being the maximum observed in the 4.0g load case, with values of 0.47 and 0.31 for the simple and detailed mesh, respectively. Consequently, this gives the structure a safety factor of 2.1 and 3.2. However, it must be noted that, the value itself of the maximum failure index is not expected to correspond to the reality since those points are singularities. The sharp transition between the first and second portions of the spars in the simple mesh and the almost $90°$ angle between the skin and spar in the detailed mesh make the stress increasingly high, no matter the

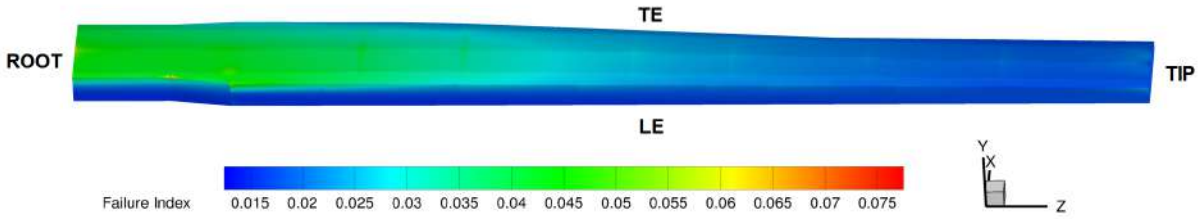

(a) Simpler wingbox's failure index at the leading edge and upper skin, under the cruise condition

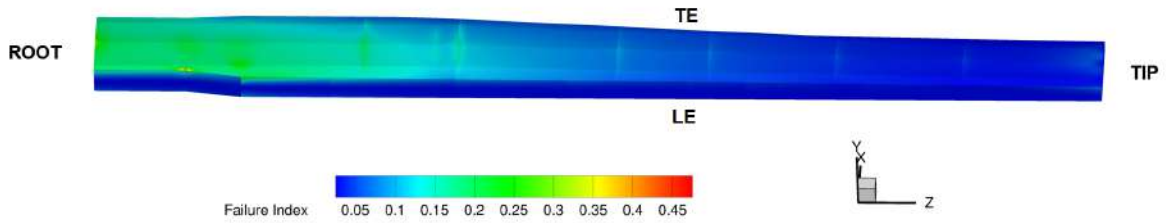

(b) Simpler wingbox's failure index at the leading edge and upper skin, under the 4.0g condition

Figure 5.14: Failure index distribution for the simpler wingbox at cruise and 4g condition

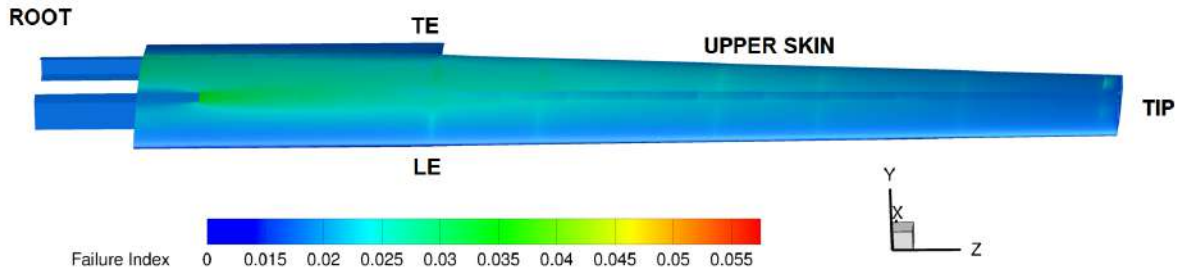

(a) Detailed wingbox's failure index at the leading edge and upper skin, under the cruise condition

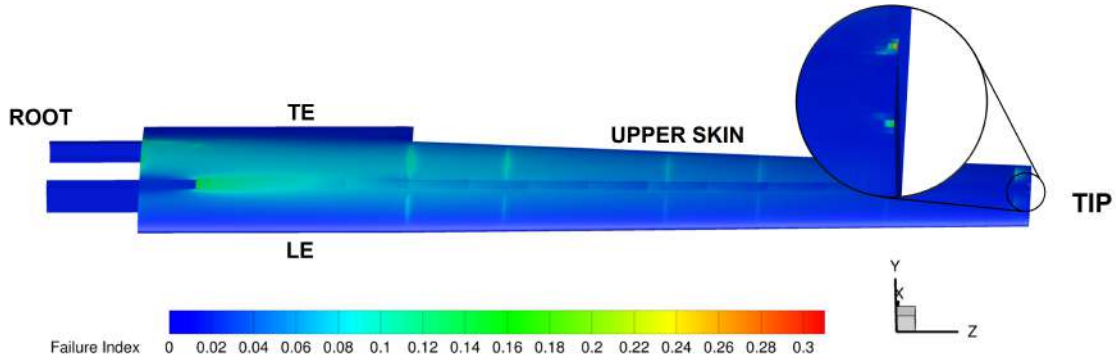

(b) Detailed wingbox's failure index at the leading edge and upper skin, under the 4.0g condition

Figure 5.15: Failure index distribution for the detailed wingbox at cruise and 4g condition

level of refinement. The value is not too high, comparatively with their neighbourhood points, as it can be seen by the colour distribution in Fig. 5.14 b) and 5.15 b), and those values are correct since the mesh converged in non singular points. Nonetheless, it could be said that these safety factors are slightly high since the Tekever AR5 is unmanned and mainly operated at sea. Therefore, in case of a problem

or failure, the most likely damages are all material. This means that the baseline design might be too conservative, leaving some room for improvement. Finally, as expected, the higher values are found near the root and where large material thickness differences occur. These values are justified due to large bending moments at the root deriving from the aerodynamic forces and due to the stress values increasing at the material transition, respectively. The aerodynamic forces are also at their highest in the 4.0g manoeuvre, giving higher values of failure index in this condition.

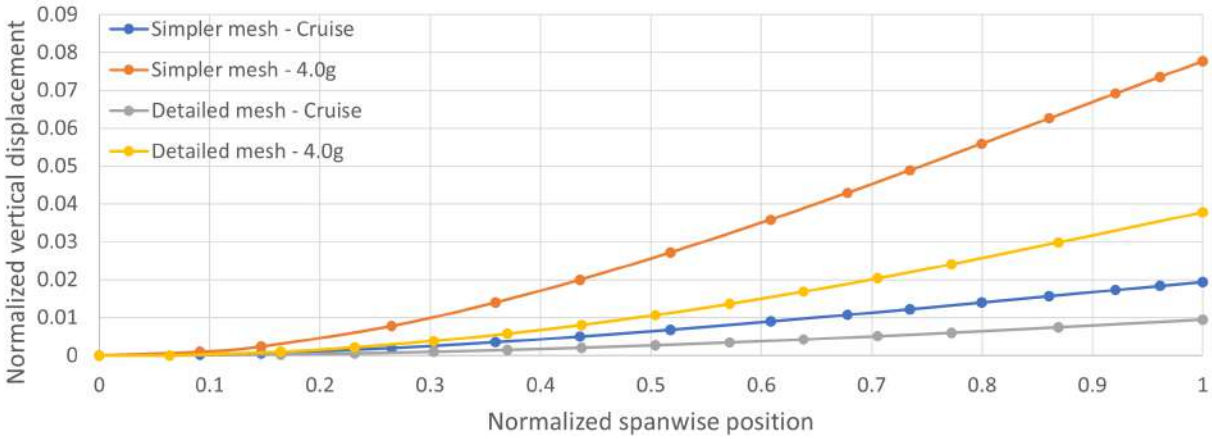

Figure 5.16: Normalized displacement at the front spar

Regarding the normalized vertical displacements that were plotted across the wingbox's front spar in Fig. 5.16 , the maximum deflection obtained is for the 4.0g load condition with the simpler mesh, at the tip, and corresponds to about 8% of half span $(0.264\,\mathrm{m})$. This value indicates that the deflection is not too large relative to the wing size and it is acceptable. Once again, the higher stiffness from the detailed mesh is easily seen, with a maximum deflection of about 4% of the half span. Another interesting aspect that can be seen is the linearity of the analysis, since with an applied force four times higher (4.0g over cruise), the displacements are likewise four times higher.

5.3.3 Summary and Discussion of Results

Given the results in the previous section, it is important to summarize and compare them among the presented load conditions. A compilation of such results is given in Tab. 5.8.

Table 5.8: Comparison of key results across the different load conditions and meshes

Load Case	Model	Maximum deflection [m]	Maximum failure index	Tip rotation ($\Delta\gamma$)	RAM	CPU time
Wing Bending Test	Simple	0.176	0.24	$-1.4°$	+2%	-85%
	Detailed	0.054	0.09	$-0.17°$	+57%	-63%
Cruise	Simple	0.068	0.08	$-0.12°$	+2%	0%
	Detailed	0.029	0.06	$-0.22°$	+55%	+9%
4.0g	Simple	0.266	0.47	$-0.47°$	REF.	REF.
	Detailed	0.116	0.31	$-0.87°$	+57%	+9%

The maximum deflection results are located at the trailing edge of the wing tip. These are within a normal range of values and are not high, since the maximum is around 8% the half-span. Considering

that the wing is not expected to deform too much, non-linear analyses would unnecessarily increase the computational cost so these analyses and the following optimisations are only linear.

As previously discussed, the maximum failure indexes give acceptable safety factors that indicate some room for improvement in this geometry.

It is now relevant to discuss the tip rotation values between the non-deformed and the deformed configuration ($\Delta\gamma$). The negative value indicates a pitch down rotation, meaning that all situations lead to a counter-acting movement to a possible divergent behaviour of the wing, which is desirable. Quantitatively, since there is no spar near the tip of the wing in the actual Tekever AR5, these values might change slightly from the ones of the simpler mesh. However, it is possible to see that this advantageous behaviour is increased with increasing load (comparing cruise to the 4.0g load condition). The outlier here is the wing bending test, that shows a much larger rotation than the other cases for the simpler mesh and the lowest rotation for the detailed mesh. For the simpler mesh, the reasoning for this behaviour is that, since the loads used are constant along the chord, which is not the case of the lift distribution, higher loads are found near the trailing edge in this test, making a higher pitch-down deflection on the wing (this is because the loads are applied in the lower skin as explained in Sec. 5.2.3). The low value in the detailed mesh is probably due to the higher stiffness of this more complete model.

Finally, in terms of computational cost, using the 4.0g analysis with the simple mesh as reference (which corresponds to the load case and mesh chosen in the mesh refinement study), it is possible to see that the least computational expensive ones are with the fixed loads. This is due to how the loads are applied since, in that case, the load is applied directly in the desired DV groups rather then reading it through a file. This last process takes more time since it is necessary to create connections between the point forces obtained with the aerodynamic analysis and the mesh nodes, through rigid links. Comparing directly the 4.0g analyses of both meshes, it is observable that the detailed mesh takes 9% more time and needs 57% more RAM than the simpler mesh. This increase in cost makes it more efficient for the optimisation to use the simpler mesh considering that those 9% more seconds scale with the number of iterations in an optimisation.

Chapter 6

Tekever AR5 Wing Structural Optimisation

In this chapter, the optimisation problem formulation is given, detailing the objective, the design variables and the given constraints to achieve the optimal wing structure. Following that, several optimal solutions are presented, with increasing level of restrictions and details. Finally, a quantitative comparison is given between the optimal solutions found and the baseline structure.

6.1 Problem Formulation

To formulate the problem to optimise the wingbox structure, it is necessary to define the parameters discussed in Sec. 3.8. Given that the highest loads in the Tekever AR5 correspond to the 4.0g manoeuvre, all the optimisation problems are under this load condition.

Objective

Tekever's goal is to minimize the structural mass and increase the efficiency of the AR5, meaning that the objective function to this problem is the total wingbox mass. This includes the ribs, spars and upper and lower skins.

$$m_{\text{total}} = m_{\text{ribs}} + m_{\text{spars}} + m_{\text{upper skin}} + m_{\text{lower skin}} \tag{6.1}$$

Design Variables

To control this mass, the variables allowed are some of the parameters that describe the wingbox design variable (DV) groups. In this case, the ones chosen are the thickness (t_i) of the ith DV group and the orientation (θ_{ij}) of the jth CFRP ply from the ith DV group. This last design variable does not have a direct impact on the mass but allows the wing to change its stiffness to possibly lower the thickness of the CFRP and still withstand the aerodynamic loads. It is important to note that, due to physical

constraints, each wingbox section thickness is allowed to change within a set of bounds (maximum and minimum thicknesses).

The boundaries for each DV group are defined as: minimum of $1\,\mathrm{mm}$ for both skins and spar areas with foam core and $0.25\,\mathrm{mm}$ for the spars sections that are only constituted by CFRP; to give more freedom to the optimiser to possibly reinforce certain areas of the wingbox, a maximum of $100\,\mathrm{mm}$ was set. The ply angles have a lower bound of -90° and a upper bound of 90°.

Constraints

Finally, some inequality constraints are set: failure constraint, using the KS function, to make sure the failure index given in Sec. 3.4 by the Tsai-Wu criterion is limited to a maximum of 1 and ensure that the wing can withstand the loads; displacement constraint, also using the KS function, to make sure the vertical displacement stays below 12% of the half wing span; adjacency constraints, to keep a thickness difference ($|t_i - t_k|$) between a certain ith DV group and its adjacent groups (kth DV groups) under a Δ_{max}; decreasing thickness constraint, from the root to the tip ($t_j - t_{j+1} \geq 0$), where t_j is the thickness of th jth DV group and t_{j+1} of the following (the higher the index, the closer to the root the DV group is); ply angle continuity ($\theta_{1_i} = \theta_{1_k}$ and $\theta_{2_i} = \theta_{2_k}$, where θ_{1_i} corresponds to the angle of the first ply of the $i$the DV group and k is its adjacent) to ensure the wing can be manufactured by normal methods; orthogonality between plies ($|\theta_1 - \theta_2| = 90^\circ$) to allow the use of carbon fibre cloths with weaving pattern; and finally a maximum torsion for the wing tip ($\gamma \leq \gamma_{\text{max}}$).

With this in mind, the fully constrained optimisation problem for this wingbox structure can be formulated as

$$
\begin{aligned}
\text{minimize} \quad & m_{\text{total}} \\
\text{w.r.t.} \quad & t_i \\
& \theta_{ij}\,, \\
\text{subject to} \quad & \text{KS(failure)} \leq 1 \\
& \text{KS(displacement)} \leq 0.12 \\
& |t_i - t_k| \leq \Delta_{max} \\
& t_j - t_{j+1} \geq 0 \\
& \theta_{1_i} = \theta_{1_k} \\
& \theta_{2_i} = \theta_{1_k} \\
& |\theta_1 - \theta_2| = 90^\circ \\
& \gamma \leq \gamma_{\text{max}}\,.
\end{aligned}
\tag{6.2}
$$

To give a more realistic solution, considering that it would not be feasible to have a very large panel connected to a very thin one, Δ_{max} is set to $5\,\mathrm{mm}$.

Optimiser Parameters

To run the optimisation, the choice of the algorithm, convergence and termination criteria are necessary.

The optimisation algorithm used was the sequential least squares programming algorithm (SLSQP), briefly presented in Sec. 3.8. For convergence, since numerically the computer can not achieve a derivative exactly zero to assess if the minimum of a function was attained, it is assumed to be at such location when the difference between solutions is smaller than 10^{-6}. To ensure that the optimisation process stops if no minimum is found and it does not run indefinitely, a maximum of 500 iterations are allowed.

6.2 Baseline Optimisation - Case 1

In this and the following sections, the optimisation results are presented and compared against the baseline model. To compare between solutions and have a better understanding of the necessity of some constraints, the problem went from a baseline and simpler formulation, evolving in the number of constraints to the complete problem in Eq. (6.2).

Before that, it is important to acknowledge that the solution found is actually a minimum of the objective function. This can be seen by checking what stopping criteria was used actually used to stop the optimisation process. In this case, the optimisation was successful since the program stopped by reaching the convergence accuracy of 10^{-6}.

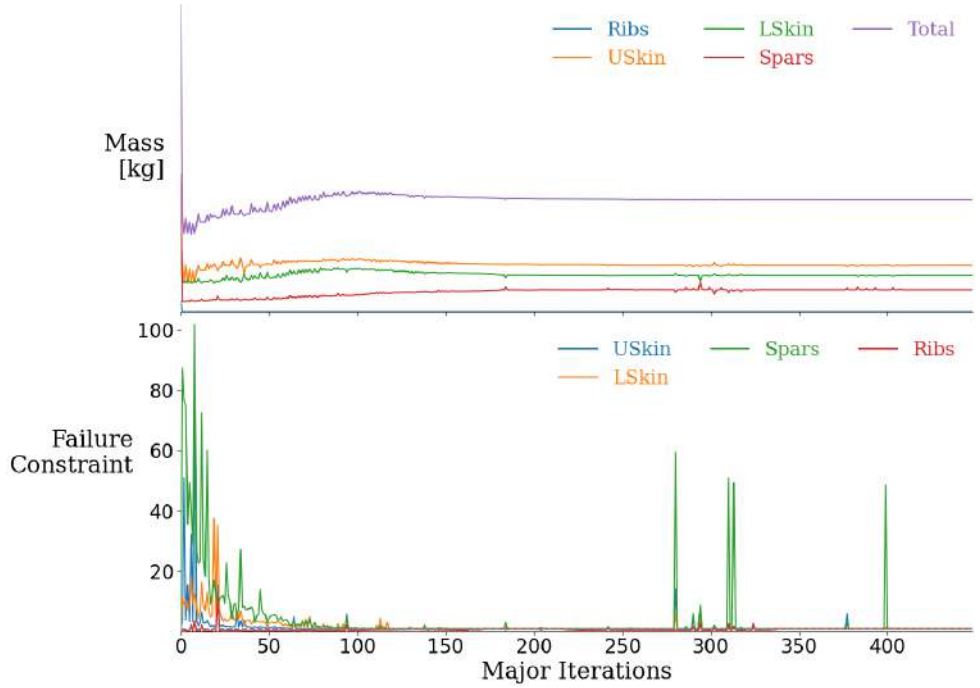

Figure 6.1: Objective function and failure constraint optimisation history

Fig. 6.1 shows the history of the objective and constraints in which the objective function exhibits a converging behaviour, reinforcing the fact that the optimisation found an optimal solution. It is important

to point that, since the SLSQP output file does not provide these history values over the iterations, the only solution found to present these results was plotting over the increasing number of function evaluations. In the optimisation process, the sensitivity function is first called to search for a feasible descent direction, then more than one function evaluation can be performed to get a better solution for the following iteration. This is the reasoning why the maximum iterations is set to 500 but the graph shows a higher number of function evaluations.

The mass reduction was very noticeable, decreasing 55.6% relative to the baseline. This is a very large difference, mainly due to the low number of constraints that this case 1 has, which results in an optimal solution with much thinner areas as Fig. 6.2 shows.

Another interesting aspect to note in Fig. 6.1 is that the failure constraint has visible upper spikes that match with the mass lowering spikes, which happens when the optimiser tries to lower the mass, violating the failure constraint.

Fig. 6.2 compares the initial case with the found optimised solution having the different wingbox components' thicknesses. Across the entire wingbox, the thickness is lower in the optimal solution and, as expected, the highest and lowest values are located near the root and tip of the wing, respectively. This is due to the lift distribution being close to elliptical, so higher forces are located near the root and lower forces at the wing tip.

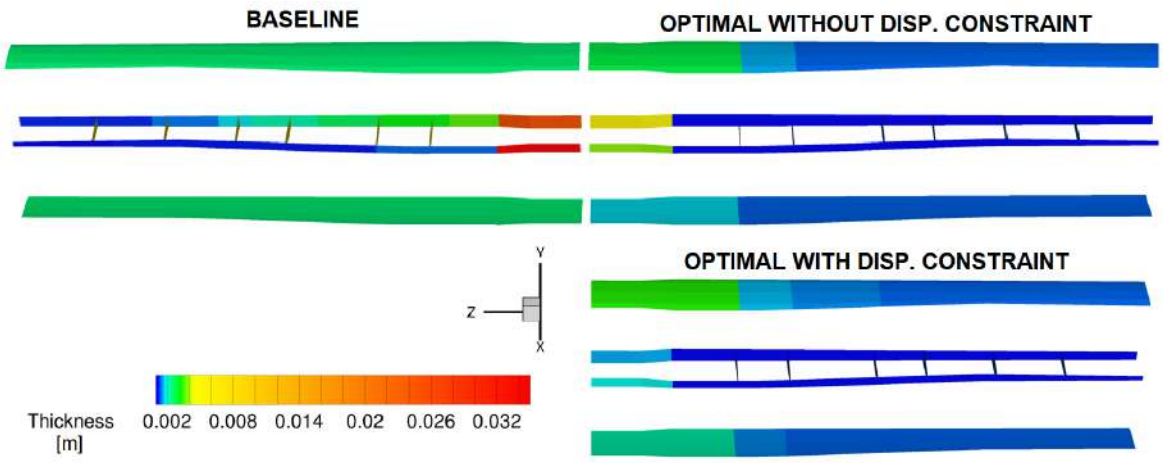

Figure 6.2: Comparison between initial component thicknesses (left) and optimised solution found (right)

Regarding the failure index shown in Fig. 6.3, the optimised wingbox has more regions with a higher failure index due to the overall decrease in the thickness and the wing being less oversized.

With the thinning of the wingbox components and without buckling constraints present in this optimisation, it is expected that the wing displacement increases. In fact, the optimised wingbox, for this 4g load condition, presents a relative maximum vertical displacement of 0.18 ($+126\%$ than the baseline) and its deformation is present in Fig. 6.4.

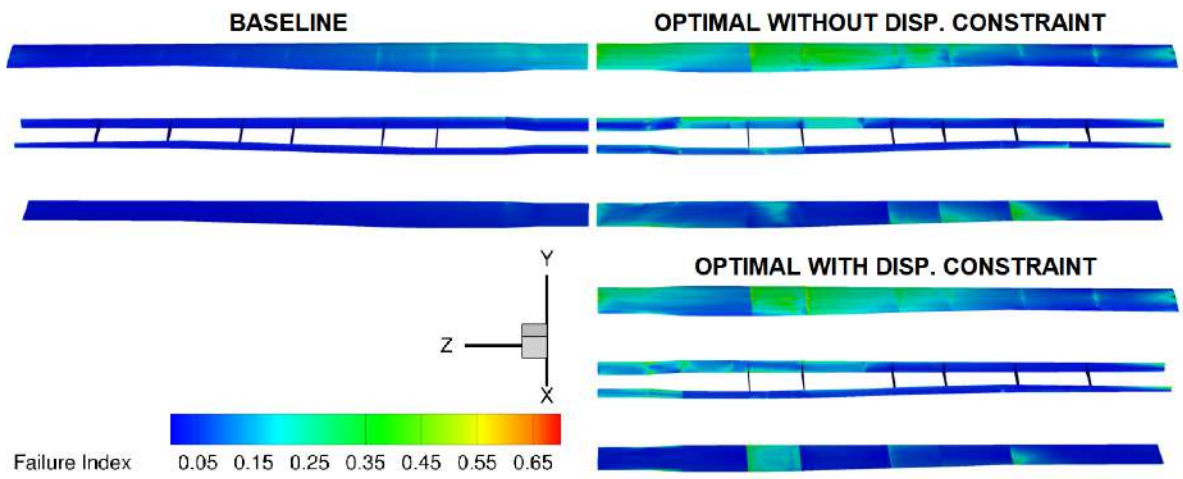

Figure 6.3: Comparison between failure index for the initial wingbox (left) and the optimised solutions found (right)

6.3 Baseline Optimisation with Displacement Constraint - Case 2

To prevent such a large displacement, another KS function, aggregating all displacements from a specific wingbox components is used, in order to more easily control the maximum displacement of that specific component. Similarly to the failure function, this displacement constraint requires a KS function since the maximum function can not be differentiated. In the present case, the tip of the wing is the most problematic location so the constraining KS function uses the displacements in that region.

Having performed the optimisation adding the inequality constraint, KS(disp) < 0.12 of half span, a similar plot to Fig. 6.1 was obtained, confirming convergence of the solution and constraints. By plotting the front spar normalized displacements against the spanwise position (Fig. 6.4) it is possible to assess that the constraint was successful at lowering the maximum allowed displacement to the acceptable 12% of half of the wing span.

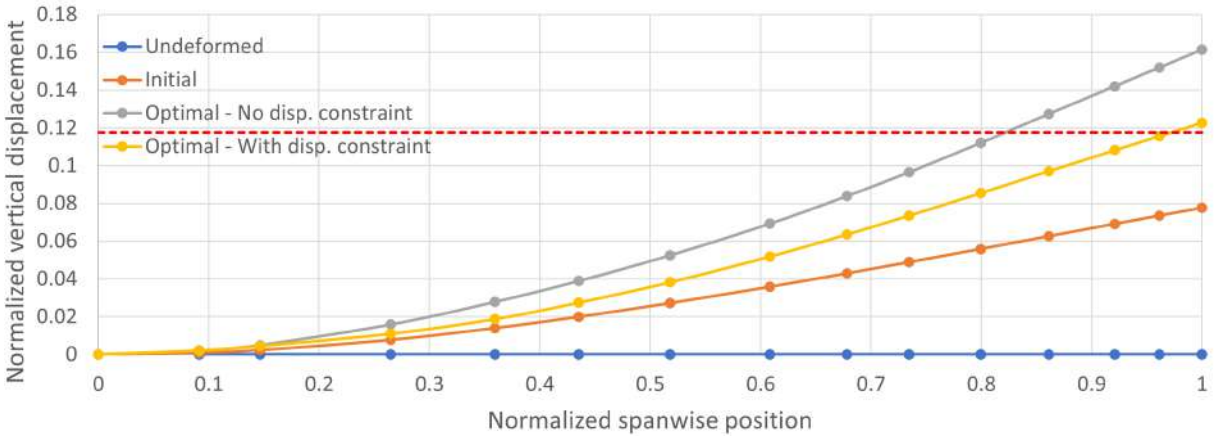

Figure 6.4: Front spar y deflection comparison between undeformed, initial solution and optimal solution, with and without maximum displacement constraint, under 4g

To ensure this new constraint was respected, it is interesting to see that, comparing the thickness of the components from the previous optimal solution and the newer one (Fig. 6.2), the thickness increased, particularly near the root for both the upper and lower skins. In contrast, there is a reduction in thickness near the root for both spars. This indicates that the root skin panels of the skin are more effective at increasing the wing bending stiffness and reducing the maximum displacement and it is possible to mitigate the mass gain by thinning the spars. Although making the spars thinner supposedly decreases their stiffness, the gain from the skin panels is greater and the overall mass is reduced this way.

Relatively to the previous case 1, this optimal solution had slightly more mass, resulting in a difference relative to the baseline of -52.8%. This happens due to the increased thickness in some sections to respect the constraint.

From Fig. 6.3 and the information in Tab. 6.7, it is possible to conclude that the failure inequality constraint remained active, implying that the optimised structure under the 4g condition corresponds to the thinnest possible solution that still withstands the critical aerodynamic loads.

Using the optimal solution obtained from the baseline optimisation as the starting point in a new optimisation with displacement constraint (Case 2 - new baseline) leads to a new solution, which corresponds to a different local minimum.

A full description of the final values of the design variables for each wingbox DV group is present in Tab. 6.1 for the three optimisation cases (Case 1/Case 2/Case 2 - new baseline). The ply orientation is according to Fig. 5.5

Table 6.1: Design variables' values of the optimal solutions

Upper Skin	1 (Root)	2	3	4	5	6	7 (Tip)
t [mm]	2.8/3.3/3.0	1.4/1.4/1.3	1.0/1.2/1.0	1.0/1.0/1.0	1.0/1.0/1.0	1.0/1.0/1.0	1.0/1.0/1.0
θ_1 [°]	-1.1/-7.8/-3.6	-1.4/-5.2/-2.6	-4.8/-2.4/-2.4	-20.1/-1.9/-3.6	3.0/-2.7/-1.9	-1.7/-1.7/-0.1	9.5/7.9/6.0
θ_2 [°]	90.0/19.6/90.0	90.0/27.8/90.0	32.8/90.0/-2.5	24.3/90.0/0.1	87.8/90.0/-0.6	88.1/90.0/90.0	87.9/90.0/90.0

Lower Skin	1 (Root)	2	3	4	5	6	7 (Tip)
t [mm]	1.7/2.2/2.1	1.0/1.2/1.0	1.0/1.0/1.0	1.0/1.0/1.0	1.0/1.0/1.0	1.0/1.0/1.0	1.0/1.0/1.0
θ_1 [°]	-1.8/-5.7/-5.3	-14.4/3.2/-16.3	-4.1/-8.5/10.3	7.9/1.3/3.5	16.6/0.7/6.3	43.2/30.5/-21.4	52.5/58.4/62.8
θ_2 [°]	56.8/14.0/18.0	22.0/90.0/19.6	20.8/13.8/-4.6	84.9/89.7/-0.3	89.9/77.4/-4.3	90.0/90.0/19.8	52.5/58.3/63.2

Ribs	1 (Closer to root)	2	3	4	5	6 (Closer to tip)
t [mm]	1.0/1.0/1.0	1.0/1.0/1.0	1.0/1.0/1.0	1.0/1.0/1.0	1.0/1.0/1.0	1.0/1.0/1.0
θ_1 [°]	-17.3/-55.6/-77.0	-20.2/3.4/13.8	-20.7/6.6/7.2	-0.5/0.0/-0.2	-5.5/-4.2/-26.6	4.4/-1.6/-24.0
θ_2 [°]	36.4/75.5/45.9	16.3/90.0/10.1	80.1/89.4/82.5	89.8/90.0/90.0	88.4/88.9/86.1	90.0/89.4/82.9

Front Spar	1 (Root)	2	3	4	5	6	7	8 (Tip)
t [mm]	5.1/1.4/3.0	0.4/0.3/0.3	0.3/0.3/0.3	0.3/0.3/0.3	0.3/0.3/0.3	0.3/0.3/0.3	0.3/0.3/0.3	0.3/0.3/0.3
θ_1 [°]	20.8/-11.1/1.7	20.7/-61.1/-30.6	10.5/-23.8/-70.4	-40.1/-3.1/-68.9	9.8/-1.8/0.4	-0.5/-2.5/-37.2	-0.3/-6.3/-62.3	0.8/1.4/1.7
θ_2 [°]	90.0/86.5/90.0	90.0/5.3/27.3	90.0/10.8/5.7	90.0/90.0/7.9	61.3/68.4/73.1	77.1/80.9/78.4	74.8/79.8/72.6	83.0/81.1/78.4

Rear Spar	1 (Root)	2	3	4 (Tip)
t [mm]	3.9/1.9/3.3	0.3/0.3/0.3	0.3/0.3/0.3	0.3/0.3/0.4
θ_1 [°]	-26.7/-28.6/-11.3	5.8/-26.9/-61.0	-9.6/-72.8/-69.9	-19.1/-18.2/-11.7
θ_2 [°]	72.9/35.6/45.0	90.0/40.7/40.9	43.3/58.4/75.5	89.3/88.2/86.3

It can be concluded that, across the span, the thickness decreases except for the rear spar although it is not too much (about $0.1\,\mathrm{mm}$ more than the previous panel). Furthermore, although the local minima produced a similar displacement response, it has a very distinct composition in terms of ply orientation, allowing the wingbox to satisfy the constraints with a higher safety factor (lower failure index).

Regarding the ribs, these are the parts that suffer the most thickness changes since their baseline value is $6\,\mathrm{mm}$ and, across all optimisations, the value is reduced to the lower bound of $1\,\mathrm{mm}$. This might indicate that the baseline value is greatly oversized. Although it might be true, it cannot be concluded since no buckling constraints were added and the wingbox ribs main function is to increase the buckling strength.

One final note about the plies orientation and a main concern and physical constraint: if this wing was to be manufactured, since the angles of the different DV groups have large disparities between them, it would not be possible to manufacture it with unidirectional fibre cloths. Considering that, it would lead to non continuity of the fibres along the span which is extremely non desirable, as they create weak points. This means that, alternative methods of manufacturing would be needed or the addition of constraints to make sure the ply angles would be the same across the groups from the different wingbox components.

6.4 Ply Angle Continuity Constraint - Case 3

To tackle this problem of continuity between the ply angles of the different DV groups each component (front and rear spars and upper and lower skins), adjacency constraints similar to the previously mention for the thickness, were applied. However, for the continuity, the Δ_{max} was set to 10^-3 so that the angles would be approximately the same. This was done since it is much easier to model the problem with inequality constraints with close upper and lower bounds (a very low Δ) than using equality constraints. A new optimisation problem was then created with this and all previous constraints.

The results produced using this new approach gave a new optimal solution and as seen in Fig. 6.5, the constraint was satisfied by each wing component, where each corresponding θ is similar across it. In Tab. 6.2, the values of the ply angles are summarised. Note that the ribs' results are not shown, since each rib is considered a DV group, making this constraint not relevant for them. The remaining results are presented in Tab. D.1 and D.2 in Appendix D.

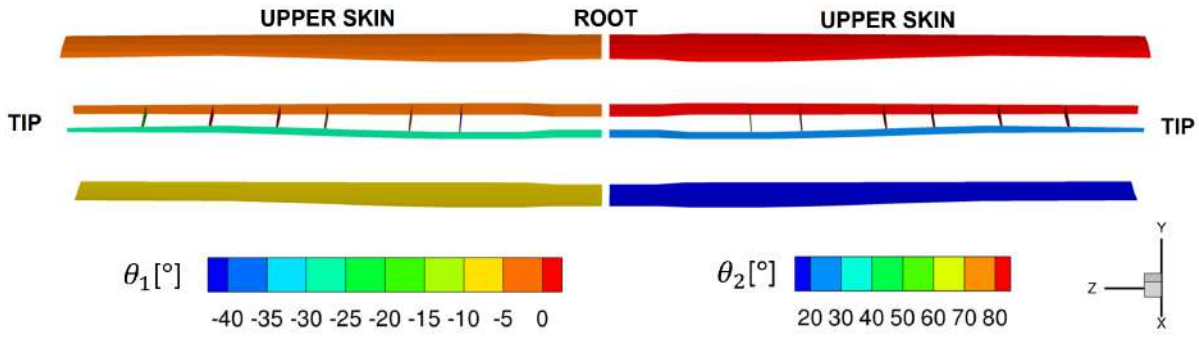

Figure 6.5: Visual representation of ply angles θ_1 and θ_2 for each component (case 3)

However, it must be noted that unidirectional fibre cloths would be required to manufacture this wingbox. Since the most commonly available and cheaper material are weave patterns, a new constraint is required to have this relation between fibres taken into consideration.

Table 6.2: Ply angle results for each component (case 3)

	Upper Skin	Lower Skin	Front Spar	Rear Spar
θ_1	$-1.9°$	$-6.2°$	$-1.0°$	$-28.1°$
θ_2	$90.0°$	$13.3°$	$90.0°$	$22.4°$

6.5 Orthogonal Plies Constraint - Case 4

As mentioned in Sec. 4.3.2, for Tekever to be able to use woven CFRP fabric with a weave pattern, the orthogonal constraint is necessary. With this in mind, this constraint was added to the previously mentioned ones and more results obtained. Once again, Tab. 6.3 and 6.4 summarises the newly obtained optimal ply angles while Fig. 6.6 represents the thickness along the span. The remaining results are presented in Tab. D.3 in Appendix D.

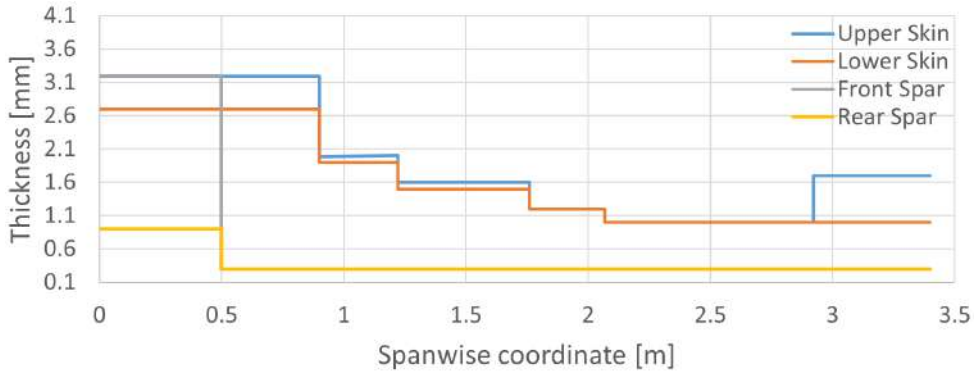

Figure 6.6: Thickness distribution for each component with added orthogonal plies constraint (case 4)

Table 6.3: Ply angle results for each component (case 4)

	Upper Skin	Lower Skin	Front Spar	Rear Spar
θ_1	$88.8°$	$90.0°$	$87.5°$	$46.8°$
θ_2	$-1.2°$	$0.1°$	$-2.5°$	$-43.1°$

Table 6.4: Ply angle and thickness results for each rib (case 4)

Ribs	1 (Root)	2	3	4	5	6
θ_1	$90.0°$	$89.1°$	$89.9°$	$90.0°$	$90.0°$	$87.6°$
θ_2	$0.0°$	$-0.9°$	$-0.1°$	$0.1°$	$0.0°$	$-2.4°$
Thickness [mm]	1.0	1.0	1.0	1.0	1.0	1.0

Tab. 6.3 and 6.4 confirms that the orthogonality between the ply angles is now present for all wingbox components.

The problem appearing now in this optimal solution is the one mentioned in Sec. 4.3.2. In the thickness distribution (Fig. 6.6), it is easily seen that the behaviour visually described in Fig. 4.7 is present at the upper skin. The thickness decreases from $3.1\,\mathrm{mm}$ at the root to about $1.0\,\mathrm{mm}$ at z equal to $2.8\,\mathrm{m}$ when it starts increasing again, up to around $1.7\,\mathrm{mm}$, not allowing the continuity of the fibres.

6.6 Decreasing Thickness Constraint - Case 5

A final manufacturing constraint was then added, to make sure the spar and skin panels have a monotonic thickness, decreasing from the root to the tip. The thickness distribution results obtained with the addition of this constraint are presented in Fig. 6.7. Once gain, the ribs' thickness results are not presented here for the same reason previously mentioned in Sec. 6.4. Nonetheless, all the results are presented in Tab. D.1 and D.2 in Appendix D and Tab. 6.5 in Sec. 6.7.

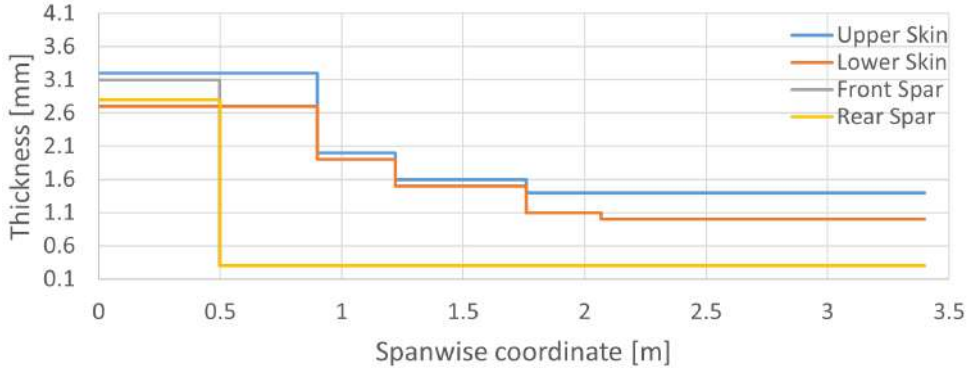

Figure 6.7: Thickness distribution for each component with added decreasing thickness constraint

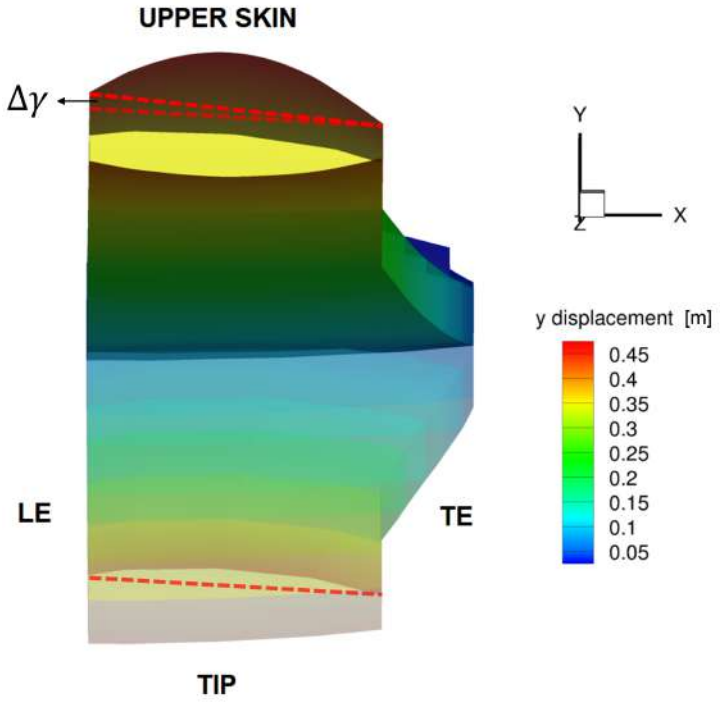

Figure 6.8: Tip rotation representation

It is acknowledged that the thickness behaves as desired while keeping active the previously added constraints, making this solution possible to be manufactured. In contrast, the tip torsion (γ - represented in Fig. 4.8) that this optimal solution presented, when under the 4g load, was $5.9°$ ($\Delta\gamma$ of $2.4°$ relative to the undeformed wingbox - Fig. 6.8). Not only this $\Delta\alpha$ is now positive (tip up) but also the absolute value

of α increased. This indicates that, the divergence behaviour is becoming a threat for the wing structure since the optimal solution is allowing a wash-in deformation under loading.

6.7 Tip Torsion Constraint - Case 6

To limit this, the final added constraint to the problem was an upper limit for the tip torsion. A new optimisation problem was set up to reduce about 20% of the tip torsion, compared to the previous solution (case 5). This final and most constrained problem is formulated in Eq. (6.2) where γ_{max} is $4.4°$ (corresponding to -20% of the tip torsin in the case 5 optimal solution). Considering that there were some difficulties trying to converge to an optimal solution, the stopping criteria was relaxed and the convergence accuracy increased to 10^{-4}.

The final optimal thickness distribution is given in Fig. 6.9 and ply angles in Tab. 6.5. In this table, the ply angles of the previous optimisation, with the decreasing thickness constraint, are added for comparison. For the ribs, both the thickness and ply angles are presented in Tab. 6.6. The remaining results are presented in Tab. D.6 in Appendix D.

Table 6.5: Ply angle results for each component and case (case 5/case 6)

	Upper Skin	Lower Skin	Front Spar	Rear Spar
θ_1	$88.8°/87.5°$	$90.0°/90.0°$	$87.4°/87.4°$	$66.4°/78.8°$
θ_2	$-1.2°/-2.5°$	$0.0°/0.1°$	$-2.6°/-2.6°$	$-23.6°/-11.1°$

Table 6.6: Ply angle and thickness results for each rib (case 6)

Ribs	1 (Root)	2	3	4	5	6
θ_1	$90.0°$	$89.5°$	$90.0°$	$90.0°$	$89.5°$	$90.0°$
θ_2	$0.0°$	$-0.5°$	$0.0°$	$0.0°$	$-0.5°$	$0.1°$
Thickness [mm]	1.0	1.0	1.0	1.0	1.0	1.0

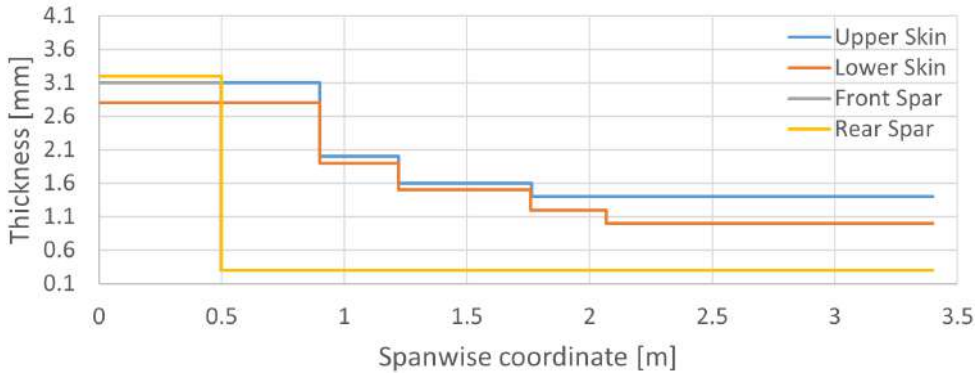

Figure 6.9: Thickness distribution for each component with added tip torsion constraint (case 6)

As desired, the tip torsion constraint is active for the optimal solution, giving an γ of $4.4°$ ($\Delta\gamma$ of about $0.7°$) while under 4g. It effectively improved the wash-in behaviour at the tip by reducing it to less than 1%.

This effective reduction in torsion can be seen with the change in ply angles from case 5 (without the torsion constraint) to case 6 (with the addition of this constraint). By analysing Tab. 6.5 and Tab. D.4 and D.6 in Appendix D, the only components with changes are the upper skin and rear spar. It is important to understand the change in the deformation behaviour of the wing due to these differences. Starting by the most noticeable, the rear spar, from case 5 to case 6, the fibres orientation change about $12°$ due to the maximum failure index being located in this component. Fig. 6.10 represents this change, where the fibres go from the position in red to green. This makes the θ_1 and θ_2 angles more perpendicular and parallel, respectively, to the displacement. In this configuration, the fibres will withstand an higher amount of load in tension and compression. This angle change has larger impact on the thicker section of the rear spar, which is exactly where the maximum failure index occurs.

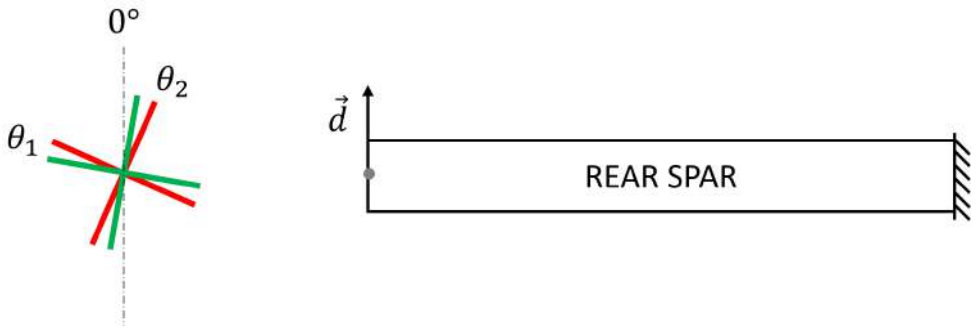

Figure 6.10: Representation of fibre orientation change in rear spar (red - case 6; green - case 7)

The other difference is in the upper skin. Although it might be small, by decreasing the angle, the torsional stiffness of the skin increases (increasing the angle up to $45°$). With this, the overall tip torsion decreases up to the desired value.

Since this is the last and most complete optimisation, the final failure index distribution is presented in Fig. 6.11 with a maximum reaching 0.87. This gives a final safety factor of 1.15 for the optimal solution. It must be noted that, once again, the point of maximum value is a stress singularity. That value only appears at that location and, further away, in regions where the stress values are converged, the highest failure indexes are about 0.4.

Similarly to case 2, since this is the last and most complete optimisation, another fully constrained problem was solved using the optimal solution from case 5 as a new starting point, to try to check for a possible local minimum (case 6 - new baseline). Comparing Tab. 6.5, 6.6 and D.6 with Tab. D.8, D.9 and D.7, respectively, its possible to conclude that the optimal solutions are very similar. In Tab. 6.7 its seen that there are marginally no mass gains with the different starting point indicating that no local minimum was found.

6.8 Summary and Discussion of Results

Having finalized all optimisations in this section, it is useful to summarize and compare some important values namely: the final mass, which was the minimization target; the failure index, to compare the final safety factors; the computational cost (difference in RAM between the baseline analysis and

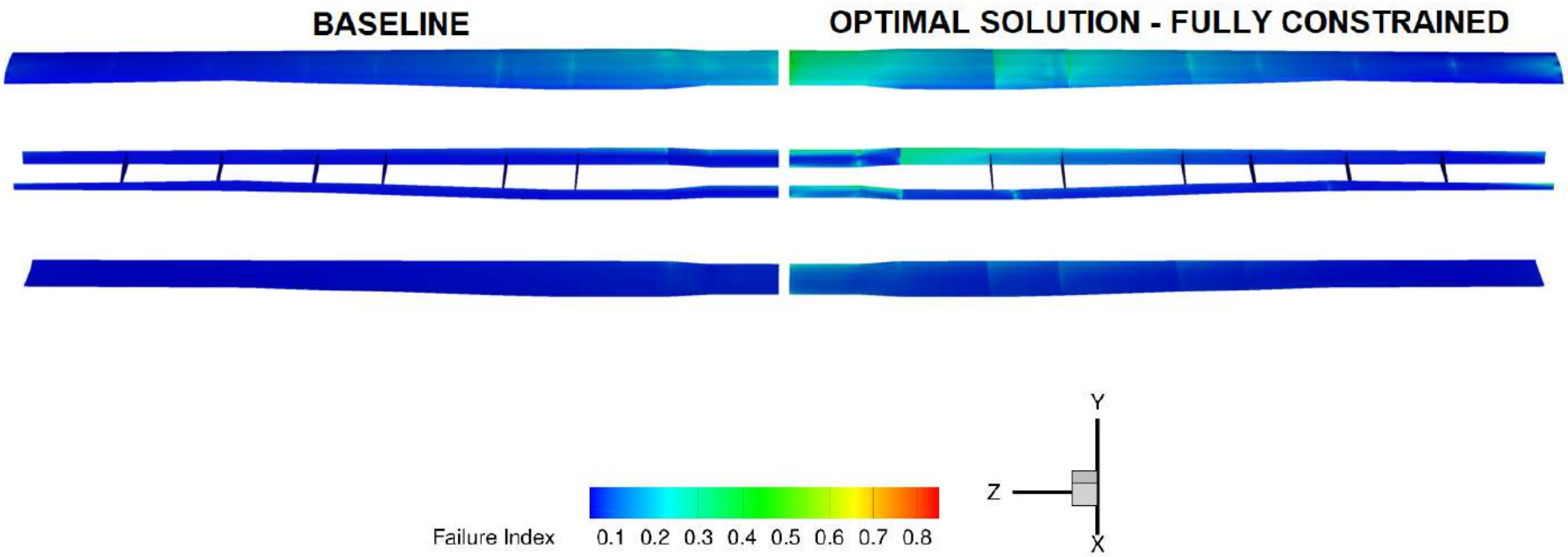

Figure 6.11: Comparison between failure index in the initial wingbox (left) and the final optimised solution found (right)

the corresponding optimisation and the time for the optimisation divided by the time taken to run the baseline analysis); the number of design variables; and the number of constraints.

Table 6.7: Summary of all optimisation results

Case	Mass difference	Failure index	RAM	Non-dimensional time	Number of iterations	Number of DVs	Number of constraints
Baseline Analysis	REF.	0.47	REF.	1.0	-	-	-
1	-55.6%	0.79	0%	37.8	179	96	26
2	-52.8%	0.67	$+2\%$	61.7	340		27
2 (Diff. baseline)	-54.4%	0.58	$+2\%$	53.1	286		27
3	-52.5%	0.64	$+2\%$	18.6	134		71
4	-44.6%	0.61	$+2\%$	11.5	71		103
5	-43.9%	0.93	$+2\%$	12.2	75		125
6	-43.6%	0.87	$+2\%$	44.5	142		126
6 (Diff. baseline)	-43.6%	0.94	$+2\%$	26.1	70		126

It is relevant to compare the results against the Tekever AR5 baseline wing structural analysis quantitatively, to better understand the enhancements these optimisations provide to the AR5 wing. In Tab. 6.7 is a summary of these results.

It is possible to conclude that these optimisations provide a large mass reduction, between 56% and 44% of the original baseline. As expected, with the increasing number of constraints, the reduction is smaller. To respect these additional constraints, thicker sections were necessary to increase the stiffness in certain areas. The third optimisation case revealed to be important since by having the starting point as the optimal solution from the first optimisation case, a better result could be found keeping the displacement constraint. Regarding the possible wingbox failure, a safety factor of 1.5 was used so that all optimisations would have a maximum index of about $\frac{1}{1.5} = 0.67$. Although some optimisations present a failure index below or within this value, others, such as case 5 and 6, do not. This is, again, in a single point of the wingbox and a singularity. Away from it, the average values are lower than 0.67 and respect the 1.5 safety factor.

In terms of computational cost, necessary RAM increased marginally ($+2\%$) when the problem went from 26 to 27 constraints and kept using about that same memory up until 126 constraints. This indicates that the total amount of RAM that is spent in this process comes mostly from the FEM analysis. Regarding the computational time, it behaved differently. While constraints were being added to the optimisation, from case 1 to 3, the time actually decreased. The reason for that is that the solution is being found in a smaller domain, every time a constraint is added. However, in case 5, the behaviour changed and the time increased again. Although the domain also got smaller, the increased number of constraints require more function evaluations and sensitivities. This means that from case 4 onwards, the computational cost increase by the addition of constraints dominates the decrease in time by having a smaller domain. The only exception is case 6 with a different baseline. Considering that the solution is already close to an optimum, the time it takes is smaller than case 6 with the baseline as starting point. It is also possible to see that, the time to finish the optimisation scales with the number of iterations since it performs more analyses. The only outlier is case 6 with the initial and different baseline. Even with a similar number of iterations as case 3 and 4 respectively, it takes more than double the time. This is due

to possible lack of efficiency of the developed tip constraint.

One important factor to note across all the optimisation cases is regarding the ribs. As you can see in Tab. 6.1, D.2, 6.4, D.5 and 6.6, in all optimal solutions, the ribs thickness went from its baseline value of $6\,\mathrm{mm}$ to the minimum ($6\,\mathrm{mm}$). The reason for this behaviour is that no buckling constraints are added throughout this work. As previously stated in Sec. 2.3, ribs are added to mitigate this structural instability on the wing. Therefore, without considering this effect, the ribs would not be necessary and the optimal solution is with these components always with the lowest possible thickness. In reality, this would not be the case.

Chapter 7

Conclusions and Future Work

7.1 Achievements

To conclude this work, a summary of the achievements is provided. Firstly, using a plate test case, the structural optimisation framework was tested and succeeded. This included: the mesh generation, with 4-node quadrangular MITC elements; the TACS analysis using composite materials and optimisation, with the validation of the custom developed constraints; and finally, the optimisation results processing.

Two mesh versions of Tekever AR5 wingbox were created using both 4- and 9-noded quadrangular elements. Analysing their convergence behaviour, it was decided to use the bilinear mesh with $145,408$ elements and $870,948$ degrees of freedom considering that this was the least computational expensive, with a monotonic converging behaviour. A more detailed mesh of the AR5 wing was than created using commercial software.

After the wingbox material characterization, the computationally obtained mass was compared against the measured mass. The difference relative to the real mass was -1.7% and $+1.6\%$, for the simpler and detailed models, respectively.

Experimental results from a wing bending test were compared against computational ones from TACS, under the same load conditions. The tip vertical displacement at the trailing and leading edges of the simpler mesh was about, $0.17\,\mathrm{m}$, which matched the experimental value at the trailing edge of the tip. Due to geometric simplifications, the computational value was very similar at both edges of the tip, in contrast with the real test. Regarding the detailed model, the computational values obtained were about 50% smaller than the measured values. The main reason for these discrepancies are the possible differences in material properties comparatively to the real wing.

Under a 4.0g load condition, the Tekever AR5 wing revealed to have a safety factor between 2.1 and 3.2 indicating a possible oversized structure and room for improvement. Between both meshes, the detailed model took 9% more CPU time and used 57% more RAM than the simpler mesh. Since the time difference scales with the number of optimisation iterations and the memory usage difference is considerable, the simpler mesh was decided as the model to use for the optimisations.

Several optimisation cases were analysed and are provided, in a increasingly constrained manner.

A baseline problem (case 1) was established, considering only adjacency and failure constraints which lead to an optimal solution with a 126% increase in maximum displacement, comparatively to the original wing. Displacement constraints were than added and a new case (case 2) formulated, with two different starting points. The results revealed two optimal solutions with a mass reduction of around 53% and 55%, indicating the presence of a local minima of the mass function. However, due to lack of manufacturing constraints, these solutions could not possibly be manufactured while maintaining structural integrity of the wing. New constraints were then added, namely the continuity of the ply angles, the orthogonality between plies and a monotonically decreasing behaviour for the thickness, from the root to the tip. After all these manufacturing constraints were added (case 5), the optimal solution revealed a 43.9% mass reduction comparatively to the baseline. Despite this desirable reduction, the tip rotation presented a wash-in behaviour, which is not beneficial due to aeroelastic phenomena, such as divergence. Using a maximum allowed tip torsion as constraint, the final and most constrained case (case 6) was created leading to a final mass reduction of 43.6%. Although this geometry had a maximum failure index of 0.94, its location was a model singularity and far from this value, the maximum stress areas had values of about 0.4, which give a safety factor of about 2.5 to the final optimal solution. A final test for local minima was performed which lead to a marginally different solution with the same mass difference relative to the baseline, indicating that, in this case, no local minimum was found.

Finally, this works delivers, as expected, a validated, tested and developed framework for high-fidelity structural analysis and optimisation, while also providing a preliminary optimal solution of the Tekever AR5 wing.

7.2 Future Work

To make sure this work brings real changes to the Tekever AR5 and make this methodology usable for other UAVs, it is important to enumerate possible improvements.

The lack of information regarding the material characteristics was something that had impact in the results of this work. Although the methodology would be the same, more precise results can be obtained if an experimental characterization of both the shell and foam core is made.

In this work, no engine or wing attachments were considered. However, the engines' weight and their acting thrust and torque can be included in the future using localized point masses.

As previously discussed, the ribs were a component that had the same optimal thickness throughout this work due to a lack of buckling constraints. To complement this work, buckling constraints are important and should be added to make sure the wing does not buckle under severe loads;

The next logical step to evolve to is a multi-disciplinary analysis and optimisation, where the coupling of the aerodynamics and structural disciplines is taken into account. The importance of this coupling is not only due to the interaction of the structural behaviour and the aerodynamic forces, but also to enable the analysis of aeroelastic phenomena. Even after the torsion constraint was added, the aeroelastic behaviour of the wing is uncertain. It would be relevant to impose some aeroelastic constraints to prevent both divergence and flutter.

Bibliography

[1] R. G. Grant. *Flight–100 years of aviation*, volume 75. Dorling Kindersley Limited, 2003. ISBN:0-7513-37323.

[2] P. G. Fahlstrom, T. J. Gleason, and M. H. Sadraey. *Introduction to UAV systems*. John Wiley & Sons, 2022. ISBN:978-1-119-97866-4.

[3] S. Gallardo-Saavedra, L. Hernández-Callejo, and O. Duque-Perez. Technological review of the instrumentation used in aerial thermographic inspection of photovoltaic plants. *Renewable and Sustainable Energy Reviews*, 93:566–579, 2018. doi:10.1016/j.rser.2018.05.027.

[4] D. C. Tsouros, S. Bibi, and P. G. Sarigiannidis. A review on UAV-based applications for precision agriculture. *Information*, 10(11):349, 2019. doi:10.3390/info10110349.

[5] H. Yao, R. Qin, and X. Chen. Unmanned aerial vehicle for remote sensing applications—a review. *Remote Sensing*, 11(12):1443, 2019. doi:10.3390/rs11121443.

[6] A. Klimkowska, I. Lee, and K. Choi. Possibilities of UAS for maritime monitoring. *The International Archives of Photogrammetry, Remote Sensing and Spatial Information Sciences*, 41:885, 2016. doi:10.5194/isprsarchives-XLI-B1-885-2016.

[7] M. Arjomandi, S. Agostino, M. Mammone, M. Nelson, and T. Zhou. Classification of unmanned aerial vehicles. *Report for Mechanical Engineering class, University of Adelaide, Adelaide, Australia*, pages 1–48, 2006.

[8] P. Cohn, A. Green, M. Langstaff, and M. Roller. Commercial drones are here: The future of unmanned aerial systems. *McKinsey & Company*, 2017.

[9] Tekever official website - about, Oct 2021. URL `https://www.tekever.com/about/`. Accessed: 15th of december 2022.

[10] P. Raj. Aircraft design in the 21st century-implications for design methods. In *29th AIAA, Fluid Dynamics Conference*, page 2895, Albuquerque,NM,U.S.A., June 1998. doi:10.2514/6.1998-2895.

[11] T. Corke. *Design of Aircraft*. Prentice Hall, 2003. ISBN 9780130892348.

[12] M. H. Sadraey. *Aircraft design: A systems engineering approach*. John Wiley & Sons, 2012. ISBN 78-1-119-95340-1.

[13] P. Panagiotou, P. Kaparos, C. Salpingidou, and K. Yakinthos. Aerodynamic design of a MALE UAV. *Aerospace Science and Technology*, 50:127–138, 2016. doi:10.1016/j.ast.2015.12.033.

[14] F. A. Administration. *Pilot's Handbook of Aeronautical Knowledge*. US Department of Transportation, Federal Aviation Administration, 2016. FAA-H-8083-25B.

[15] J. Yu. Design and optimization of wing structure for a fixed-wing unmanned aerial vehicle (UAV). *Modern Mechanical Engineering*, 8(4):249–263, 2018. doi:10.4236/mme.2018.84017.

[16] B. L. Horvath. *Aircraft Conceptual Structural Design Using The AMMIT Structural Analysis Tool*. San Diego, California, January 2019. doi:10.2514/6.2019-0549.

[17] D. Howe. The prediction of aircraft wing mass. *Proceedings of the Institution of Mechanical Engineers, Part G: Journal of Aerospace Engineering*, 210(2):135–145, 1996. doi:10.1243/PIME_PROC_1996_210_355_02.

[18] S. Chintapalli, M. S. Elsayed, R. Sedaghati, and M. Abdo. The development of a preliminary structural design optimization method of an aircraft wing-box skin-stringer panels. *Aerospace Science and Technology*, 14(3):188–198, 2010. doi:https://doi.org/10.1016/j.ast.2009.12.007.

[19] A. Elham and M. J. van Tooren. Tool for preliminary structural sizing, weight estimation, and aeroelastic optimization of lifting surfaces. *Proceedings of the Institution of Mechanical Engineers, Part G: Journal of Aerospace Engineering*, 230(2):280–295, 2016. doi:10.1177/0954410015591045.

[20] A. Elham, G. La Rocca, and M. J. van Tooren. Development and implementation of an advanced, design-sensitive method for wing weight estimation. *Aerospace Science and Technology*, 29(1): 100–113, 2013. doi:10.1016/j.ast.2013.01.012.

[21] J. Moore and S. Cutright. *Structural Analysis and Performance-Based Validation of a Composite Wing Spar*. San Diego, California, January 2019. doi:10.2514/6.2019-0548.

[22] L. Iqbal and J. Sullivan. Balanced approach to the aircraft design. In *50th AIAA Aerospace Sciences Meeting including the New Horizons Forum and Aerospace Exposition*, page 395, 2012. doi:10.2514/6.2012-395. 9-12 January, Nashville, Tenessee.

[23] D. Grose. Reengineering the aircraft design process. In *5th Symposium on Multidisciplinary Analysis and Optimization*, Panama City Beach, FL, U.S.A., September 1994.

[24] J. R. R. A. Martins and A. Ning. *Engineering Design Optimization*. Cambridge University Press, 2021. ISBN 9781108833417.

[25] T. Katrňák and J. Juračka. Detailed topometry fem optimization of wing structural panel. In *Engineering Mechanics 2015*, volume 821 of *Applied Mechanics and Materials*, pages 357–363. Trans Tech Publications Ltd, 2 2016. doi:10.4028/www.scientific.net/AMM.821.357.

[26] Y. Liao, S. He, J. R. R. A. Martins, and Y. L. Young. *Hydrostructural Optimization of Generic Composite Hydrofoils*. Orlando, FL, January 2020. doi:10.2514/6.2020-0164.

[27] K. Sinha, T. Klimmek, M. Schulze, and V. Handojo. Loads analysis and structural optimization of a high aspect ratio, composite wing aircraft. *CEAS Aeronautical Journal*, 12:233–243, 2021. doi:10.1007/s13272-021-00494-x.

[28] S. Dähne and C. Hühne. Gradient based structural optimization of a stringer stiffened composite wing box with variable stringer orientation. In A. Schumacher, T. Vietor, S. Fiebig, K.-U. Bletzinger, and K. Maute, editors, *Advances in Structural and Multidisciplinary Optimization*, pages 814–826, Cham, 2018. Springer International Publishing. ISBN 978-3-319-67988-4. doi:10.1007/978-3-319-67988-4_62.

[29] S. De, M. Jrad, and R. K. Kapania. Structural optimization of internal structure of aircraft wings with curvilinear spars and ribs. *Journal of Aircraft*, 56(2):707–718, 2019. doi:10.2514/1.C034818.

[30] S. Kilimtzidis, A. Kotzakolios, and V. Kostopoulos. Efficient structural optimisation of composite materials aircraft wings. *Composite Structures*, 303:116268, 2023. doi:10.1016/j.compstruct.2022.116268.

[31] O. Dababneh, T. Kipouros, and J. Whidborne. Application of an efficient gradient-based optimization strategy for aircraft wing structures. *Aerospace*, 5(1):3, Jan 2018. doi:10.3390/aerospace5010003.

[32] E. Jonsson, C. Riso, B. B. Monteiro, A. C. Gray, J. R. R. A. Martins, and C. E. S. Cesnik. High-fidelity gradient-based wing structural optimization including geometrically nonlinear flutter constraint. *AIAA Journal*, 61(7):3045–3061, 2023. doi:10.2514/1.J061575.

[33] O. C. Zienkiewicz, R. L. Taylor, and R. L. Taylor. *The finite element method: solid mechanics*, volume 2. Butterworth-Heinemann, 2000. ISBN 0-7506-5055-9.

[34] M. N. Özişik, H. R. Orlande, M. J. Colaço, and R. M. Cotta. *Finite difference methods in heat transfer*. CRC press, 2017. ISBN 978-1-4822-4345-1.

[35] Y. M. Hashash, J. J. Hook, B. Schmidt, I. John, and C. Yao. Seismic design and analysis of underground structures. *Tunnelling and underground space technology*, 16(4):247–293, 2001. doi:10.1016/S0886-7798(01)00051-7.

[36] J. N. Reddy. *An introduction to the finite element method*, volume 1221. McGraw-Hill New York, 2004. ISBN 007-124473-5.

[37] W. P. Paiva, P. Sollero, and E. L. Albuquerque. Modal analysis of anisotropic plates using the boundary element method. *Engineering Analysis with Boundary Elements*, 35(12):1248–1255, 2011. doi:10.1016/j.enganabound.2011.06.001.

[38] Y. Liu. Analysis of shell-like structures by the boundary element method based on 3-D elasticity: formulation and verification. *International Journal for Numerical Methods in Engineering*, 41(3): 541–558, 1998. doi:10.1002/(SICI)1097-0207(19980215)41:3<541::AID-NME298>3.0.CO;2-K.

[39] R. Eymard, T. Gallouët, and R. Herbin. Finite volume methods. In *Solution of Equation in Rn (Part 3), Techniques of Scientific Computing (Part 3)*, volume 7 of *Handbook of Numerical Analysis*, pages 713–1018. Elsevier, 2000. doi:10.1016/S1570-8659(00)07005-8.

[40] J. N. Reddy. *Mechanics of laminated composite plates and shells: theory and analysis*. CRC press, 2003. ISBN 0-5493-1592-1.

[41] P. W. Tarek I. Zohdi, editor. *An Introduction to Computational Micromechanics*. Springer Berlin, Heidelberg, 2008. ISBN:978-3-540-77482-2.

[42] T. W. Clyne and D. Hull. *An introduction to composite materials*. Cambridge university press, 3rd edition, 2019. ISBN 978-0-521-86095-6.

[43] J. Rodrigues and P. Martins. *Tecnologia Mecânica: Tecnologia da Deformação Plástica - Vol I - Fundamentos Teóricos*. Escolar Editora, 2005. ISBN 9789725922798.

[44] R. M. Jones. *Mechanics of composite materials*. CRC Press, 2nd edition, 1999. ISBN 1-56032-712-X.

[45] K. D. Hjelmstad. *Fundamentals of Structural Mechanics*. Springer New York, NY, 2nd edition, 2005. ISBN 0-387-23331-8. doi:10.1007/b101129.

[46] F. A. Administration. *Aviation Maintenance Technician Handbook–Airframe*, volume 1. US Department of Transportation, Federal Aviation Administration, 2012. FAA-H-8083-31A.

[47] T. J. Hughes and F. Brezzi. On drilling degrees of freedom. *Computer methods in applied mechanics and engineering*, 72(1):105–121, 1989. doi:10.1016/0045-7825(89)90124-2.

[48] D. Fox and J. Simo. A drill rotation formulation for geometrically exact shells. *Computer Methods in Applied Mechanics and Engineering*, 98(3):329–343, 1992. doi:10.1016/0045-7825(92)90002-2.

[49] K. K. Rumayshah, A. Prayoga, and M. A. Moelyadi. Design of high altitude long endurance UAV: Structural analysis of composite wing using finite element method. In *Journal of Physics: Series*, volume 1005, page 012025. IOP Publishing, 2018. doi:10.1088/1742-6596/1005/1/012025.

[50] G. J. Kennedy and J. R. Martins. A parallel finite-element framework for large-scale gradient-based design optimization of high-performance structures. *Finite Elements in Analysis and Design*, 87: 56–73, 2014. doi:10.1016/j.finel.2014.04.011.

[51] G. Kennedy and J. R. R. A. Martins. A comparison of metallic and composite aircraft wings using aerostructural design optimization. In *12th AIAA Aviation Technology, Integration, and Operations (ATIO) Conference and 14th AIAA/ISSMO Multidisciplinary Analysis and Optimization Conference*, Indianapolis, Indiana, September . doi:10.2514/6.2012-5475.

[52] G. K. W. Kenway and J. R. R. A. Martins. Multipoint high-fidelity aerostructural optimization of a transport aircraft configuration. *Journal of Aircraft*, 51(1):144–160, 2014. doi:10.2514/1.C032150.

[53] N. Werter and R. De Breuker. A novel dynamic aeroelastic framework for aeroelastic tailoring and structural optimisation. *Composite Structures*, 158:369–386, 2016. doi:10.1016/j.compstruct.2016.09.044.

[54] K. R. Bramsiepe, V. Handojo, Y. M. Meddaikar, M. Schulze, and T. Klimmek. Loads and structural optimization process for composite long range transport aircraft configuration. In *2018 Multidisciplinary Analysis and Optimization Conference*, Atlanta, Georgia, June 2018. doi:10.2514/6.2018-3572.

[55] N. Wu, G. Kenway, C. A. Mader, J. Jasa, and J. R. R. A. Martins. pyoptsparse: A python framework for large-scale constrained nonlinear optimization of sparse systems. *Journal of Open Source Software*, 5(54):2564, 2020. doi:10.21105/joss.02564.

[56] Z. Lyu, Z. Xu, and J. R. Martins. Benchmarking optimization algorithms for wing aerodynamic design optimization. In *The 8th International Conference on Computational Fluid Dynamics*, Chengdu, Sichuan, China, July 2014. ICCFD8-2014-0203.

[57] L. Zhou, J. Huang, Z. Gao, and W. Zhang. Three-dimensional aerodynamic/stealth optimization based on adjoint sensitivity analysis for scattering problem. *AIAA Journal*, 58(6):2702–2715, 2020. doi:10.2514/1.J059136.

[58] I. Gibert Martínez, F. Afonso, S. Rodrigues, and F. Lau. A sequential approach for aerodynamic shape optimization with topology optimization of airfoils. *Mathematical and Computational Applications*, 26(2), 2021. doi:10.3390/mca26020034.

[59] A. El Ibrahim, S. Abdulkerim, and I. Göv. Aero structural optimization for sailplane wing in preliminary design. *Journal of Advances in Technology and Engineering Research*, 4, 02 2018. doi:10.20474/jater-4.1.5.

[60] R. T. Haftka. Simultaneous analysis and design. *AIAA Journal*, 23(7):1099–1103, 1985. doi:10.2514/3.9043.

[61] G. K. W. Kenway, G. J. Kennedy, and J. R. R. A. Martins. A CAD-free approach to high-fidelity aerostructural optimization. In *Proceedings of the 13th AIAA/ISSMO Multidisciplinary Analysis Optimization Conference*, Fort Worth, TX, September 2010. AIAA 2010-9231.

[62] Solidworks 3D CAD. URL `https://www.solidworks.com/product/solidworks-3d-cad`. Accessed: 8th of january 2023.

[63] Simcenter Femap. URL `https://plm.sw.siemens.com/en-US/simcenter/mechanical-simulation/femap/`. Accessed: 8th of january 2023.

[64] Altair Hypermesh. URL `https://altair.com/hypermesh`. Accessed: 8th of january 2023.

[65] J. R. R. A. Martins, G. Kennedy, and G. K. Kenway. High aspect ratio wing design: Optimal aerostructural tradeoffs for the next generation of materials. In *52nd Aerospace Sciences Meeting*, National Harbor, Maryland, January 2014. doi:10.2514/6.2014-0596.

[66] C. A. Mader, G. K. W. Kenway, A. Yildirim, and J. R. R. A. Martins. ADflow—an open-source computational fluid dynamics solver for aerodynamic and multidisciplinary optimization. *Journal of Aerospace Information Systems*, 2020. doi:10.2514/1.I010796.

[67] MDO Lab. *pyTACS Documentation*. MDO Lab, University of Michigan, USA, 2023. URL `https://mdolab-pytacs.readthedocs-hosted.com/en/latest/index.html`. Accessed: 8th of january.

[68] S. Sethi, A. Striz, S. Sethi, and A. Striz. On using the kreisselmeier-steinhauser function in simultaneous analysis and design. In *38th Structures, Structural Dynamics, and Materials Conference*, Kissimmee, FL, U.S.A., April 1997. doi:10.2514/6.1997-1289.

[69] Paraview. URL `https://www.paraview.org/`. Accessed: 16th of january 2023.

[70] Tecplot 360. URL `https://www.tecplot.com/products/tecplot-360/`. Accessed: 16th of january 2023.

[71] P. R. Amestoy, T. A. Davis, and I. S. Duff. An approximate minimum degree ordering algorithm. *SIAM Journal on Matrix Analysis and Applications*, 17(4):886–905, 1996. doi:10.1137/S0895479894278952.

[72] *AIREX® C70*. 3A Composites Core Materials, 2011. URL `https://www.3accorematerials.com/uploads/documents/TDS-AIREX-C70-E_1106.pdf`. Accessed: 19th of April 2023.

[73] *T700S - Standard Modulus Carbon Fiber*. Toray Composite Materials America, Inc., 2018. URL `https://www.toraycma.com/wp-content/uploads/T700S-Technical-Data-Sheet-1.pdf.pdf`. Accessed: 19th of April 2023.

Appendix A

UAV Market Overview

Table A.1: Market overview

Company	Name	Endurance [kg]	Endurance [h]	Range [km]	Wingspan [m]	Cruise speed [km h^{-1}]	Payload [kg]	Ceiling [m]
Tekever	AR5	180	12	-	7.3	100	50	
UKRSPECSYSTEMS	PD-2	55	8	1100	5	100	19	4500
UKRSPECSYSTEMS	PD-1	40	7		4	95	10	3000
Applied Aeronautics	Albatross Fixed Wing UAV	10	4	250	3	68	4.4	
Plyrotech	XV/XV-H	25	3/4	241/322	2.95	80	2.5/3.5	4572
Plyrotech	XVL	85	7	788	4.5	112	25	4572
Volatus Aerospace	Flexrotor	25	15	2000	3		7.7	1300
Censys Technologies	Sentaero BVLOS	10	1.2	90	2.3	73		
Censys Technologies	Sentaero VLOS	8.4	1-1.75	120	2.1	64		
A-TechSYN	CGT50	55	6	80-200	4.71		5	5500
Boresight	Viking VTOL	7	0.42	5	2.2	108		
FIXAR	FIXAR 007	7	1	60	1.54	65-72	2	
FIXAR	FIXAR 025	25	3.5	300	2.8	85	10	5000
CHC Navigation	P330 Pro	14	2.7		2.53	75.6	2	6000
UAVOS	BOREY 20	20	5	430	0.875	72		430
UAVOS	Albatross 2.2	550	20	2255	14.97	205	250	7200
UAVOS	SITARIA E	39	1.5	240	5.16	80	10	6000
EleveonX	SkyEye Sierra VTOL	12.5	3/5	320	3.1	65	3	
EleveonX	SkyEye Sierra	12.5	4.5/8	500	3	65	5	
EleveonX	Tango VTOL	20.5	2.5/6	420	3	72	5	
EleveonX	SkyEye Delta	6.25	2.5/3.5	140/200	2.29	58	2	
Robot Aviation	SkyRobot FX10	6.5	2.5		2			
Robot Aviation	SkyRobot FX20	13	4	40	3.16	90	3	4000
Robot Aviation	SkyRobot FX450	200	20	200-2500	7.2	125	30	5000
Airlogix	Hammerhead eV20 fixed-wing version	80	1		4.7	72	20	3500
C-Astral Aerospace	BRAMOR C4EYE	3.8-4.7	3	150	2.3	58	0.6-1	5000
C-Astral Aerospace	BRAMOR ppx	4.5	3.5	150	2.3	58	0.6-1	5000
C-Astral Aerospace	ATLAS AS90X	2.7	1.5	90	1.55	47	0.3	5000
C-Astral Aerospace	SQA eVTOL	10	2.5	160	2.9	61	1	4000
Black Swift Technologies	S2	9.5	1.83	110	3	43	2.3	6000
Black Swift Technologies	So	1.59	1.5		1.39	61		4572
Skyeton	Raybird 3	20	18-24	120	3	110	5	4500
Vertical Technologies	DeltaQuad	6.2	2	120	2.35	65	1.2	4000
UAVision	OGS42	38	10	100	4.2	94	5	2438
UAVision	OGS42V	36	6-8	100	4.2	94	5	2438
UAVision	WINGO S	10	2	40	2.3	40	3	
UAVision	WINGO	25	10	250	3.9	70	5	
Gadfin Aero-Logistics Systems	Spirit X	250		500	10.5	150	150	
Cannon Dynamics	Sword Cargo 6.0	350			6		250	
AheadX	QP532	18	3.2	150	3.2	70-90		4000
AheadX	QP530	16	3	150	3	75		4000
Aertec Solutions	Tarsis	75	12	150	5.2	100	12	4267
General Atomics Aeronautical Systems	Predator MQ-1	1020		1240	16.8	130	204	7620
Portuguese Air Force Academy	ANTEX-M	150	15		7		30	4500
EMPORDEF	PAIC Império SP1	80		120	2.4	120		4500
SCR	ATLANTIC I	55	8	100	3.8	120	5	
SCR	TUCAN	5	1.5	25	2.74	65	0.75	
Conyca	Conyca Geodrone	2	1		1.5		0.6	
Thales Spain	Thales Fulmar X	20	6-12	800	3		8	4000

Appendix B

TACS guidelines

For a better understanding of how TACS software works, a flow chart of the dependency of the files created to run the problem are presented in Fig. B.1 and B.2.

To setup the problem, a Python file was created with the name *setup_tacs.py*. In this, the mesh file is imported using the pyTACS class from *pytacs.py*, with all the information regarding nodes, their connectivity to form the finite elements, the type of elements to be used, a label for certain regions of the mesh and finally, the constraints. After having this information, the design variable groups are set using the *pyTACS.addVariables* method. This is done using the labels for each wingbox region. For example, if the front and rear spar sections have different labels in the mesh file but their properties and design boundaries are the same for the optimisation, a unique design variable group can be set, that includes both.

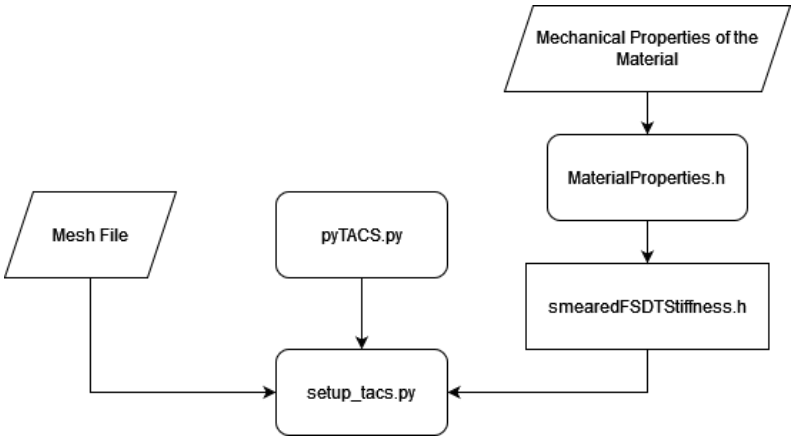

Figure B.1: Flow chart of *setup_tacs.py* file

Having these groups set, the constitutive model (see Sec. 4.2.3) is created calling the *pyTACS.create TACSAssembler* method for each one. This model is generated by first defining an orthotropic ply class using the OrthoPly class present in TACS *MaterialProperties.h* header file and given a set of material properties. Then, this material class is used as input to create the smearedFSDTStiffness class from *smearedFSDTStiffness.h*, given some stacking and thickness parameters. To make sure the design variable groups were set as desired, an output file can be created and opened with a post-processing

software like ParaView [69] or Tecplot [70] by calling the *pyTACS.writeDVVisualization* method.

Following this, the final step in this setup file is to specify the functions to be monitored throughout the optimisation, either the constraints or objective function, with the *pyTACS.addFunction* method. These are part of a group of already defined functions such as total mass and maximum failure.

Finally, in the file to run the analysis and optimisation, called *struct_opt.py*, the loads and the objective function and constraints, from the group of functions specified in the setup file, are set. This starts by creating a StructProblem class from *pyStruct_problem.py*, which is from a Python library called base-classes from the University of Michigan MDO Lab. This is used to represent all the relevant information for the structural analysis, including the loads. For the aerodynamic loads, TACS takes in consideration the input file used to define de StructProblem class. To add a fixed load, such as an engine weight, and gravity, the methods *pyTACS.addLoadToComponents* and *pyTACS.addInertialLoad* must be used, respectively. The only missing informations are relative to the optimisation process.

An Optimization class from *pyOpt_optimization.py* of the pyOptSparse Python library is created, to contain all information about the optimisation problem. The objective function is defined using the *Optimization.addObj* method, the design variables and constraints are defined with the *pyTACS.addVariables PyOpt* and *pyTACS.addConstraintsPyOpt* and *Optimization.addCon*, respectively.

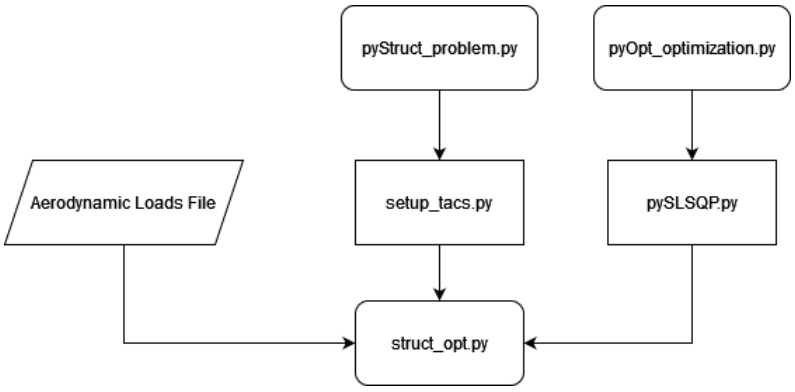

Figure B.2: Flow chart of *struct_opt.py* file

Finally, the optimiser is chosen. Depending on the optimiser algorithm, different options need to be given. In this case, the choice was the SLSQP and the optimisation routine to solve the problem is defined by calling the SLSQP class in *pySLSQP.py* from pyOptSparse. The TACS itself does not solve the optimisation but, instead, provides the necessary gradients for the gradient-based optimiser. For each iteration, the structural analysis is performed, which is done by calling the pyTACS class giving the StructProblem class as input. Both the function evaluations as well as the sensitivities provided to the optimiser are obtained using the *pyTACS.evalFunctions* and *pyTACS.evalFunctionsSens*, respectively.

Appendix C

Tekever AR5 Material Characterization

C.1 Wing Geometry

In Fig. C.1, a parametrisation of the real AR5 wingbox is given with the control points that define the front spar (blue), rear spar (orange) and ribs (grey). Together with that, the distribution of the DV groups used for the front spar and rear spar are also shown as FS and RS, respectively.

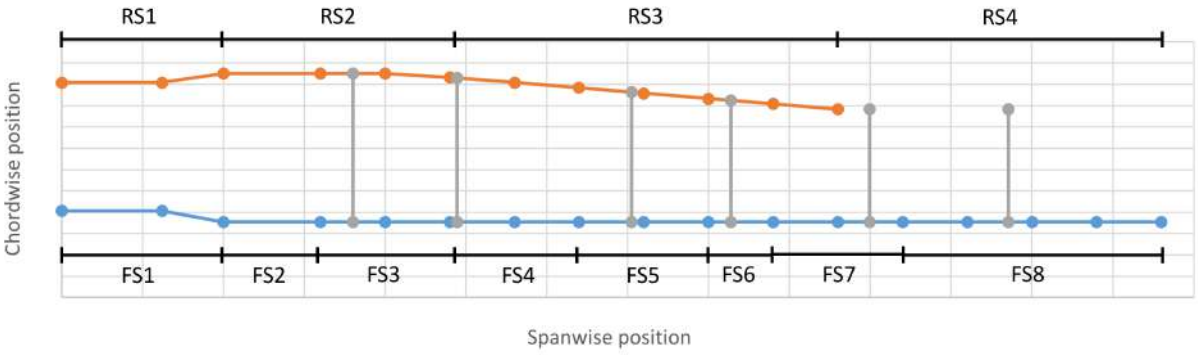

Figure C.1: Wingbox parametrisation

C.2 Material Characterization

Depending on the wingbox component, different fractions and types of foam and CFRP are used. A summary of these fractions is given in Tab. C.1.

For the thickness, different values were used for both the upper and lower skins and the ribs. Each DV group represented in Fig. C.1 has the thickness given in Tab. C.2.

Regarding the physical and mechanical properties necessary of the foam, these were obtained from the manufacturer data-sheet and summarized in Tab. C.3.

The CFRP is composed of carbon fibres and resin in a pre-defined portion. To obtain the density and Young's modulus, a rule of mixtures was applied as described in Sec. 3.3. For the strength parameters,

Table C.1: CFRP and foam proportions with corresponding type of foam

	CFRP		Foam (Ref.)
	$0°$	$90°$	
Front spar (FS1)			
Front spar (remaining groups)			
Rear spar (RS1)			
Rear spar (remaining groups)			
Ribs			
Skin			

Table C.2: Baseline thickness of each DV group

Front Spar	1 (Root)	2	3	4	5	6	7	8 (Tip)
Thickness [mm]								

Rear Spar	1 (Root)	2	3	4 (Tip)
Thickness [mm]				

Table C.3: Foam properties [72]

Material	Foam type 1	Foam type 2	Foam type 3
Density [$\mathrm{kg\,m^{-3}}$]			
Tensile modulus in the plane [MPa]			
Shear modulus [MPa]			
Tensile strength in the plane [MPa]			

these were obtained from fibres data-sheet in a section of composite properties. A summary of the properties obtained can be seen in Tab. C.4.

Table C.4: Density and physical properties of CFRP ply [73]

Density*
Young's modulus (fibre direction)*
Young's modulus (transverse direction)*
Shear modulus
Poisson ratio
Tensile strength (fibre direction)
Compressive strength (fibre direction)
Tensile and compressive strength (transverse direction)
Shear strength

* Obtained from rule of mixtures

Appendix D

Optimal Solutions

D.1 Ply Angle Continuity Constraint - Case 3

Table D.1: Thickness results for each component and DV group for case 3

Upper Skin	1 (Root)	2	3	4	5	6	7 (Tip)
Thickness [mm]	2.8	1.4	1.2	1.0	1.0	1.0	1.0

Lower Skin	1 (Root)	2	3	4	5	6	7 (Tip)
Thickness [mm]	2.5	1.0	1.0	1.0	1.0	1.0	1.0

Front Spar	1 (Root)	2	3	4	5	6	7	8 (Tip)
Thickness [mm]	3.6	0.4	0.3	0.3	0.3	0.3	0.3	0.3

Rear Spar	1 (Root)	2	3	4 (Tip)
Thickness [mm]	2.7	0.3	0.3	0.4

Table D.2: Ply angle and thickness results for each rib for case 3

Ribs	1 (Root)	2	3	4	5	6
θ_1	$90.0°$	$89.5°$	$90.0°$	$90.0°$	$89.5°$	$90.0°$
θ_2	$0.0°$	$-0.5°$	$0.0°$	$0.0°$	$-0.5°$	$0.1°$
Thickness [mm]	1.0	1.0	1.0	1.0	1.0	1.0

D.2 Orthogonal Plies Constraint - Case 4

Table D.3: Thickness results for each component and DV group for case 4

Upper Skin	1 (Root)	2	3	4	5	6	7 (Tip)
Thickness [mm]	3.2	2.0	1.6	1.2	1.0	1.0	1.7

Lower Skin	1 (Root)	2	3	4	5	6	7 (Tip)
Thickness [mm]	2.7	1.9	1.5	1.2	1.0	1.0	1.0

Front Spar	1 (Root)	2	3	4	5	6	7	8 (Tip)
Thickness [mm]	3.2	0.3	0.3	0.3	0.3	0.3	0.3	0.3

Rear Spar	1 (Root)	2	3	4 (Tip)
Thickness [mm]	0.9	0.3	0.3	0.3

D.3 Decreasing Thickness Constraint - Case 5

Table D.4: Thickness results for each component and DV group for case 5

Upper Skin	1 (Root)	2	3	4	5	6	7 (Tip)
Thickness [mm]	3.2	2.0	1.6	1.4	1.4	1.4	1.4

Lower Skin	1 (Root)	2	3	4	5	6	7 (Tip)
Thickness [mm]	2.7	1.9	1.5	1.1	1.0	1.0	1.0

Front Spar	1 (Root)	2	3	4	5	6	7	8 (Tip)
Thickness [mm]	3.1	0.3	0.3	0.3	0.3	0.3	0.3	0.3

Rear Spar	1 (Root)	2	3	4 (Tip)
Thickness [mm]	2.8	0.3	0.3	0.3

Table D.5: Ply angle and thickness results for each rib for case 5

Ribs	1 (Root)	2	3	4	5	6
θ_1	$90.0°$	$88.9°$	$89.9°$	$90.0°$	$89.4°$	$89.2°$
θ_2	$0.0°$	$-1.1°$	$-0.1°$	$0.0°$	$-0.6°$	$-0.7°$
Thickness [mm]	1.0	1.0	1.0	1.0	1.0	1.0

D.4 Tip Torsion Constraint - Case 6

Table D.6: Thickness results for each component and DV group for case 6

Upper Skin	1 (Root)	2	3	4	5	6	7 (Tip)
Thickness [mm]	3.1	2.0	1.6	1.4	1.4	1.4	1.4

Lower Skin	1 (Root)	2	3	4	5	6	7 (Tip)
Thickness [mm]	2.8	1.9	1.5	1.2	1.0	1.0	1.0

Front Spar	1 (Root)	2	3	4	5	6	7	8 (Tip)
Thickness [mm]	3.1	0.3	0.3	0.3	0.3	0.3	0.3	0.3

Rear Spar	1 (Root)	2	3	4 (Tip)
Thickness [mm]	3.2	0.3	0.3	0.3

D.5 Tip Torsion Constraint - Case 6 (New Baseline)

Table D.7: Thickness results for each component and DV group for case 6 - new baseline

Upper Skin	1 (Root)	2	3	4	5	6	7 (Tip)
Thickness [mm]	3.1	1.9	1.6	1.4	1.4	1.4	1.4

Lower Skin	1 (Root)	2	3	4	5	6	7 (Tip)
Thickness [mm]	2.8	1.9	1.5	1.1	1.0	1.0	1.0

Front Spar	1 (Root)	2	3	4	5	6	7	8 (Tip)
Thickness [mm]	3.0	0.3	0.3	0.3	0.3	0.3	0.3	0.3

Rear Spar	1 (Root)	2	3	4 (Tip)
Thickness [mm]	3.1	0.3	0.3	0.3

Table D.8: Ply angle results for each component for case 6 - new baseline

	Upper Skin	Lower Skin	Front Spar	Rear Spar
θ_1	$87.2°$	$90.0°$	$87.1°$	$73.1°$
θ_2	$-2.7°$	$0.1°$	$-2.9°$	$-16.9°$

Table D.9: Ply angle and thickness results for each rib for case 6 - new baseline

Ribs	1 (Root)	2	3	4	5	6
θ_1	$90.0°$	$88.7°$	$89.9°$	$90.0°$	$89.1°$	$89.7°$
θ_2	$0.0°$	$-1.3°$	$-0.1°$	$0.0°$	$-0.9°$	$-0.3°$
Thickness [mm]	1.0	1.0	1.0	1.0	1.0	1.0

Appendix E

Custom Constraints Implementation

In this appendix, some code excerpts used for the custom constraints used throughout the optimisations are shown. Since several files needed to be changed, only the parts considered relevant are here presented.

E.1 Orthogonal Plies Constraint

```
int OrthoPlieCon::evalCon(int offset, TacsScalar con[]) {
  for (int k = 0; k < ncon; k++) {
    con[offset + k] = abs(sx[k] * x[k] - sy[k] * y[k]);
  }
  return ncon;
}

int OrthoPlieCon::evalConDVSens(int offset, TacsScalar Acol[], const int rowp[], const
    int cols[]) {
  int start = rowp[offset];
  for (int k = 0; k < ncon; k++) {
    Acol[start] = sx[k];
    start++;
    Acol[start] = -sy[k];
    start++;
  }
  return ncon;
}
```

Listing E.1: Excerpt from the orthogonal plies constraint in TACSSparseCon.c file

```
def addOrthogonalPliesConstraint(self, delta=1.5708, index=1, ribs=0, **kwargs):
"""
Parameters
----------
delta : float or list
```

```
The maximum change change between variables. This constraint is enforced between design variables ``x1`` and ``x2``:
.. math:: -\delta < x_1 - x_2 < \delta
index : int of list of ints
The index of the dv's on each constitutive object to constrain. Note this implies that the order of design variables on the con objects much match.
"""

dvSet = self._findAdjacencySet(**kwargs)
indices = np.atleast_1d(index)
deltas = np.atleast_1d(delta)

"""... CODE OMITTED ..."""

    if not dvNumsA[index] == dvNumsB[index]:
      # Finally add the sparseConstraint -- one at a time
      self.linearSparseCon.addConstraint(
        self.TACS.OrthoPlieCon([dvNumsA[index]], [dvNumsA[index+1]], [deltas[i]-1.0e-3], [deltas[i]])
      )
      if j == len(dvSet)-1:
      self.linearSparseCon.addConstraint(
        self.TACS.OrthoPlieCon([dvNumsB[index]], [dvNumsB[index+1]], [deltas[i]-1.0e-3], [deltas[i]])
      )

"""... CODE OMITTED ..."""

  if ribs == 1:
    dvSet = [0,1,2,3,4,5] # First 6 DV Groups
    for j in range(len(dvSet)):
      ndvA = self.conObjects[dvSet[j]].getNumDesignVars()
      dvNumsA = np.zeros(ndvA, dtype="intc")
      self.conObjects[dvSet[j]].getDesignVarNums(dvNumsA)

      for i in range(len(indices)):
        index = indices[i]

        # Finally add the sparseConstraint
        self.linearSparseCon.addConstraint(
          self.TACS.OrthoPlieCon([dvNumsA[index]], [dvNumsA[index+1]], [deltas[i]-1.0e-3], [deltas[i]])
        )
```

Listing E.2: Excerpt from the orthogonal plies constraint in pytacs.py file

E.2 Monotonic Thickness Constraint

```
def addDecreasingThickConstraints(self, delta, index=0, **kwargs):
"""
Add a set of constraints to not allow the increase in thickness with increasing DV number
    ‘.

Parameters
----------
delta : float or list
The maximum change change between variables. This constraint is enforced between design
    variables ‘‘x1‘‘ an ‘‘x2‘‘:

.. math:: -\delta < x_1 - x_2 < \delta

index : int of list of ints
The index of the dv’s on each constitutive object to constrain. Note this implies that
    the order of design variables on the con objects much match.
"""

# Find the set of group indices that are geometrically adjacent to one another
dvSet = self._findAdjacencySet(**kwargs)
indices = np.atleast_1d(index)
deltas = np.atleast_1d(delta)

"""... CODE OMITTED ..."""

    if not dvNumsA[index] == dvNumsB[index]:
      # Finally add the sparseConstraint -- one at a time
      self.linearSparseCon.addConstraint(
        self.TACS.AdjacencySparseCon([dvNumsA[index]], [dvNumsB[index]], [0], [deltas[i
    ]])
      )

"""... CODE OMITTED ..."""
```

Listing E.3: Excerpt from the monotonic thickness constraint in pytacs.py file

E.3 Tip Torsion Constraint

```
const char* TipTorsion::funcName = "TipTorsion";

TipTorsion::TipTorsion(TACSAssembler* _tacs) : TACSFunction(_tacs) {
  torsion_val = 0.0;
  maxNumNodes = 0;
  quad_type = GAUSS_QUADRATURE;
  scheme_elevation = 0;
}
```

```
9
10 """... CODE OMITTED ..."""
11
12 void TipTorsion::elementWiseEval(const int iter, TACSElement* element, int elemNum, const
       TacsScalar vars[], const TacsScalar Xpts[], int* iwork, TacsScalar* work) {
13
14   // Get the information about the number of nodes
15   int numNodes = element->numNodes();
16
17   // The number of displacements per node
18   int numDisp = element->numDisplacements();
19
20 """... CODE OMITTED ..."""
21
22   for (int k = 0; k < numNodes; k++) {
23     TacsScalar X[3];
24     X[0] = Xpts[3 * k];
25     X[1] = Xpts[3 * k + 1];
26     X[2] = Xpts[3 * k + 2];
27
28     if (X[0] == 0.1771 && (X[1] <= 0.0465 && X[1] >= 0.0464990) && X[2] == 3.4){ /* P1
       LOCATION */
29       p1[0] = X[0];
30       p1[1] = X[1];
31       p1[2] = X[2];
32       work[2] = p1[0];
33       work[3] = p1[1];
34       elemNum1 = elemNum;
35
36 """... CODE OMITTED ..."""
37
38         // Compute the displacement along the specified vector
39         TacsScalar disp = 0.0;
40         int a = 1; // y component of displacement
41         TacsScalar d = 0.0; //0
42           for (int j = 0; j < numNodes; j++) {
43             d += teste[j] * vars[numDisp * j + a];
44           }
45
46         // Set the maximum displacement
47         if (abs(d) > abs(work[1])) {
48           work[0] = d;
49         }
50         }
51     } else if (X[0] == 0.441 && (X[1] <= 0.0285 && X[1] >= 0.0284890) && X[2] == 3.4){ /*
        P2 LOCATION */
52       p2[0] = X[0];
53       p2[1] = X[1];
54       p2[2] = X[2];
```

```
      work[4] = p2[0];
      work[5] = p2[1];
      elemNum2 = elemNum;

"""... CODE OMITTED ..."""

        // Compute the displacement along the specified vector
        TacsScalar disp = 0.0;
        int a = 1;  // y component of displacement
        TacsScalar d = 0.0; //0.0
        for (int j = 0; j < numNodes; j++) {
          d += teste[j] * vars[numDisp * j + a];
        }

        // Set the maximum displacement
        if (abs(d) > abs(work[1])) {
          work[1] = d;
        }
      }
    }
  }
}

void TipTorsion::postEvalThread(const int iter, int* iwork, TacsScalar* work) {

  double delta_x = 0.0;
  double delta_y_init = 0.0;
  double delta_y_final = 0.0;
  double alfa1 = 0.0;
  double alfa2 = 0.0;

  /* work[0] -> disp1
  work[1] -> disp2
  work[2] -> x1
  work[3] -> y1
  work[4] -> x2
  work[5] -> y2 */

  delta_x = work[4] - work[2];
  delta_y_init = work[3] - work[5]; //Positive tip up
  alfa1 = atan(delta_y_init/delta_x) * 180 / 3.1415;
  delta_y_final = (work[3] + work[0]) - (work[5] + work[1]); //Positive tip up
  alfa2 = atan(delta_y_final/delta_x) * 180 / 3.1415;
  torsion_val = alfa2;
}

void TipTorsion::elementWiseSVSens(TacsScalar* elemSVSens, TACSElement* element, int
    elemNum, const TacsScalar vars[], const TacsScalar Xpts[], TacsScalar* work) {

```

```
"""... CODE OMITTED ..."""

  if (elemNum == elemNum1){
  for (int k = 0; k < 3 && k < numDisp; k++) {
    if (k != 1) {
      for (int j = 0; j < numNodes; j++) {
        elemSVSens[numDisp * j + k] = 0.0;
      }
    } else {
      for (int j = 0; j < numNodes; j++) {
        if (j == 0) {
          elemSVSens[numDisp * j + k] = (1 / (delta_x * (1 + pow((delta_y_final / delta_x
    ),2))));
        } else {
          elemSVSens[numDisp * j + k] = 0.0;
        }
      }
    }
  }
  } else if (elemNum == elemNum2) {
    for (int k = 0; k < 3 && k < numDisp; k++) {
      if (k != 1) {
        for (int j = 0; j < numNodes; j++) {
          elemSVSens[numDisp * j + k] = 0.0;
        }
      } else {
        for (int j = 0; j < numNodes; j++) {
          if (j == 0) {
            elemSVSens[numDisp * j + k] = -(1 / (delta_x * (1 + pow((delta_y_final /
    delta_x),2))));
          } else {
            elemSVSens[numDisp * j + k] = 0.0;
          }
        }
      }
    }
  } else {
    for (int k = 0; k < 3 && k < numDisp; k++) {
      for (int j = 0; j < numNodes; j++) {
        elemSVSens[numDisp * j + k] = 0.0;
      }
    }
  }
}

"""... CODE OMITTED ..."""
```

Listing E.4: Excerpt from the tip torsion constraint in the created TipTorsion.c file

Appendix F

Scripts for Geometric Definition and Mesh Generation

F.1 pyGeo Script

```
import numpy as np
from pygeo import pyGeo

"""... CODE OMITTED ..."""

# --------- Sharp Trailing Edge / Rounded Tip -------
wing = pyGeo(
  "liftingSurface",
  xsections=airfoil_list,
  scale=chord,
  offset=offset,
  x=x,
  y=y,
  z=z,
  rotX=rot_x,
  rotY=rot_y,
  rotZ=rot_z,
  kSpan=2,
  tip="rounded",
)

wing.writeIGES("AR5_WING_PYGEO.igs")
```

Listing F.1: Excerpt from pyGeo scrip

F.2 pyLayout Script

```
from pygeo import pyGeo, geo_utils
from pylayout import pyLayout

pathName = os.path.dirname(__file__)
surfFile = os.path.join(pathName, "AR5_WING_PYGEO.igs")
geo = pyGeo("iges", fileName=surfFile)

"""... CODE OMITTED ..."""

# Shell element order and number of elements per panel
elementOrder = 2
spanSpace = 16 * numpy.ones(nribs - 1, "intc")
ribSpace = 16 * numpy.ones(nspars + 1, "intc")
verticalSpace = 16
stringerSpace = 0

# Setup X, the array of rib/spar intersections
leList = [
  [offsets[0] + 0.29 * chords[0], 0, 0.0],
  [offsets[0] + 0.29 * chords[0], 0, 0.310],
  """... CODE OMITTED ..."""
  [offsets[0] + 0.253 * chords[0], 0, 3.4],
]
teList = [
  [offsets[0] + 0.72 * chords[0], 0, 0.0],
  [offsets[0] + 0.72 * chords[0], 0, 0.310],
  """... CODE OMITTED ..."""
  [offsets[0] + 0.630 * chords[0], 0, 3.4],
]

"""... CODE OMITTED ..."""

# Boundary conditions
ribBC = {0: {"all": "123456"}}

# Set up pyLayout and write BDF file
layout = pyLayout.Layout(
  geo, teEdgeList, nribs, nspars, elementOrder=elementOrder, domain=domain,
  ribPosPara=ribPosPara, ribBlank=ribBlank, sparBlank=sparBlank,
  topStringerBlank=topStringerBlank, botStringerBlank=botStringerBlank,
  ribStiffenerBlank=ribStiffenerBlank, minStringerHeight=0.025, maxStringerHeight=0.025,
  spanSpace=spanSpace, ribSpace=ribSpace, vSpace=verticalSpace,
  stringerSpace=stringerSpace, flipRibStiffner=False, flipUp=False, ribBC=ribBC
)
layout.finalize(os.path.join(pathName, "AR5_WINGBOX_CONV7.bdf"))
```

Listing F.2: Excerpt from pyLayout scrip